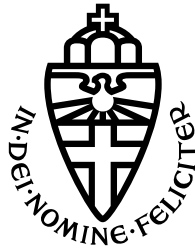RADBOUD UNIVERSITY NIJMEGEN
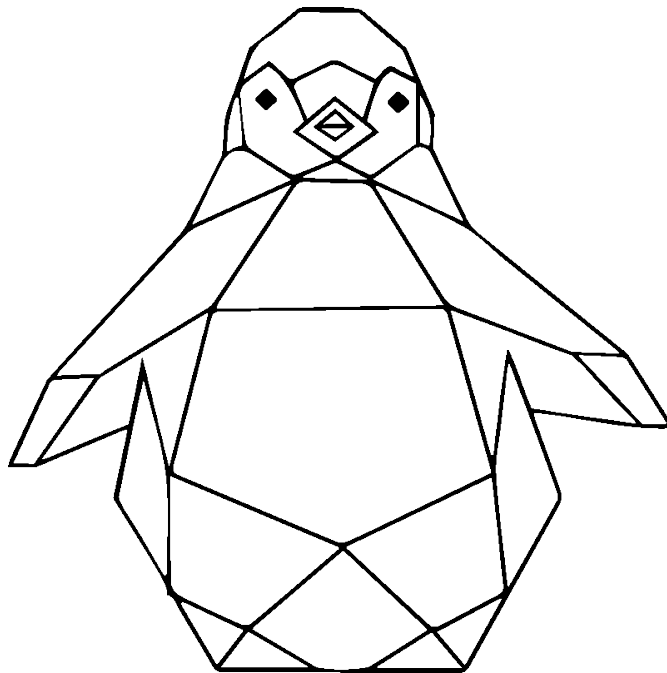
FACULTY OF SCIENCE, DEPARTMENT OF HIGH ENERGY PHYSICS

Branching ratio calculations for $B_s^0 \to \mu^+\mu^-$

A COMPARATIVE ANALYSIS OF COMPUTATIONAL TOOLS

Author:
L.Y. VAN DIJK

Supervisors:
Prof. dr. W.J.P. BEENAKKER
M.C. VAN BEEKVELD
M.T. SCHUTTEN

January 12, 2020

Acknowledgements - Dankwoord

Toen ik bijna anderhalf jaar geleden aan dit project begon, had ik niet kunnen bedenken dat ik gedurende het proces zoveel zou leren. Naast dat ik me op wetenschappelijk gebied heb ontwikkeld, heb ik ook op persoonlijk gebied stappen gezet. Ik heb mijn masterstage ervaren als een groot avontuur en ben erg trots op het uiteindelijke resultaat. Dat had had ik niet kunnen bereiken zonder de hulp en steun van veel mensen om mij heen. Een aantal mensen wil ik graag persoonlijk bedanken.

Allereerst mijn begeleiders, Wim Beenakker, Melissa van Beekveld en Marrit Schutten. Dankzij jullie aanmoedigingen en tips heb ik veel mogen leren en is het mij gelukt om het beste uit mijzelf te halen tijdens dit project. Graag wil ik jullie nog specifiek bedanken voor de uitvoerige feedback die jullie hebben gegeven op eerdere versies van deze thesis. Dat was erg leerzaam en het heeft mij geholpen om tot een goed eindproduct te komen. Tot slot ben ik erg blij dat we gezamenlijk dit project tot een goed einde hebben weten te brengen.

Furthermore, I would like to thank Robert Fleischer and Ruben Jaarsma from Nikhef for introducing me to the world of B-physics. I really appreciate it that you were always available for questions and I enjoyed the time we spent together at Nikhef.

Ook wil ik graag Bob Stienen bedanken. Mede dankzij jouw hulp heb ik mijn programmeervaardigheden weten op te krikken het afgelopen jaar. Maar nog belangrijker, ik kon ook altijd bij je terecht als ik ergens mee zat. Mede dankzij jou steun heb ik me door de moeilijke momenten heen geslagen en daar ben ik je erg dankbaar voor.

Als laatste wil ik graag mijn huisgenoten, vrienden en familie bedanken. Jullie waren er altijd voor mij, zowel in goede als in slechte tijden. Dankzij jullie steun en aanmoedigingen is het mij gelukt om dit project tot een goed einde te brengen. Bedankt!

Contents

1 Introduction

The Standard Model (SM) of particle physics describes the interactions among the smallest building blocks of nature by means of three, non-gravitational, fundamental forces. These building blocks of nature are called fundamental particles. The SM contains three generations of matter particles, quarks and leptons, which interact via the electromagnetic, strong and weak force. There also exists a fourth fundamental force, which is gravity. This force is not described by the SM, but by the theory of general relativity. Experiments and observations show that the SM is not the complete story. Therefore, we need a theory that goes beyond the SM (BSM). An example of an extension of the SM is Supersymmetry (SUSY), which introduces a symmetry between bosons and fermions. In its minimal version, SUSY introduces a so-called superpartner for each SM particle. These superpartners possess the same internal quantum numbers as their SM counterparts, but their spin differs by 1/2. The model that describes the minimal supersymmetric extension of the SM is the Minimal Supersymmetric Standard Model (MSSM). This model introduces a large number (100+) of additional free parameters.

Though experiments such as the Large Hadron Collider (LHC) have been searching for signs of SUSY for years, none of the new particles introduced in the MSSM have been discovered so far. A possible reason could be that, since the parameter space for new physics is so large, we simply have not looked at the right place. Therefore the best strategy is to make use of the knowledge we already possess, to constrain the parameter space of the MSSM. This will tell us in which regions current and future experiments have to search to find new physics. One of the observables, which is influenced by the presence of SUSY particles and therefore used to constrain the MSSM, is the branching ratio (BR) of the decay $B_s^0 \to \mu^+\mu^-$. Multiple tools have been developed to calculate this BR. However, it turns out that, for the same set of MSSM parameters, they can give a different BR result. This is quite inconvenient, since it could lead to incorrect exclusion decisions.

In this thesis, we will focus on BR calculations performed by the programs SuperIso[15] and MicrOMEGAs [18]. We will compare these tools in the phenomenological MSSM (pMSSM), which is a constrained version of the MSSM with only 19 additioned free parameters. We will investigate how these programs calculate the BR of $B_s^0 \to \mu^+\mu^-$, and why these programs sometimes result in different outcomes. Next to this, we will study the behavior of the BR in the pMSSM, to determine which parameters have the largest effect on this calculation. Furthermore, we will try to explain why the calculation results in a SM-like BR for some parameter settings, whereas for other models the calculated values are much larger. The final question we aim to answer is which of these programs can be used best to calculate the BR of the decay $B_s^0 \to \mu^+\mu^-$.

The outline of this thesis is as follows. First, a brief description of the SM of particle physics and an introduction to the MSSM are provided in chapter 2. Next, chapter 3 gives an introduction to the process $B_s^0 \to \mu^+\mu^-$. This chapter also explains $B_s^0 - \bar{B}_s^0$-mixing and provides a step-by-step derivation of the BR expressions. An overview of the different computational tools that are used is given in chapter 4. This chapter also describes the differences in the BR calculations performed by SuperIso and MicrOMEGAs. The analysis of the BR behavior for both programs is split into two parts. First, chapter 5 compares the calculations performed by both programs in the SM. Next, chapter 6 analyses the behavior of the BR within the pMSSM. At the end of this thesis, we will determine which program can be used best to perform the BR calculation.

1.1 Notations and conventions

- We will adopt natural units where $\hbar = c = 1$.

- For the Minkowski metric $\eta_{\mu\nu}$ we choose the convention $\eta_{\mu\nu} = \mathrm{diag}(+1, -1, -1, -1)$.

- We will use the Einstein summation convention for all repeated indices.

- The partial derivative is defined as $\partial_\mu \equiv \frac{\partial}{\partial x^\mu}$.

- The 4 x 4 Dirac gamma matrices are defined in the chiral representation. They are given by

$$\gamma^0 = \begin{pmatrix} 0 & I_2 \\ I_2 & 0 \end{pmatrix}, \qquad \gamma^j = \begin{pmatrix} 0 & \sigma^j \\ -\sigma^j & 0 \end{pmatrix}, \qquad j = 1, 2, 3.$$

  Here I_2 is the 2 x 2 identity matrix and σ^j are the Pauli spin matrices, which are defined as

$$\sigma^1 = \begin{pmatrix} 0 & 1 \\ 1 & 0 \end{pmatrix}, \qquad \sigma^2 = \begin{pmatrix} 0 & -i \\ i & 0 \end{pmatrix}, \qquad \sigma^3 = \begin{pmatrix} 1 & 0 \\ 0 & -1 \end{pmatrix}.$$

- The SM fermions are described by four-dimensional Dirac spinors (ψ). The adjoint Dirac spinor is defined as $\bar{\psi} = \psi^\dagger \gamma^0$.

- For a four-component Dirac spinor, the left- and right-handed components ('L', 'R') are defined as

$$\psi_L = P_L \psi, \qquad \psi_R = P_R \psi,$$

  where the chiral projection operators P_L and P_R are given by

$$P_L = \frac{1}{2}(1 - \gamma^5), \qquad P_R = \frac{1}{2}(1 + \gamma^5),$$

  in terms of $\gamma^5 = i\gamma^0 \gamma^1 \gamma^2 \gamma^3$.

- The Levi-Civita symbol ϵ_{abc} is defined as

$$\epsilon_{abc} = \begin{cases} 1 & \text{if (a,b,c) is an even permutation of (1,2,3)} \\ -1 & \text{if (a,b,c) is an odd permutation of (1,2,3)} \\ 0 & \text{otherwise} \end{cases}.$$

- The abbreviation 'h.c.' is short for 'Hermitian conjugate'.

2 The Standard Model and Supersymmetry

This chapter gives a brief overview of the SM of particle physics. Furthermore, an introduction to SUSY is provided. The particle content of the MSSM is discussed and a description of the pMSSM is given.

2.1 The Standard Model

The SM of particle physics was established in the previous century. It describes the interactions of two kinds of particles: spin-1/2 matter fermions, and spin-1 gauge bosons. Next to this, the SM also describes the Higgs boson, a spin-0 particle that is responsible for the mass acquisition of other particles. As mentioned in the introduction, though the SM can be used to explain a large part of the world around us, it falls short in being a complete theory. This is because it, for example, does not incorporate gravity, does not explain the huge imbalance between the amount of matter and anti-matter in our universe and does not include dark matter. However, despite its shortcomings, the SM provides a basis for our understanding of the universe. Therefore, we will describe its basic properties in this chapter. We start with a brief mathematical description of the SM as a quantum field theory, based on the lectures on 'The Standard Model and Beyond' by Wim Beenakker[8] and the textbook on quantum field theory by Peskin and Schroeder[28]. Furthermore, we provide an introduction to the electroweak theory (EW) and quantum chromodynamics (QCD). Lastly, we will explain how particles acquire mass and give an overview of the particle content of the SM.

2.1.1 Lagrangian formalism and the gauge principle

The SM is a quantum field theory in which every particle is described by a continuous quantum field that has specific transformation properties under the Lorentz group. The dynamics of these fields can be formulated in terms of a Lagrangian density ($\mathcal{L}$), or Lagrangian for short. In this section, we will construct a field theory that is invariant under local gauge transformations. We start from the massless free Dirac Lagrangian for spin-1/2 particles

$$\mathcal{L}(x) = \bar{\psi}(x)i\gamma^\mu\partial_\mu\psi(x), \tag{1}$$

where ψ is a 4-dimensional Dirac spinor ($\bar{\psi} = \psi^\dagger(x)\gamma^0$) and γ^μ (with $\mu = 0, 1, 2, 3$) are the Dirac γ-matrices. First, we impose a global U(1) (also called 'abelian') gauge transformation

$$\psi(x) \to e^{i\alpha}\psi(x), \qquad \bar{\psi}(x) \to e^{-i\alpha}\bar{\psi}(x), \tag{2}$$

where α is a real constant and U(1) means that we use the same phase factor for each field component. The Lagrangian remains invariant if we apply this global transformation. Since relativistic quantum mechanics should be a local theory, we demand our theory to be also invariant under local gauge transformations. To check whether this is true for our theory, we impose a local U(1) gauge transformation

$$\psi(x) \to e^{i\alpha(x)}\psi(x), \qquad \bar{\psi}(x) \to e^{-i\alpha(x)}\bar{\psi}(x), \tag{3}$$

where local refers to $\alpha(x)$ being a real scalar function dependent on x. If we impose this transformation, our Lagrangian is no longer invariant, but contains an extra term

$$\mathcal{L}'(x) = \mathcal{L}(x) - \bar{\psi}(x)\gamma^\mu\partial_\mu\alpha(x)\psi(x). \tag{4}$$

Here, $\mathcal{L}(x)$ refers to the original Lagrangian given in equation 1. In order to make our Lagrangian locally invariant, we have to compensate for this extra term. We will do this by replacing the ordinary derivative ∂_μ by a so-called covariant derivative D_μ. This covariant derivative is chosen such that it transforms as $D_\mu\psi(x) \to D'_\mu\psi'(x) = e^{i\alpha(x)}D_\mu\psi(x)$. This can be achieved by writing the covariant derivative as

$$D_\mu \equiv \partial_\mu + igA_\mu(x), \tag{5}$$

where g is a gauge coupling, and $A_\mu(x)$ is a gauge field, that transforms as $A_\mu(x) \to A'_\mu(x) = A_\mu(x) - \frac{1}{g}\partial_\mu\alpha(x)$. The particles described by a gauge field are spin-1 gauge bosons. In this way we obtain a Lagrangian that is invariant under local gauge transformations and that describes the interaction between

spin-1/2 matter particles and spin-1 gauge bosons.

The last step we have to take, is to add a gauge invariant kinetic term for the gauge field $A_\mu(x)$:

$$\mathcal{L}(x) = \bar{\psi}(x)i\gamma^\mu D_\mu \psi(x) - \frac{1}{4}F_{\mu\nu}(x)F^{\mu\nu}(x), \tag{6}$$

where $F_{\mu\nu}(x) = \partial_\mu A_\nu(x) - \partial_\nu A_\mu(x)$ is an anti-symmetric field strength tensor.

Different matter particles have different charges and therefore couple in a different way to the gauge field $A_\mu(x)$. This can be achieved by scaling $\alpha(x)$ and g according to $\alpha(x) \to Q\alpha(x)$ and $g \to Qg$. This leaves the transformation property of $A_\mu(x)$ unaltered, which means that the same gauge field can couple to particles of different charge. The covariant derivative changes to $D_\mu \equiv \partial_\mu + iQgA_\mu(x)$, which causes a change in the interaction strength. If we set $g = |e|$ (unit charge) and $q = Q|e|$ (particle charge) we arrive at

$$
\begin{aligned}
\mathcal{L}_{\text{QED}} &= \bar{\psi}(x)i\gamma^\mu D_\mu \psi(x) - \frac{1}{4}F_{\mu\nu}(x)F^{\mu\nu}(x), \\
&= \bar{\psi}(x)i\gamma^\mu \partial_\mu \psi(x) - q\bar{\psi}(x)\gamma^\mu \psi(x)A_\mu(x) - \frac{1}{4}F_{\mu\nu}(x)F^{\mu\nu}(x).
\end{aligned} \tag{7}
$$

This is the Lagrangian for the theory of quantum electrodynamics (QED). We can identify $A_\mu(x)$ as the electromagnetic potential and $F_{\mu\nu}(x)$ is called the electromagnetic field strength tensor.

We have assumed that the gauge field $A_\mu(x)$ and its corresponding particles are massless. A massive gauge field would require the addition of a mass term of the form $\frac{1}{2}m_A^2 A_\mu(x)A^\mu(x)$. However, by adding such a term, we would break gauge invariance. So for the electromagnetic field, local gauge invariance implies that the mass of the gauge field is zero. If we would nevertheless like to add a massive gauge field to the theory, we have to find a way to work around this. We come back to this issue when we discuss electroweak symmetry breaking (EWSB).

Generalized gauge principle

We will now generalize the gauge theory concept we used to describe QED, to non-abelian groups. A characteristic of these groups is that their generators (T^a) do not commute. An example of such a non-abelian group is SU(N), which is a unitary group that consists of $N \times N$ matrices with a determinant of 1. This group has $N^2 - 1$ generators and the generators obey the following commutation relation: $[T^a, T^b] = if^{abc}T^c$, where f^{abc} are real and totally antisymmetric structure constants.

We consider a massless Dirac Lagrangian for an N-component multiplet of Dirac fields:

$$\mathcal{L}(x) = \bar{\psi}(x)i\gamma^\mu \partial_\mu \psi(x), \qquad \psi(x) = \begin{pmatrix} \psi_1(x) \\ \vdots \\ \psi_N(x) \end{pmatrix}. \tag{8}$$

This Lagrangian is invariant under global continuous SU(N) transformations:

$$
\begin{aligned}
\psi(x) &\to \psi'(x) = U\psi(x), \\
\bar{\psi}(x) &\to \bar{\psi}'(x) = \bar{\psi}(x)U^\dagger, \\
&\text{with } U = e^{i\alpha^a T^a},
\end{aligned} \tag{9}
$$

where α^a are real constants and a runs over the total number of generators. We will again demand local invariance, which means that $\alpha^a \to \alpha^a(x)$. To achieve this, we will replace the derivative ∂_μ by the following covariant derivative

$$D_\mu \equiv \partial_\mu + igK_\mu^a(x)T^a, \tag{10}$$

where g is the SU(N) gauge coupling and where $K_\mu^a(x)$ are the gauge fields. For every generator, there is a distinct gauge field. These gauge fields must transform as $K_\mu^a(x) \to K_\mu'^a(x) = K_\mu^a(x) - \frac{1}{g}\partial_\mu \alpha^a(x) - f^{abc}\alpha^b(x)K_\mu^c(x)$.

Next, we generalize the kinetic term for the gauge fields by defining the SU(N) field strength tensor:

$$K^a_{\mu\nu}(x) = \partial_\mu K^a_\nu(x) - \partial_\nu K^a_\mu(x) - gf^{abc}K^b_\mu(x)K^c_\nu(x). \tag{11}$$

This kinetic term contains, compared to QED, a new non-abelian term that implies self-interactions between the gauge fields. Combining our results, we obtain the following massless Lagrangian that is invariant under local SU(N) gauge transformations:

$$\mathcal{L}_{\mathrm{SU}(N)} = \bar{\psi}(x)i\gamma^\mu D_\mu\psi(x) - \frac{1}{4}K^a_{\mu\nu}(x)K^{a,\mu\nu}(x). \tag{12}$$

The (unbroken) SM is locally invariant under two of such non-abelian gauge groups: SU(2) and SU(3). If we combine them with the abelian U(1) theory, we can write the gauge group of the SM as

$$SU(3)_C \otimes SU(2)_L \otimes U(1)_Y,$$

where C stands for color charge, L for left-handed chirality and Y is the hypercharge. In the next section we will discuss the interactions that arise from the SU(3)$_C$ and SU(2)$_L\otimes$U(1)$_Y$ gauge groups.

2.1.2 Electroweak theory (EW) and Quantum chromodynamics (QCD)

The SU(2)$_L\otimes$U(1)$_Y$ gauge groups are responsible for the electroweak interactions. The generators of these groups are the Pauli spin matrices (σ^a, $a = 1, 2, 3$) and the hypercharge (Y). The corresponding gauge fields, W^a_μ and B_μ, couple by the gauge couplings g and g' to fermionic fields. The gauge coupling g is called the weak interaction strength. The SU(2) subscript L refers to the fact that the SU(2) gauge bosons only couple to left-handed fermions. It is for this reason, that left-handed fermions appear in matter doublets and the right-handed fermions appear in matter singlets under SU(2). The Lagrangian for the electroweak theory can be written as

$$\mathcal{L}_{\mathrm{EW}} = \bar{\psi}_L(x)i\gamma^\mu D_{\mu,L}\psi_L(x) + \bar{\psi}_R(x)i\gamma^\mu D_{\mu,R}\psi_R(x) - \frac{1}{4}W^a_{\mu\nu}(x)W^{a,\mu\nu}(x) - \frac{1}{4}B_{\mu\nu}(x)B^{\mu\nu}(x), \tag{13}$$

where the electroweak field strength tensors are given by

$$\begin{aligned} W^a_{\mu\nu}(x) &= \partial_\mu W^a_\nu(x) - \partial_\nu W^a_\mu(x) - g\epsilon_{abc}W^b_\mu(x)W^c_\nu(x), \\ B_{\mu\nu}(x) &= \partial_\mu B_\nu(x) - \partial_\nu B_\mu(x). \end{aligned} \tag{14}$$

Here ϵ_{abc} is the Levi-Civita symbol. The covariant derivatives ($D_{\mu,L}$ and $D_{\mu,R}$) are defined as

$$\begin{aligned} D_{\mu,L} &= \partial_\mu + \frac{i}{2}g\sigma^a W^a_\mu(x) + ig'Y(\psi_L)B_\mu(x), \\ D_{\mu,R} &= \partial_\mu + ig'Y(\psi_R)B_\mu(x). \end{aligned} \tag{15}$$

The strong interaction arises from the SU(3)$_C$ gauge group. For this group there are eight generators. The gauge fields that correspond to these generators are called gluons. The gauge fields G^a_μ couple by the gauge coupling g_s, the strong interaction strength, to fermions called quarks. The quarks reside in matter triplets and carry an internal quantum number called color, which can be red, green or blue. A single quark can not exist as a free particle, because free particles turn out to be color neutral. Quarks therefore always appear in bound states, this is called quark confinement. A color neutral bound state of three quarks (consisting of an (anti-)red, (anti-)green and (anti-)blue quark) is called a hadron and a color neutral combination of two quarks (consisting of a color and anti-color quark) a meson. The Lagrangian for QCD can be written as

$$\mathcal{L}_{\mathrm{QCD}} = \bar{\psi}(x)i\gamma^\mu D_\mu\psi(x) - \frac{1}{4}G^a_{\mu\nu}(x)G^{a,\mu\nu}(x), \tag{16}$$

where the strong field strength tensor is given by

$$G^a_{\mu\nu}(x) = \partial_\mu G^a_\nu(x) - \partial_\nu G^a_\mu(x) - g_s f^{abc}G^b_\mu(x)G^c_\nu(x). \tag{17}$$

2.1.3 Generating masses

The gauge theory we have constructed so far only allows for massless particles. From experiments we know that all SM particles, except for the photon and gluons, are massive. A simple solution to this problem is the addition of mass terms to the Lagrangian. However, as mentioned before, if we do this for the gauge bosons we will break gauge invariance. Next to this, the addition of a fermion mass term of the form $m\bar{\psi}\psi = m(\bar{\psi}_R\psi_L + \bar{\psi}_L\psi_R)$, will also break gauge invariance. This is because $SU(2)_L$ is a chiral theory, in which the different chiral states (ψ_L, ψ_R) transform in a different way under local gauge transformations. Therefore, we need to find another way to generate masses for these particles.

A solution to this is the Higgs mechanism. In this procedure a hypercharge 1, complex scalar doublet of Higgs fields, Φ, is added to the SM. This scalar doublet has 4 real degrees of freedom (d.o.f.) and consists of one charged and one complex neutral component. The new terms that are added to the SM Lagrangian are given by

$$\mathcal{L}_{\text{Higgs}} = (D_\mu\Phi)^\dagger(D^\mu\Phi) - \mu^2\Phi^\dagger\Phi - \lambda(\Phi^\dagger\Phi)^2 = (D_\mu\Phi)^\dagger(D^\mu\Phi) - V(\Phi),$$
$$\text{with } \Phi = \begin{pmatrix} \phi^+ \\ \phi^0 \end{pmatrix}. \tag{18}$$

If we demand that $\mu^2 < 0$ and $\lambda > 0$, the potential $V(\Phi)$ has a local maximum at $|\phi| = 0$ and a ring of minima at $|\phi|^2 = \frac{-\mu^2}{2\lambda} \equiv \frac{v^2}{2} > 0$. Because $|\phi| = 0$ is unstable, it is not suitable as a groundstate. We may choose the groundstate anywhere in the ring of minima, but we choose it such that $\langle 0| \hat{\phi} |0\rangle = \langle\phi\rangle_0 = (0, \frac{v}{\sqrt{2}})$. This groundstate expectation value is also referred to as the vacuum expectation value (VEV). By choosing this groundstate, the symmetry of the gauge group is broken. For this reason, we call this process electroweak symmetry breaking (EWSB). As a next step, we will switch to the unitary gauge, for which $\Phi(x) = \frac{1}{\sqrt{2}}(0, v + h(x))$. Here $h(x)$ is a physical Higgs boson field, and v is the VEV, which will create mass terms for the gauge bosons. After EWSB, we find three gauge boson mass eigenstates which are mixtures of the gauge eigenstates W_μ^a and B_μ

$$A_\mu = s_W W_\mu^3 + c_W B_\mu$$
$$Z_\mu = c_W W_\mu^3 - s_W B_\mu$$
$$W_\mu^\pm = \frac{1}{\sqrt{2}}(W_\mu^1 \mp iW_\mu^2) \tag{19}$$
$$\text{with } s_W = \sin\theta_W, \ c_W = \cos\theta_W, \ \tan\theta_W = \frac{g'}{g}.$$

Here θ_W is the weak mixing angle. These three mass eigenstates are known as the photon, the Z boson and the W bosons. In the above described process, the W and Z bosons acquired a mass because they were supplied with an extra d.o.f.[1] This extra d.o.f. originated from the complex scalar doublet that was added to the SM. This doublet initially had 4 d.o.f., of which 3 were used to generate the gauge boson masses. The remaining d.o.f. corresponds to a new scalar particle: the Higgs boson.

In the previous paragraph we successfully obtained masses for gauge bosons by means of the Higgs mechanism. We will now use this mechanism to give masses to the fermions. To achieve this, we introduce $SU(2)_L \otimes U(1)_Y$ invariant interactions between the fermions and scalar doublets. These so-called Yukawa interactions are given by

$$\mathcal{L}_{\text{Yukawa}} = -y_e{}^{ab}\bar{L}_L'^a\Phi e_R'^b - y_d{}^{ab}\bar{Q}_L'^a\Phi d_R'^b - y_u{}^{ab}\bar{Q}_L'^a\tilde{\Phi}u_R'^b + \text{h.c.}, \tag{20}$$

where $e_R'^b$, $d_R'^b$ and $u_R'^b$ are the gauge eigenstates of the right-handed fermion singlets, and $L_L'^a$ and $Q_L'^a$ are the gauge eigenstates of the left-handed fermion doublets, for the leptons and quarks, respectively. The labels a and b refer to the three different generations of matter fermions and the $y_i{}^{ab}$ are complex 3×3 matrices in generation (family) space, called Yukawa couplings. The fermion mass terms follow from the non-zero VEV of the Higgs potential and are given by

---

[1] A massless gauge boson has two d.o.f., whereas a massive gauge boson has three d.o.f..

$$\frac{-v}{\sqrt{2}}\left[y_e^{ab}\bar{e}_L'^a e_R'^b + y_d^{ab}\bar{d}_L'^a d_R'^b + y_u^{ab}\bar{u}_L'^a u_R'^b + \text{h.c.}\right]. \tag{21}$$

The terms contain mass matrices $M_i^{ab} = \frac{v}{\sqrt{2}}y_i^{ab}$ for the gauge eigenstates. We can switch to the mass eigenstates by bringing these mass matrices into a diagonal form. To diagonalize the mass matrices we use unitary matrices (S_i and W_i)

$$\begin{aligned} u_L'^a &= S_u^{ab} u_L^b, & d_L'^a &= S_d^{ab} d_L^b \\ u_R'^a &= W_u^{ab} u_R^b, & d_R'^a &= W_d^{ab} d_R^b \end{aligned} \tag{22}$$

If we take a closer look at the electroweak interactions, we see that the matrices S_u and S_d cancel out in the terms that describe the couplings to the Z boson and the photon. For example, for the electromagnetic current we can write

$$\bar{u}_L'^a \gamma^\mu u_L'^a = \bar{u}_L^b S_u^{\dagger ba} \gamma^\mu S_u^{ac} u_L^c = \bar{u}_L^b \gamma^\mu \underbrace{(S_u^\dagger S_u)}_{I}{}^{bc} u_L^c = \bar{u}_L^a \gamma^\mu u_L^a. \tag{23}$$

The same can be done for the right-handed eigenstates. This relation implies that no flavour changing neutral currents (FCNC) occur at the tree level. They do appear at higher loop orders, however these processes are suppressed within the SM. For the charged current interaction with the W bosons, we do see a trace of the diagonalization procedure

$$\bar{u}_L'^a \gamma^\mu d_L'^a = \bar{u}_L^b S_u^{\dagger ba} \gamma^\mu S_d^{ac} d_L^c = \bar{u}_L^b \gamma^\mu (S_u^\dagger S_d)^{bc} d_L^c = \bar{u}_L^a \gamma^\mu (V_{\text{CKM}})^{ab} d_L^b. \tag{24}$$

The resulting matrix V_{CKM} is known as the Cabibbo-Kobayashi-Maskawa (CKM) matrix. It describes the mixing of quarks in the charged current interactions. Similar to the quark sector, provided that we add neutrino mass terms and right-handed neutrino fields to the SM Lagrangian, also lepton mixing can take place in these interactions. This mixing is described by the Pontecorvo-Maki-Nakagawa-Sakata (PMNS) matrix. A detailed description of the CKM and PMNS matrices is given in appendix A.

2.1.4 SM particle content

To conclude our description of the SM, we will give an overview of its particle content and corresponding fields. As mentioned before, the SM consists of matter fermions, gauge bosons and the Higgs boson. The matter fermions can be divided in two groups: quarks, which are subject to strong interactions and leptons, which are not subject to strong interactions. Both groups contain six spin-1/2 fermions and six spin-1/2 anti-fermions. The six quark flavors are up (u), down (d), charm (c), strange (s), top (t) and bottom (b). The six lepton types are electron (e), electron neutrino (ν_e), muon (μ), muon neutrino (ν_μ), tau (τ) and tau neutrino (ν_τ). Within the SM, pairs of quarks and leptons are grouped together in three generations. The first generation consists of u, d, ν_e and e, the second generation consists of c, s, ν_μ and μ and the third generation consists of t, b, ν_τ and τ. The spin-1 gauge bosons are responsible for the mediation of the fundamental forces. The photon (γ) mediates the electromagnetic force, the W and Z bosons ($W^\pm, Z^0$) mediate the electroweak force and the gluons (g) are the mediators of the strong force. As explained in the previous section, the spin-0 Higgs boson is responsible for the mass acquisition of the other particles. An overview of all SM particles and their corresponding fields is given in table 1[2]. For each particle, the charge, spin and representation under the SM gauge group is provided.

---

[2]Note that our definition of the SM does not include right-handed neutrinos, as is done traditionally.

Name	Fields	Content	Charge	Spin	$SU(3)_C \otimes SU(2)_L \otimes U(1)_Y$
Quarks (3 generations)	Q_L	$(u,d)_L$	(2/3, -1/3)	1/2	$\mathbf{3} \otimes \mathbf{2} \otimes 1/6$
	u_R	u_R	(2/3)	1/2	$\mathbf{3} \otimes \mathbf{1} \otimes 2/3$
	d_R	d_R	(-1/3)	1/2	$\mathbf{3} \otimes \mathbf{1} \otimes -1/3$
Leptons (3 generations)	L_L	$(\nu_e, e)_L$	(0, -1)	1/2	$\mathbf{1} \otimes \mathbf{2} \otimes -1/2$
	e_R	e_R	-1	1/2	$\mathbf{1} \otimes \mathbf{1} \otimes -1$
Gluon	G_μ^a	g	0	1	$\mathbf{8} \otimes \mathbf{1} \otimes 0$
W bosons	W_μ^b	$W^\pm, Z^0, \gamma$	$\pm 1, 0, 0$	1	$\mathbf{1} \otimes \mathbf{3} \otimes 0$
B boson	B_μ	Z^0, γ	0, 0	1	$\mathbf{1} \otimes \mathbf{1} \otimes 0$
Higgs boson	(ϕ^+, ϕ^0)	h	0	0	$\mathbf{1} \otimes \mathbf{2} \otimes 1/2$

Table 1: Particle content of the SM, with for each particle the corresponding fields, electrostatic charge, spin and representation under the SM gauge group. In this representation, the first two boldface numbers indicate the dimension of the corresponding representation of the gauge group and the last number denotes the eigenvalue of the hypercharge Y. For the quarks and leptons, only one generation is displayed. The gauge fields W_μ^b and B_μ mix to form the electromagnetically neutral mass eigenstates Z^0 (Z boson) and γ (photon) after EWSB. Adapted from ref. [41] and ref. [42].

2.2 Supersymmetry

An extension of the SM is the MSSM. This extension could explain some of the phenomena that the SM cannot describe, such as the existence of dark matter. Furthermore, it could unify the three fundamental forces that are described by the SM. This section will give a brief introduction to the MSSM. For a detailed theoretical description, the reader is referred to refs. [25] and [37].

The MSSM is created by imposing an additional symmetry on the SM Lagrangian: a supersymmetry. This symmetry is a spacetime symmetry that relates bosons to fermions. The operator Q, which is the generator of the symmetry, turns a bosonic state into a fermionic state and vice versa.

$$Q \left| \text{Boson} \right\rangle = \left| \text{Fermion} \right\rangle, \qquad Q \left| \text{Fermion} \right\rangle = \left| \text{Boson} \right\rangle.$$

The operator Q is fermionic, which leads to an algebra of anti-commutation relations[37]

$$\{Q_\alpha, Q_\beta^\dagger\} = 2(\sigma^\mu)_{\alpha\beta} P_\mu,$$
$$\{Q_\alpha, Q_\beta\} = \{Q_\alpha^\dagger, Q_\beta^\dagger\} = 0,$$
$$\{P^\mu, Q_\alpha\} = \{P^\mu, Q_\alpha^\dagger\} = 0,$$

where P^μ is the four-momentum generator of spacetime translations and $\sigma^\mu \equiv (I_2, \sigma^1, \sigma^2, \sigma^3)$. Here σ^j, for $j = 1, 2, 3$, denotes the Pauli spin matrices.

The MSSM is the simplest supersymmetric extension of the SM. It describes the minimal amount of new particles and interactions that are added to the SM by imposing the extra symmetry. Within the MSSM, the bosonic and fermionic states are grouped together in 'supermultiplets'. Each supermultiplet contains the same number of bosonic and fermionic d.o.f.. These bosonic and fermionic states are referred to as 'superpartners' of each other. Particles that are part of the same supermultiplet have equal masses and internal quantum numbers. For the MSSM, it is convenient to write the 4-component Dirac spinor (ψ) in terms of two Weyl spinors

$$\psi = \begin{pmatrix} \chi_L \\ \chi_R \end{pmatrix}, \tag{25}$$

where χ_L denotes a left-handed Weyl spinor and χ_R a right-handed Weyl spinor. Since these spinors describe fermions, they must anti-commute. We can define the charge conjugate of a right-handed

Weyl spinor as $\psi_R^c \equiv i\sigma^2\psi_R^*$, where σ^2 is the second Pauli spin matrix. By using this definition, a right-handed Weyl spinor can be brought in left-handed form and vice versa. The two simplest possibilities to create a supermultiplet with an equal amount of bosonic and fermionic d.o.f. are a 'chiral' and 'gauge' supermultiplet. A chiral supermultiplet is a combination of a two-component spin-1/2 Weyl fermion with a complex scalar field with spin 0. A gauge supermultiplet contains a spin-1 gauge boson and a two-component spin-1/2 (Majorana) Weyl fermion.

Within the MSSM, the SM fermions obtain bosonic spin-0 superpartners. They are members of the chiral supermultiplets. The names for the superpartners are constructed by adding an 's' (for scalar) to the original name, resulting in 'squarks', 'sleptons', and collectively 'sfermions'. For example, the superpartner of the right-handed electron is the right-handed selectron. The symbols that denote the squarks and sleptons are the same as for the corresponding fermions, but with an added tilde (i.e. $\tilde{e}$ for the selectron). It is important to note that for the sfermions the handedness does not refer to the helicity of the particle (since they are spin-0 particles), but to that of their superpartners. The gauge interactions for all sfermions involve the same covariant derivatives as for the corresponding SM fermions. They only differ due to the difference in kinetic terms for bosons and fermions. An overview of the chiral supermultiplets within the MSSM is given in table 3. The gauge bosons of the SM are members of the gauge supermultiplets. The names of their fermionic superpartners are constructed by adding 'ino' to the name of the SM particle. Collectively they are called 'gauginos'. An overview of the gauge supermultiplets within the MSSM is given in table 2.

Names	spin 1/2	spin 1	$SU(3)_C \otimes SU(2)_L \otimes U(1)_Y$
gluino, gluon	$\tilde{g}$	g	$\mathbf{8} \otimes \mathbf{1} \otimes 0$
winos, W bosons	$\widetilde{W}^\pm, \widetilde{W}^0$	$W^\pm, W^0$	$\mathbf{1} \otimes \mathbf{3} \otimes 0$
bino, B boson	$\widetilde{B}^0$	B^0	$\mathbf{1} \otimes \mathbf{1} \otimes 0$

Table 2: Gauge supermultiplets in the MSSM. Adapted from ref. [37].

In order to have a gauge invariant supersymmetric Lagrangian, the MSSM contains two Higgs chiral supermultiplets, one with $Y = 1/2$ and one with $Y = -1/2$. The $Y = 1/2$ Higgs supermultiplet couples by means of a Yukawa coupling to up-type quarks, whereas the $Y = -1/2$ Higgs supermultiplet couples to down-type quarks and charged leptons. The two complex scalar fields are called H_u (for the $Y = 1/2$ supermultiplet) and H_d (for the $Y = -1/2$ supermultiplet). The components of H_u are denoted by H_u^+, H_u^0, which have charges 1 and 0 respectively. Similarly, H_d has components H_d^0, H_d^- with charges 0 and -1. An overview of the Higgs chiral supermultiplets is given in table 3.

Names	spin 0	spin 1/2	$SU(3)_C \otimes SU(2)_L \otimes U(1)_Y$
squarks, quarks	$(\tilde{u}, \tilde{d})_L$	$(u, d)_L$	$\mathbf{3} \otimes \mathbf{2} \otimes 1/6$
(3 generations)	$\tilde{u}_R^*$	u_R^c	$\bar{\mathbf{3}} \otimes \mathbf{1} \otimes -2/3$
	$\tilde{d}_R^*$	d_R^c	$\bar{\mathbf{3}} \otimes \mathbf{1} \otimes 1/3$
sleptons, leptons	$(\tilde{\nu}_e, \tilde{e})_L$	$(\nu, e)_L$	$\mathbf{1} \otimes \mathbf{2} \otimes -1/2$
(3 generations)	$\tilde{e}_R^*$	e_R^c	$\mathbf{1} \otimes \mathbf{1} \otimes 1$
Higgs, higgsinos	(H_u^+, H_u^0)	$(\widetilde{H}_u^+, \widetilde{H}_u^0)$	$\mathbf{1} \otimes \mathbf{2} \otimes 1/2$
	(H_d^0, H_d^-)	$(\widetilde{H}_d^0, \widetilde{H}_d^-)$	$\mathbf{1} \otimes \mathbf{2} \otimes -1/2$

Table 3: Chiral supermultiplets in the MSSM. A standard convention is used where all chiral supermultiplets are defined in terms of left-handed spinors, such that the conjugates of the right-handed (s)fermions appear in the table. Adapted from ref. [37].

Since there are two complex Higgs doublets in the MSSM, the description of EWSB is slightly more complicated than in the SM. Again we have to demand that the minimum of the Higgs scalar potential (which has changed due to the extra doublet, for an expression see ref. [37]) breaks the SU(2) symmetry down to electromagnetism. Making use of the SU(2) gauge freedom, we can set $H_u^+ = H_d^- = 0$ at the minimum of the potential. For EWSB to occur, H_u^0 and H_d^0 need non-zero VEVs. These are set at $v_u = v \sin\beta$ for H_u^0 and $v_d = v \cos\beta$ for H_d^0. Here $v_u^2 + v_d^2 = v^2 = \frac{4M_Z^2}{g^2 + g'^2}$ is required to be consistent with EWSB of the SM. The VEVs are taken to be real and positive, therefore we have $0 < \beta < \pi/2$. The ratio of the VEVs is denoted by $\tan\beta = v_u/v_d$. Before EWSB, we started with two complex scalar Higgs doublets consisting of eight d.o.f.. After EWSB, three d.o.f. are used to give masses to Z^0 and $W^\pm$ (similar to the SM) and five Higgs scalar mass eigenstates remain: two CP-even neutral scalars (h^0 and H^0), one CP-odd neutral scalar (A^0), and two charged scalars (H^+ and H^-).

In principle, the MSSM allows for processes that violate baryon and lepton number, such as proton decay. Because such processes are not experimentally observed, we want to make sure that these processes do not occur. Therefore, a new symmetry called 'R-parity' is introduced to the MSSM. This new quantum number P_R is conserved in the MSSM. All SM particles have $P_R = +1$ and all SUSY particles have $P_R = -1$. Due the conservation of R-parity in the MSSM, the lightest SUSY particle (LSP) must be stable.

Soft SUSY Breaking

Since none of the superpartners have been discovered until now, SUSY must be a broken symmetry. However, the mechanism to break supersymmetry is unknown, but needed for achieving EWSB. In a quantum field theory, a symmetry can be broken in two ways. It can happen spontaneously, such as in the SM by means of the Higgs mechanism. Symmetry breaking may also be forced by adding extra terms to the Lagrangian that break this symmetry (explicitly). This is the way in which supersymmetry is broken in the MSSM. The Lagrangian of the MSSM can be written as $\mathcal{L} = \mathcal{L}_{\text{SUSY}} + \mathcal{L}_{\text{soft}}$. The first term ($\mathcal{L}_{\text{SUSY}}$) contains all the gauge and Yukawa interactions and preserves supersymmetry invariance. The second term ($\mathcal{L}_{\text{soft}}$) violates supersymmetry. The SUSY breaking terms should be 'soft'[37], which means that they should be of positive mass dimension. The soft SUSY breaking terms introduce over a 100 free parameters to the MSSM Lagrangian. Without a mechanism that describes how they enter the Lagrangian, the parameters can only be determined by experiment.

2.2.1 The pMSSM

Since it is hard to work with such a large set of independent parameters as in the MSSM, often a constrained version of the model is used. An example of this is the phenomenological MSSM (pMSSM), which is obtained by imposing the following constraints[24][40]:

- There are no new CP-violating terms. The MSSM introduces new CP violating terms. In the pMSSM these terms are set to zero, which leaves the SM as the only source of CP violation.

- There are no tree-level flavor changing neutral currents (FCNC). This constraint is supported by experimental results and met by taking all sfermion mass matrices and trilinear couplings (A_f) to be diagonal in generation space.

- The first and second sfermion generations are degenerate. This is supported by experimental data on meson mixing, which limits the splitting between the masses of the first and second generation sfermions.

- The first and second generation trilinear couplings (A_f) are set to zero. Hence, only A_t, A_b and A_τ have a non-zero value.

These constraints reduce the number of parameters to 19, which are listed in table 4. The parameter values are defined at a scale equal to the geometric mean of the top squark masses called the 'SUSY scale', $M_{\text{SUSY}} \equiv \sqrt{m_{\tilde{t}_1} m_{\tilde{t}_2}}$.

Parameter	Description
M_1, M_2, M_3	bino, wino and gluino mass
μ	higgsino mass
$\tan\beta$	the ratio of the vacuum expectation values of the two Higgs doublets
m_A	CP odd Higgs mass
A_t, A_b, A_τ	trilinear couplings of the third generation sfermions
$m_{\tilde{Q}_1}$	first and second generation left-handed squark mass
$m_{\tilde{Q}_3}$	third generation left-handed squark mass
$m_{\tilde{u}_R}, m_{\tilde{d}_R}$	first and second generation right-handed squark masses
$m_{\tilde{t}_R}, m_{\tilde{b}_R}$	third generation right-handed squark massess
$m_{\tilde{L}_1}$	first and second generation left-handed slepton mass
$m_{\tilde{L}_3}$	third generation left-handed slepton mass
$m_{\tilde{e}_R}$	first and second generation right-handed charged slepton mass
$m_{\tilde{\tau}_R}$	third generation right-handed charged slepton mass

Table 4: The 19 parameters of the pMSSM.

In the pMSSM, gauge eigenstates with equal quantum numbers can mix to form different mass eigenstates. This happens for the higgsinos, gauginos and sfermions. Since the gluino is a color octet fermion, it cannot mix with any other pMSSM particles. An overview of the mass eigenstates in the pMSSM is given in table 5. Its specific content will be discussed in the next paragraphs.

Name	Spin	Gauge Eigenstates	Mass Eigenstates
squarks	0	$\tilde{u}_L, \tilde{u}_R, \tilde{d}_L, \tilde{d}_R$	(same)
		$\tilde{s}_L, \tilde{s}_R, \tilde{c}_L, \tilde{c}_R$	(same)
		$\tilde{t}_L, \tilde{t}_R, \tilde{b}_L, \tilde{b}_R$	$\tilde{t}_1, \tilde{t}_2, \tilde{b}_1, \tilde{b}_2$
sleptons	0	$\tilde{e}_L, \tilde{e}_R, \tilde{\nu}_e$	(same)
		$\tilde{\mu}_L, \tilde{\mu}_R, \tilde{\nu}_\mu$	(same)
		$\tilde{\tau}_L, \tilde{\tau}_R, \tilde{\nu}_\tau$	$\tilde{\tau}_1, \tilde{\tau}_2, \tilde{\nu}_\tau$
Higgs bosons	0	$H_u^0, H_d^0, H_u^+, H_d^-$	$h^0, H^0, A^0, H^\pm$
neutralinos	1/2	$\widetilde{B}^0, \widetilde{W}^0, \widetilde{H}_u^0, \widetilde{H}_d^0$	$\tilde{\chi}_1^0, \tilde{\chi}_2^0, \tilde{\chi}_3^0, \tilde{\chi}_4^0$
charginos	1/2	$\widetilde{W}^\pm, \widetilde{H}_u^+, \widetilde{H}_d^-$	$\tilde{\chi}_1^\pm, \tilde{\chi}_2^\pm$
gluino	1/2	$\tilde{g}$	(same)

Table 5: Overview of the gauge and mass eigenstates of the sparticles in the pMSSM. Adapted from ref. [37].

HIGGS BOSONS

As explained before, after EWSB, five Higgs scalar mass eigenstates (h^0, H^0, A^0, $H^\pm$) remain. The masses of A^0, H^0 and $H^\pm$ (m_{A^0}, m_{H^0} and $m_{H^\pm}$) can be arbitrarily large, whereas the mass of h^0 is bounded from above ($m_{h^0} \lesssim 135$ GeV)[3]. A special situation called the 'decoupling limit' occurs for

---
[3]This is based on the assumption that sparticles that contribute in loop corrections have masses that do not exceed 1 TeV[37].

$m_{A^0} \gg M_Z$, where M_Z denotes the mass of the Z boson. This results in m_{A^0}, m_{H^0} and $m_{H^\pm}$ being very large and $m_{h^0} = \mathcal{O}(M_Z)$. In this situation, the light state h^0 resembles the SM Hhiggs boson, having (nearly) the same couplings to fermions and gauge bosons as the SM Higgs. In the decoupling limit, the couplings of the heavy states A^0 and H^0 come with additional factors $\tan \beta$ (for down-type fermions) and $\tan^{-1} \beta$ (for up-type fermions). For large $\tan \beta$, the hierarchy of these couplings could therefore be altered drastically.

NEUTRALINOS AND CHARGINOS

Due to the effects of EWSB, the higgsinos and electroweak gauginos mix with each other. The neutral higgsinos ($\widetilde{H}_u^0$, $\widetilde{H}_d^0$) and the neutral gauginos ($\widetilde{B^0}$, $\widetilde{W}^0$) combine into four neutral mass eigenstates called 'neutralinos'. The charged higgsinos ($\widetilde{H}_u^+$, $\widetilde{H}_d^-$) and winos ($\widetilde{W}^+$, $\widetilde{W}^-$) mix into two charged mass eigenstates, called 'charginos'. The neutralinos are denoted by $\tilde{\chi}_i^0$ ($i = 1, 2, 3, 4$) and the charginos by $\widetilde{\chi}_i^\pm$ ($i = 1, 2$). By convention these mass eigenstates are labeled such that $m_{\widetilde{\chi}_n^{0,\pm}} < m_{\widetilde{\chi}_{n+1}^{0,\pm}}$. Here $m_{\widetilde{\chi}_j^i}$ denotes the mass of the charginos and neutralinos. The lightest neutralino, $\widetilde{\chi}_1^0$, is usually assumed to be the LSP.

In gauge eigenstate basis $\psi^0 = (\widetilde{B}, \widetilde{W}^0, \widetilde{H}_d^0, \widetilde{H}_u^0)$, the neutralino mass term of the Lagrangian is given by

$$\mathcal{L}_{\text{neutralino mass}} = -\frac{1}{2}(\psi^0)^T \mathbf{M}_{\widetilde{\chi}^0} \psi^0 + \text{c.c.}, \tag{26}$$

where

$$\mathbf{M}_{\widetilde{\chi}^0} = \begin{pmatrix} M_1 & 0 & -M_Z c_\beta s_W & M_Z s_\beta s_W \\ 0 & M_2 & M_Z c_\beta c_W & -M_Z s_\beta c_W \\ -M_Z c_\beta s_W & M_Z c_\beta c_W & 0 & -\mu \\ M_Z s_\beta s_W & -M_Z s_\beta c_W & -\mu & 0 \end{pmatrix}. \tag{27}$$

Here we introduced the abbreviations $s_\beta = \sin \beta$, $c_\beta = \cos \beta$, $s_W = \sin \theta_W$ and $c_W = \cos \theta_W$. By bringing the mass matrix $\mathbf{M}_{\widetilde{\chi}^0}$ into diagonal form, the mass eigenstates ($\widetilde{\chi}_i^0$) can be obtained. A similar approach can be used for the charginos. In gauge eigenstate basis $\psi^\pm = (\widetilde{W}^+, \widetilde{H}_u^+, \widetilde{W}^-, \widetilde{H}_d^-)$, the chargino mass term of the Lagrangian is given by

$$\mathcal{L}_{\text{chargino mass}} = -\frac{1}{2}(\psi^\pm)^T \mathbf{M}_{\widetilde{\chi}^\pm} \psi^\pm + \text{c.c.}, \tag{28}$$

where

$$\mathbf{M}_{\widetilde{\chi}^\pm} = \begin{pmatrix} 0 & 0 & M_2 & \sqrt{2} c_\beta M_W \\ 0 & 0 & \sqrt{2} s_\beta M_W & \mu \\ M_2 & \sqrt{2} s_\beta M_W & 0 & 0 \\ \sqrt{2} c_\beta M_W & \mu & 0 & 0 \end{pmatrix}. \tag{29}$$

Here M_W is the mass of the W boson. Again the mass eigenstates can be obtained by bringing $\mathbf{M}_{\widetilde{\chi}^\pm}$ into diagonal form. Since the eigenvalues of $\mathbf{M}_{\widetilde{\chi}^\pm}$ are doubly degenerate, diagonalization results in two mass eigenstates ($\widetilde{\chi}_i^\pm$) with the same value.[37]

As mentioned before, the neutralinos and charginos are mixtures of the electroweak gauginos and higgsinos. Depending on the relative magnitude and separation of the variables M_1, M_2, μ and β they can have a dominant bino, wino or higgsino component. This causes the particles to be more bino-like, wino-like or higgsino-like. An overview of the different regimes and corresponding dominant neutralino and chargino components is given in table 6.

Regime	Composition neutralinos	Composition charginos
$M_1 < M_2 < |\mu|$	$(\widetilde{B}, \widetilde{W}, \widetilde{H}, \widetilde{H})$	$(\widetilde{W}, \widetilde{H})$
$M_1 < |\mu| < M_2$	$(\widetilde{B}, \widetilde{H}, \widetilde{H}, \widetilde{W})$	$(\widetilde{H}, \widetilde{W})$
$|\mu| < M_1 < M_2$	$(\widetilde{H}, \widetilde{H}, \widetilde{B}, \widetilde{W})$	$(\widetilde{H}, \widetilde{W})$
$|\mu| < M_2 < M_1$	$(\widetilde{H}, \widetilde{H}, \widetilde{W}, \widetilde{B})$	$(\widetilde{H}, \widetilde{W})$
$M_2 < |\mu| < M_1$	$(\widetilde{W}, \widetilde{H}, \widetilde{H}, \widetilde{B})$	$(\widetilde{W}, \widetilde{H})$
$M_2 < M_1 < |\mu|$	$(\widetilde{W}, \widetilde{B}, \widetilde{H}, \widetilde{H})$	$(\widetilde{W}, \widetilde{H})$

Table 6: Dominant components of the neutralinos $(\widetilde{\chi}_1^0, \widetilde{\chi}_2^0, \widetilde{\chi}_3^0, \widetilde{\chi}_4^0)$ and charginos $(\widetilde{\chi}_1^\pm, \widetilde{\chi}_2^\pm)$. Extracted from ref. [27].

SQUARKS AND SLEPTONS

In principle, it is possible for all squarks and sleptons with the same electric charge to mix with each other. However, if $\mu \tan^{-1} \beta$ is small enough, the mixing of the first and second generation squarks and sleptons can be assumed to be negligible in the pMSSM. This means that effectively only mixing of third generation squarks and sleptons takes place. For the stops, the two gauge eigenstates $(\tilde{t}_L, \tilde{t}_R)$ mix into two mass eigenstates $(\tilde{t}_1, \tilde{t}_2)$. The same happens for the sbottom and stau, resulting in mass eigenstates $\tilde{b}_1, \tilde{b}_2$ and $\tilde{\tau}_1, \tilde{\tau}_2$. For small $\tan \beta$ and μ, mixing between the gauge eigenstates is minimal. However, for larger values of $\tan \beta$ the mixing can be significant.

In gauge eigenstate basis $(\tilde{t}_L, \tilde{t}_R)$, the stop mass term of the Lagrangian is given by

$$\mathcal{L}_{\text{stop mass}} = - \begin{pmatrix} \tilde{t}_L^* & \tilde{t}_R^* \end{pmatrix} \mathbf{M}_{\tilde{t}}^2 \begin{pmatrix} \tilde{t}_L \\ \tilde{t}_R \end{pmatrix}, \tag{30}$$

where

$$\mathbf{M}_{\tilde{t}}^2 = \begin{pmatrix} m_{\tilde{Q}_3}^2 + m_t^2 + (\frac{1}{2} - \frac{2}{3} s_W^2) M_Z^2 \cos 2\beta & m_t(A_t - \mu \cot \beta) \\ m_t(A_t - \mu \cot \beta) & m_{\tilde{t}_R}^2 + m_t^2 + \frac{2}{3} s_W^2 M_Z^2 \cos 2\beta \end{pmatrix}. \tag{31}$$

Here the off-diagonal elements are real and $s_W = \sin \theta_W$. The squared-mass matrix can be diagonalized by a rotation matrix which turns the gauge eigenstates $(\tilde{t}_L, \tilde{t}_R)$ into the mass eigenstates $(\tilde{t}_1, \tilde{t}_2)$

$$\begin{pmatrix} \tilde{t}_1 \\ \tilde{t}_2 \end{pmatrix} = \begin{pmatrix} \cos \theta_{\tilde{t}} & -\sin \theta_{\tilde{t}} \\ \sin \theta_{\tilde{t}} & \cos \theta_{\tilde{t}} \end{pmatrix} \begin{pmatrix} \tilde{t}_L \\ \tilde{t}_R \end{pmatrix}. \tag{32}$$

Here $\theta_{\tilde{t}}$ is the stop mixing angle, which can be chosen in the range $0 \leq \theta_{\tilde{t}} < \pi$. The stop mixing angle is given by[13]

$$\sin 2\theta_{\tilde{t}} = \frac{-2m_t(A_t - \mu \cot \beta)}{m_{\tilde{t}_1}^2 - m_{\tilde{t}_2}^2},$$
$$\cos 2\theta_{\tilde{t}} = \frac{m_{\tilde{Q}_3}^2 - m_{\tilde{t}_R}^2 + (\frac{1}{2} - \frac{4}{3} s_W^2) M_Z^2 \cos 2\beta}{m_{\tilde{t}_1}^2 - m_{\tilde{t}_2}^2}, \tag{33}$$

where $m_{\tilde{t}_1}^2$ and $m_{\tilde{t}_2}^2$ are the eigenvalues of equation 31.

A similar analysis can be performed for the sbottoms and staus, for which the mass part of the Lagrangian is of the same form as equation 30. In their respective gauge-eigenstate bases $(\tilde{b}_L, \tilde{b}_R)$ and $(\tilde{\tau}_L, \tilde{\tau}_R)$ they have squared mass matrices

$$\mathbf{M}_{\tilde{b}}^2 = \begin{pmatrix} m_{\tilde{Q}_3}^2 + m_b^2 - (\frac{1}{2} - \frac{1}{3} s_W^2) M_Z^2 \cos 2\beta & m_b(A_b - \mu \tan \beta) \\ m_b(A_b - \mu \tan \beta) & m_{\tilde{b}_R}^2 + m_b^2 - \frac{1}{3} s_W^2 M_Z^2 \cos 2\beta \end{pmatrix}, \tag{34}$$

$$\mathbf{M}_{\tilde{\tau}}^2 = \begin{pmatrix} m_{\tilde{L}_3}^2 + m_\tau^2 - (\frac{1}{2} - s_W^2) M_Z^2 \cos 2\beta & m_\tau(A_\tau - \mu \tan \beta) \\ m_\tau(A_\tau - \mu \tan \beta) & m_{\tilde{\tau}_R}^2 + m_\tau^2 - s_W^2 M_Z^2 \cos 2\beta \end{pmatrix}. \tag{35}$$

Again, the off-diagonal elements are real. In analogy with the stop, these squared-mass matrices can be diagonalized to find the mass eigenstates $(\tilde{b}_1, \tilde{b}_2)$ and $(\tilde{\tau}_1, \tilde{\tau}_2)$.[37] The respective mixing angles are given by[13][25]

$$\sin 2\theta_{\tilde{b}} = \frac{-2m_b(A_b - \mu \tan \beta)}{m_{\tilde{b}_1}^2 - m_{\tilde{b}_2}^2},$$

$$\cos 2\theta_{\tilde{b}} = \frac{m_{\tilde{Q}_3}^2 - m_{\tilde{b}_R}^2 - (\frac{1}{2} - \frac{2}{3}s_W^2)M_Z^2 \cos 2\beta}{m_{\tilde{b}_1}^2 - m_{\tilde{b}_2}^2},$$

(36)

and

$$\sin 2\theta_{\tilde{\tau}} = \frac{-2m_\tau(A_\tau - \mu \tan \beta)}{m_{\tilde{\tau}_1}^2 - m_{\tilde{\tau}_2}^2},$$

$$\cos 2\theta_{\tilde{\tau}} = \frac{m_{\tilde{L}_3}^2 - m_{\tilde{\tau}_R}^2 - (\frac{1}{2} - 2s_W^2)M_Z^2 \cos 2\beta}{m_{\tilde{\tau}_1}^2 - m_{\tilde{\tau}_2}^2}.$$

(37)

3 The process $B_s^0 \to \mu^+\mu^-$

This chapter describes the process $B_s^0 \to \mu^+\mu^-$. First, an introduction to B-physics and the B_s^0 meson is given, followed by a discussion of the relevance of this process in the search for new physics. Next a detailed explanation of $B_s^0 - \bar{B}_s^0$ mixing and the different types of branching ratios (BRs) is given, followed by an overview of the dominant Feynman diagrams within the SM and the pMSSM. The chapter concludes with a derivation of the BR for $B_s^0 \to \mu^+\mu^-$ by means of an effective field theory (EFT).

3.1 Searching for new physics

In flavour physics, B-physics refers to processes that concern B-mesons. These mesons consist of an (anti-)bottom quark and any other (anti-)quark. They can be charged or neutral, depending on the quark type. One of the neutral B-mesons is the B_s^0 particle, which consists of an anti-bottom and a strange quark ($\bar{b}s$). It has a mass of 5.37 GeV and a mean lifetime of 1.510 ps. Its main decay mode is to a D_s^- meson accompanied by anything else. This mode comprises a branching fraction of 93%.[26]

Another possible decay mode of the B_s^0 meson is to a muon-anti-muon pair. This process is very interesting for the search for possible new sources of FCNC decays. Since it is a FCNC decay, it has no contributions at the three level within the SM, and is therefore suppressed. Next to this, it is also CKM suppressed since it contains at least one off-diagonal element of the CKM matrix (for a detailed description of the CKM matrix see appendix A). Last but not least, the process is also helicity suppressed. This is because the B_s^0 meson is a spin-0 particle. Due to momentum conservation, the muon and anti-muon travel in opposite directions when the meson decays in its rest frame, and hence have the same helicity. For massless particles, the helicity is the same as the chirality. Therefore, in the case of a massless anti-muon and muon, having the same chirality, the decay can not take place. This is because the weak force only couples to left-handed particles (and right-handed anti-particles). However, since (anti-)muons are massive, the decay does take place. This is possible, because due to the particles being massive, their helicity can differ from their chirality. The corresponding decay amplitude includes a mass insertion that changes the helicity of one of the particles. This leads to a decay amplitude which is proportional to the muon mass. Since this mass is very small, the decay is suppressed.

The various kinds of suppression result in a very small BR and therefore the process is referred to as a 'rare decay'. However, within specific extensions of the SM, the decay may receive large enhancements, leading to a larger BR. In these extensions, the helicity suppression may be lifted, less off-diagonal CKM elements may be involved, or the process could occur at the three level. In addition, the transition $B_s^0 \to \mu^+\mu^-$ is a very clean process. This is because its final muon-antimuon state is easily tagged in experiments and the largest uncertainty comes from the hadronic decay constant (which can be calculated by means of non-perturbative QCD[3], an example will be given in section 3.4.1). In combination with the possibility of large BR enhancements, this makes the muon-anti-muon decay channel a very interesting probe to look for new physics.[5][33]. Such scenarios of new physics could, next to BR enhancement, also lead to new CP violating phases[4]. However, in this thesis, we will study the BR of the transition $B_s^0 \to \mu^+\mu^-$ within the pMSSM. This means that we will neglect all new sources of CP violation.

3.2 B_s^0-$\bar{B}_s^0$ mixing

An important feature of B_s^0 mesons is that they mix with their anti-particles. Within the SM, this mixing arises from the box diagrams shown in figure 1, and leads to time-dependent oscillations between the B_s^0 and $\bar{B}_s^0$ states. This section describes the Schrödinger equation for B_s^0-$\bar{B}_s^0$ mixing, introduces important mixing parameters and derives the time-dependent decay rate for B_s^0 mesons.

3.2.1 Schrödinger equation for B_s^0-$\bar{B}_s^0$ mixing

Without mixing, the time evolution of a B_s^0 meson can be described as

$$|B_s^0(t)\rangle = |B_s^0(0)\rangle\, e^{-iHt}, \qquad H = M - \frac{i\Gamma}{2}, \tag{38}$$

---

[4]For a detailed description of this CP violating new physics the reader is referred to ref. [34] and [33].
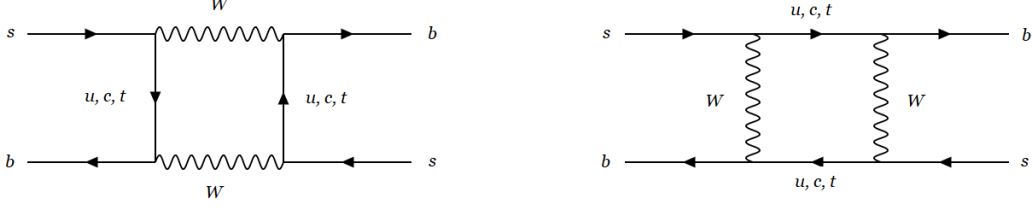
Figure 1: Box diagrams contributing to B_s^0-$\bar{B}_s^0$ mixing in the SM.

where $|B_s^0(0)\rangle$ denotes the state of the meson at $t = 0$, H is the Hamiltonian, M is the mass of the B_s^0 meson and Γ its decay width. An equivalent equation exists for $\bar{B}_s^0$.

If mixing is included, the time evolution of the B_s^0-$\bar{B}_s^0$ system is governed by a Schrödinger equation of the following form

$$i\frac{d\psi(t)}{dt} = H\psi(t), \qquad \text{with } \psi(t) = \begin{pmatrix} |B_s^0(t)\rangle \\ |\bar{B}_s^0(t)\rangle \end{pmatrix}. \tag{39}$$

Here, $|B_s^0(t)\rangle$ denotes the state of a meson initially produced as a B_s^0. Analogously, $|\bar{B}_s^0(t)\rangle$ denotes the state of a meson initially produced as a $\bar{B}_s^0$. The Hamiltonian matrix H is defined as

$$H = M - i\frac{\Gamma}{2} = \begin{pmatrix} M_{11} - i\frac{\Gamma_{11}}{2} & M_{12} - i\frac{\Gamma_{12}}{2} \\ M_{21} - i\frac{\Gamma_{21}}{2} & M_{22} - i\frac{\Gamma_{22}}{2} \end{pmatrix}. \tag{40}$$

The mass matrix M and decay matrix Γ are hermitian matrices with positive eigenvalues. For the off-diagonal elements we can write $M_{12} = M_{21}^*$ and $\Gamma_{12} = \Gamma_{21}^*$ and as a result of the CPT theorem[5], we can define $M_{11} = M_{22} = M$ and $\Gamma_{11} = \Gamma_{22} = \Gamma$[32]. Substituting this in equations 39 and 40, we arrive at

$$i\frac{d}{dt}\begin{pmatrix} |B_s^0(t)\rangle \\ |\bar{B}_s^0(t)\rangle \end{pmatrix} = \begin{pmatrix} M - i\frac{\Gamma}{2} & M_{12} - i\frac{\Gamma_{12}}{2} \\ M_{12}^* - i\frac{\Gamma_{12}^*}{2} & M - i\frac{\Gamma}{2} \end{pmatrix}\begin{pmatrix} |B_s^0(t)\rangle \\ |\bar{B}_s^0(t)\rangle \end{pmatrix}. \tag{41}$$

The mass eigenstates at $t = 0$ are linear combinations of $|B_s^0\rangle$ and $|\bar{B}_s^0\rangle$

$$|B_L\rangle = a\,|B_s^0\rangle + b\,|\bar{B}_s^0\rangle\,, \qquad |B_H\rangle = a\,|B_s^0\rangle - b\,|\bar{B}_s^0\rangle\,, \qquad \text{with } |a|^2 + |b|^2 = 1.$$

It is common to denote the two eigenstates by B_H and B_L where 'H' stands for 'heavy' and 'L' for 'light'. Both states differ in their masses (M_H and M_L) and their decay widths (Γ_H and Γ_L). It is useful to introduce the following quantities:

$$
\begin{aligned}
M &\equiv \frac{M_H + M_L}{2}, \\
\Delta M &\equiv M_H - M_L, \\
\Gamma &\equiv \frac{\Gamma_H + \Gamma_L}{2} = \frac{1}{\tau_{B_s}}, \\
\Delta\Gamma &\equiv \Gamma_L - \Gamma_H, \\
y_s &\equiv \frac{\Delta\Gamma}{2\Gamma}.
\end{aligned}
\tag{42}
$$

Here, τ_{B_s} is the lifetime of the B_s^0 meson, and y_s is the decay width parameter, which is related to the lifetime[32]. By definition, the mass difference of the heavy and light eigenstates (ΔM) is positive. The decay width difference of the two eigenstates ($\Delta\Gamma$) can be either positive or negative. Here, we choose it to be positive in the SM. If we assume that $|\Gamma_{12}| \ll |M_{12}|$ and expand the masses, decay widths and b/a in Γ_{12}/M_{12}, we find[22]

---

[5]This theorem implies invariance under combined CP and time-reversal (T) transformations. For a detailed description see ref. [21].

$$\Delta M = 2|M_{12}|, \qquad \Delta\Gamma = 2|\Gamma_{12}|\cos\phi, \qquad \frac{b}{a} = -e^{-i\phi_M}\left[1 - \frac{p}{2}\right]. \tag{43}$$

Here, $\phi_M = \arg M_{12}$ is called the mixing phase. In the equation for b/a we have neglected all terms of order Γ_{12}^2/M_{12}^2. The phase ϕ and parameter p are defined as

$$\frac{M_{12}}{\Gamma_{12}} = -\left|\frac{M_{12}}{\Gamma_{12}}\right|e^{i\phi}, \qquad p = \left|\frac{\Gamma_{12}}{M_{12}}\right|\sin\phi. \tag{44}$$

Here, p is assumed to be small.[6]. For the decay of a B_s^0 or $\bar{B}_s^0$ into a final state f, we define

$$A_f = \langle f|B_s^0\rangle, \qquad \bar{A}_f = \langle f|\bar{B}_s^0\rangle, \qquad \lambda_f = \frac{b}{a}\frac{\bar{A}_f}{A_f}, \tag{45}$$

where A_f and $\bar{A}_f$ are the unevolved decay widths, which will be used in the next section to derive the time dependent decay widths.

3.2.2 Time dependent decay width

We can define the time dependent decay width of an initial B_s^0 meson into a final state f as

$$\Gamma(B_s^0(t) \to f) = \frac{1}{N_B}\frac{dN\big(\Gamma(B_s^0(t) \to f)\big)}{dt}, \tag{46}$$

here N_B is the total number of B_s^0's produced at time $t = 0$, $B_s^0(t)$ represents a meson at time t, initially produced as a B_s^0, and $dN\big(\Gamma(B_s^0(t) \to f)\big)$ denotes the number of decays of $B_s^0(t)$ into the final state f within the time interval $[t, t+dt]$. The time dependent decay of an initial $\bar{B}_s^0$ can be defined in an analogous way.

By solving the Schrödinger equation in equation 41, and using the relations in equations 42 and 43, we arrive at the time dependent decay widths[22]

$$\begin{aligned}
\Gamma(B_s^0(t) \to f) &= \mathcal{N}_f|A_f|^2\frac{1+|\lambda_f|^2}{2}e^{-\Gamma t} \\
&\times \left[\cosh\frac{y_s t}{\tau_{B_s}} + \frac{1-|\lambda_f|^2}{1+|\lambda_f|^2}\cos(\Delta M t) + \mathcal{A}_{\Delta\Gamma}\sinh\frac{y_s t}{\tau_{B_s}} + \frac{2\mathrm{Im}\lambda_f}{1+|\lambda_f|^2}\sin(\Delta M t)\right], \\
\Gamma(\bar{B}_s^0(t) \to f) &= \mathcal{N}_f|A_f|^2\frac{1+|\lambda_f|^2}{2}(1+p)e^{-\Gamma t} \\
&\times \left[\cosh\frac{y_s t}{\tau_{B_s}} - \frac{1-|\lambda_f|^2}{1+|\lambda_f|^2}\cos(\Delta M t) + \mathcal{A}_{\Delta\Gamma}\sinh\frac{y_s t}{\tau_{B_s}} - \frac{2\mathrm{Im}\lambda_f}{1+|\lambda_f|^2}\sin(\Delta M t)\right].
\end{aligned} \tag{47}$$

Here, $\mathcal{N}_f$ is a time-independent factor used for normalization and $\mathcal{A}_{\Delta\Gamma}$ is defined as

$$\mathcal{A}_{\Delta\Gamma} = -\frac{2\mathrm{Re}\lambda_f}{1+|\lambda_f|^2}. \tag{48}$$

Note that the time-dependent decay widths in equation 47 are functions of the unevolved decay width (A_f).

3.2.3 Untagged decay width

In a situation without knowledge about the initial state being a B_s^0 or $\bar{B}_s^0$ meson, the total decay width can be expressed as a combination of the decay widths of both particles to the same final state f. This is called the untagged decay width and it is given by

$$\langle\Gamma(B_s(t) \to f)\rangle \equiv \frac{1}{2}\left[\Gamma(B_s^0(t) \to f) + \Gamma(\bar{B}_s^0(t) \to f)\right]. \tag{49}$$

---

[6]The value of p can hardly exceed 0.01[?].

Here, $B_s(t)$ contains both $B_s^0(t)$ and $\bar{B}_s^0(t)$. By inserting the time dependent decay widths from equation 47 we find

$$\langle \Gamma(B_s(t) \to f) \rangle = \frac{1}{2} \mathcal{N}_f |A_f|^2 (1 + |\lambda_f|^2) e^{-\Gamma t} \left[\cosh \frac{y_s t}{\tau_{B_s}} + \mathcal{A}_{\Delta\Gamma} \sinh \frac{y_s t}{\tau_{B_s}} \right] + \mathcal{O}(p). \tag{50}$$

In experiments it is hard to tag the initial state of the B_s meson. This is because it requires further analysis of side-products of the decay to find out if the initial state was a B_s^0 or $\bar{B}_s^0$ particle. In some cases, for instance when it comes to the analysis of CP asymmetries, information about the initial state is necessary. However, for the cases in which tagging is not necessary, the untagged decay width is the preferred observable.

3.2.4 Theoretical and time-integrated BR

A further distinction can be made concerning the process $B_s \to f$, as we can choose whether we do or do not take time-evolution into account. This results in two different BRs: the theoretical BR and the time-integrated BR. In the first case, time evolution is not taken into account, and, therefore the effects of B_s^0-$\bar{B}_s^0$ mixing are 'switched off'. This BR is evaluated at $t = 0$ and for the initial state a pure, unevolved B_s^0 or $\bar{B}_s^0$ state is used. On the other hand, for the time-integrated BR, there is mixing of the two neutral states. This BR is based on the time-dependent decay width and is evaluated by integrating over the whole duration of the decay. Since mixing cannot be switched off in an experiment, it is the time-integrated BR that we need to compute for a prediction.

The time-integrated BR can be defined as

$$\mathrm{BR}(B_s \to f)_{\text{time-integrated}} \equiv \bar{\mathcal{B}}(B_s \to f) \equiv \int_0^\infty \langle \Gamma(B_s(t) \to f) \rangle \mathrm{dt}. \tag{51}$$

Upon insertion of equation 50 and performing the integral we find

$$\mathrm{BR}(B_s \to f)_{\text{time-integrated}} = \frac{\tau_{B_s}}{2} \mathcal{N}_f |A_f|^2 (1 + |\lambda_f|^2) \left[\frac{1 + \mathcal{A}_{\Delta\Gamma} y_s}{1 - y_s^2} \right] + \mathcal{O}(p). \tag{52}$$

The theoretical BR can be calculated by[23]

$$\mathrm{BR}(B_s \to f)_{\text{theoretical}} \equiv \tau_{B_s} \langle \Gamma(B_s(t) \to f) \rangle \Big|_{t=0}. \tag{53}$$

Upon insertion of equation 50 and setting $t = 0$ we find

$$\mathrm{BR}(B_s \to f)_{\text{theoretical}} = \frac{\tau_{B_s}}{2} \mathcal{N}_f |A_f|^2 (1 + |\lambda_f|^2) + \mathcal{O}(p) \tag{54}$$

Neglecting the $\mathcal{O}(p)$ contribution, we can convert the time-integrated BR into the theoretical BR by means of the following equation

$$\mathrm{BR}(B_s \to f)_{\text{theoretical}} = \left[\frac{1 - y_s^2}{1 + \mathcal{A}_{\Delta\Gamma} y_s} \right] \mathrm{BR}(B_s \to f)_{\text{time-integrated}} \tag{55}$$

In the case of $y_s = 0$ (i.e. a zero decay width difference between the light and heavy state), the theoretical and time-integrated BRs are equal [23]. The notation $\mathrm{BR}(B_s \to f)$ is used to denote the untagged theoretical BR and $\bar{\mathcal{B}}(B_s \to f)$ to refer to the untagged time-integrated BR.

3.3 Feynman diagrams and important parameters

For the transition $B_s^0 \to \mu^+ \mu^-$, the diagrammatic contributions can be decomposed into box, Z penguin and Higgs penguin diagrams as can be seen in figure 2. The photon penguin contribution vanishes due to the Ward identity, which will be derived in section 3.4.2. This section gives an overview of the lowest order (LO) SM diagrams and the dominant pMSSM contributions. Based upon these diagrams, a set of important pMSSM parameters that influence the process is derived.
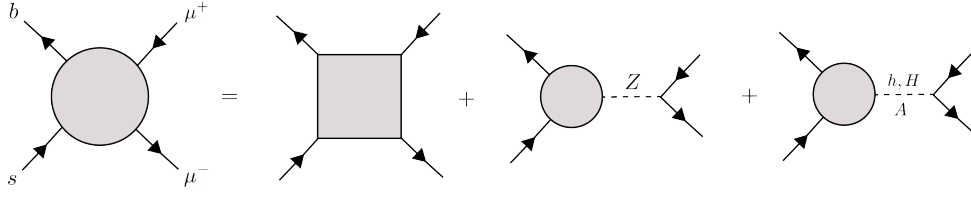
Figure 2: Decomposition of the diagrams contributing to the transition $B_s^0 \to \mu^+\mu^-$. From left to right: box diagram, Z penguin diagram, Higgs penguin diagram.[3].

SM diagrams

The LO contributions to the transition $B_s^0 \to \mu^+\mu^-$ in the SM are displayed in figure 3.
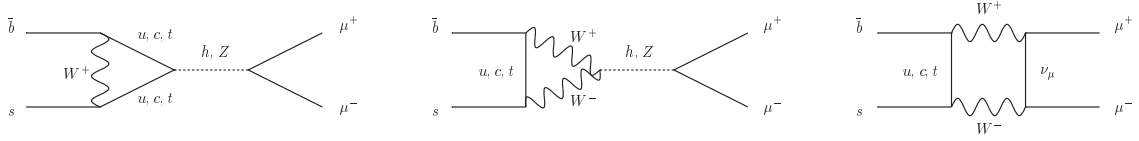

Figure 3: Lowest order diagrams within the SM.

pMSSM diagrams

In the pMSSM, new particles can enter the box and penguin topologies. An overview of the dominant LO diagrams contributing to $B_s^0 \to \mu^+\mu^-$ is given in figure 4.
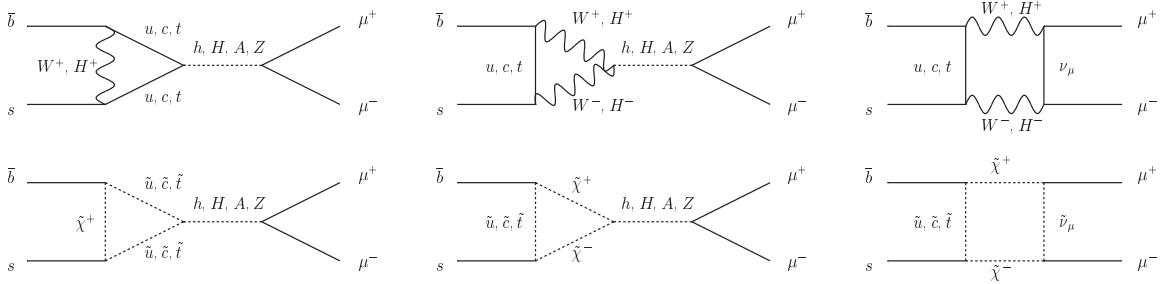

Figure 4: Dominant lowest order diagrams within the pMSSM.[2]

3.3.1   Important pMSSM parameters

Based on the dominant pMSSM diagrams, we can argue which of the 19 pMSSM parameters will contribute in a significant way to the BR. By looking at the diagrams in figure 4 we encounter diagrams that contain neutral and charged Higgs particles. This hints at μ, $\tan\beta$ and m_A being parameters of interest. Next to this, the presence of charginos tells us that, in addition, the wino mass parameter, M_2, might play an important role. Lastly, the up-type squarks that appear in the diagrams point at the trilinear coupling A_t and the squark masses $m_{\tilde{Q}_1}$, $m_{\tilde{Q}_3}$, $m_{\tilde{u}_R}$ and $m_{\tilde{t}_R}$ as important parameters. Although this short analysis gives us some insight into the behavior of the process within the pMSSM, we should stress that it is only based on the dominant, lowest order diagrams and is therefore only a first order approximation. We will use this approximation as a starting point for our analysis of the BR behavior in chapter 6.1.

3.4   Branching ratio calculation of $B_s^0 \to \mu^+\mu^-$

In this section we will derive the BR equation for $\bar{B}_s^0 \to \mu^+\mu^-$. We start by introducing the concept of an effective theory and explain how this can be used to describe weak hadronic decays. Next, we perform a derivation of the BR using this concept. We will start from the effective Hamiltonian, calculate the matrix element and use this result to arrive at the expression for the BR. From this general equation we will

derive the SM BR expression. Next to this, the differences between the theoretical and time-integrated BR are explained. To conclude, an experimentally obtained value and a calculated SM prediction of the BR are provided.

3.4.1 EFT approach

In physics, processes happen at many different scales. Since a description of a theory for the whole range of scales can be complex, or is sometimes unknown, we can make the decision to focus on a specific regime. By doing this, we can describe the phenomena that occur at specific scales without having to know the full underlying physics model. Such a description is called 'effective theory'. In order to simplify the description of the phenomena occurring at the selected scale range, the following approach is used: parameters that are very small compared to the quantities of interest at the chosen scale are set to zero, whereas parameters that are very large compared to these quantities are set to infinity. Afterwards, the finite effects of these parameters are included as small perturbations[20]. An example of such an effective theory is Newtonian mechanics, which is just the small velocity limit of relativistic mechanics. Though, in this case, we are familiar with the full theory, it is sometimes just easier to leave relativity out. This illustrates the underlying principle of an effective theory.

For a quantum field theory, the relevant parameter is energy (or distance). If it is possible to separate the theories at different scales, we can use an effective field theory (EFT) to describe the physics at a specific scale. For an EFT to work, there must be a significant separation between the energy scale of interest and the energy scale of the full theory. With respect to the concept of an effective theory, for an EFT, the parameters of interest are particle masses. If an EFT is used to describe physics up to a certain energy scale, all particle masses that are much larger than this scale are set to infinity and the finite size effects are included as perturbations. This is referred to as 'integrating out' these heavy particles. For the EFT to work, we must be able to perform this step (i.e. the decoupling theorem must hold). The scale up to which an EFT describes physics determines which particles are integrated out and which particles are included in the EFT. Each particle mass can therefore be linked to a boundary between two EFTs. For energies above this boundary, the EFT includes the particle, whereas for energies below the boundary, the particle is integrated out. The physics just below the boundary must be the same as just above it. At LO this comes down to the requirement that the coupling constants for the interactions of the particles that are not integrated out are continuous across the boundary[20]. To link the two EFTs, these coupling constants have to be related to the parameters of the underlying physics model[7]. This process is called 'matching'.

Figure 5 illustrates the concept of an EFT. We start at a large scale μ, where the physics is described by a high-energy theory. This high-energy theory contains a set of heavy particles with mass M, which are described by the fields χ. Next to this, the theory contains a set of light particles which are described by the fields ϕ and have mass m. The Lagrangian for this theory can be written as $\mathcal{L}_H(\chi, \phi) + \mathcal{L}(\phi)$. Here, the second term includes contributions that only depend on the light particles, whereas the other term also describes the heavy particles. By means of renormalization group equations, the theory can be evolved to lower scales. If the scale reaches the value of the heavy particle mass M, the high-energy theory should be changed to an EFT, in which the heavy particles are integrated out. The result is a low-energy EFT which has a Lagrangian of the form $\mathcal{L}(\phi) + \delta\mathcal{L}(\phi)$. Here, the term for the heavy particles is removed and the term $\delta\mathcal{L}(\phi)$ is added. This new term represents all the changes that are made by going from the high-energy theory to the EFT[20]. To match the two theories, $\delta\mathcal{L}(\phi)$ has to be chosen such that the physics described by the two theories matches at the boundary scale $\mu = M$. This results in a set of so called 'matching conditions'. It is important to note that the matching scale does not exactly have to resemble the value of the heavy particle mass, but can be chosen with a certain freedom. Note that this choice affects calculations performed within the EFT. As a rule of thumb, the matching scale is usually chosen between $\frac{1}{2}$ and $2M$.
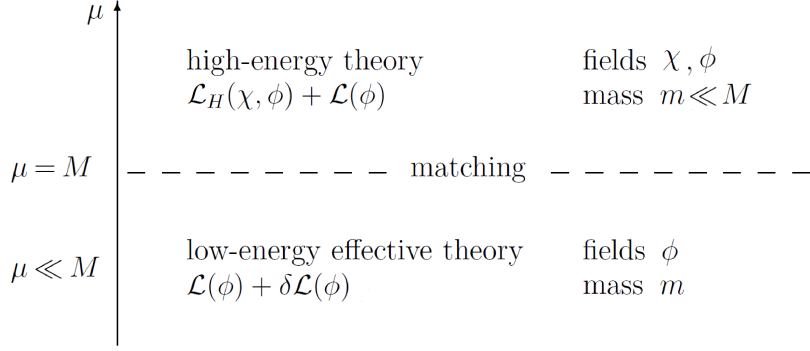
Figure 5: Schematic view of the concept of an EFT. A high-energy theory, containing heavy particles χ with mass M and light particles ϕ with mass $m \ll M$ is displayed. After lowering the scale μ below M and integrating out the heavy particles, a low-energy EFT is left. Matching of the two theories takes place at a scale $\mu = M$. Adapted from ref. [7].

Example: Fermi theory of weak interactions

The theoretical description of EFTs in particle physics given above is rather abstract, therefore we will consider an explicit example: the Fermi theory of weak interactions. We consider the process $b \to c d \bar{u}$. A Feynman diagram for the full theory is presented on the left-hand side of figure 6. The decay amplitude for the process contains a factor $g^2/(p^2 - M_W^2)$, where g is the coupling constant of the weak interaction, M_W the mass of the W boson and p its four-momentum. At the typical hadronic energy scale of the decay process, $\mathcal{O}(1\text{ GeV})$, the momentum carried by the W boson is much smaller than its mass, which is around 80 GeV. Therefore the propagator factor can be expanded as

$$\frac{g^2}{p^2 - M_W^2} \xrightarrow{p^2 \ll M_W^2} -\frac{g^2}{M_W^2} + \mathcal{O}\left(\frac{p^2}{M_W^4}\right) \tag{56}$$

In a diagrammatic representation, this corresponds to the right-hand side of figure 6. Here, the W boson is integrated out and the short distance physics of the W boson is hidden into a point-like four-vertex with an effective coupling G_F (Fermi coupling). On the basis of such low energy decay processes, Fermi postulated the existence of four particle interactions (1930s)[36]. From our present knowledge we now know that this was just an EFT description of the theory of weak interactions.
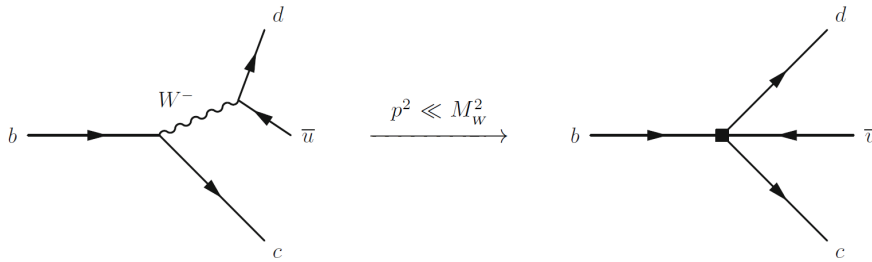

Figure 6: Example of the Fermi theory in which the W boson is integrated out of the full theory (left) and an effective theory (right) remains.

EFT for weak hadronic decays

Weak decays of hadrons are mediated by weak interactions among quarks. The strong interactions binding the quarks into hadrons are, as mentioned in the previous example, characterized by a typical hadronic energy scale of $\mathcal{O}(1\text{ GeV})$. Since this scale is much lower than the scale of electroweak interactions, $\mathcal{O}(M_{weak} \approx 100\text{ GeV})$, we can describe the hadronic decays by an EFT. Similar to the Fermi theory example, in such an EFT, the W boson and all heavier particles are integrated out and a low-energy EFT remains.[17]

To construct the EFT, we make use of the Operator Product Expansion (OPE). By using the OPE we can write the Hamiltonian for the effective theory ($\mathcal{H}_{\text{eff}}$) as a series expansion of local operators O_i, whose contributions are weighted by effective couplings C_i [7]

$$\mathcal{H}_{\text{eff}} = \frac{G_F}{\sqrt{2}} \lambda_{\text{CKM}} \sum_i C_i(\mu) O_i(\mu), \tag{57}$$

where λ_{CKM} represents the CKM matrix elements and G_F is the Fermi coupling. The local operators and effective couplings are evaluated at a scale μ. By making use of the OPE technique, we have separated the Hamiltonian in two parts: one that accounts for the low energy (long distance) and the other for the high energy (short distance) contributions. The high energy part contains the perturbative contributions and is parameterized by the effective couplings $C_i(\mu)$, also referred to as Wilson coefficients. The low energy contributions are non-perturbative quantities and are described by the local operators $O_i(\mu)$. The contributions of the particles that are integrated out are included in the Wilson coefficients. In order to find the expressions for the Wilson coefficients, we have to match the decay amplitude of the full theory to the EFT at the matching scale. For weak hadronic decays this matching scale is of $\mathcal{O}(M_W)$. The matching can be performed in three steps:

1. Calculate the decay amplitude in the full theory, A_{full}.

2. Calculate the local operator matrix elements, $\langle O_i \rangle$.

3. Extract the Wilson coefficients by inserting the calculated matrix elements $\langle O_i \rangle$ in the equation for the effective amplitude (A_{eff}) and comparing this to the calculated A_{full}:

$$A_{\text{full}} = A_{\text{eff}} = \frac{G_F}{\sqrt{2}} \lambda_{\text{CKM}} \sum_i C_i \langle O_i \rangle. \tag{58}$$

This provides us with the expressions for the Wilson coefficients, which generally depend logarithmically on the matching scale and the masses of the particles that are integrated out. The coefficients can be used for calculations at and below a scale $\mu = \mathcal{O}(M_W)$. If we want to perform calculations at the hadronic scale, for which $\mu \ll M_W$, we have to evolve the Wilson coefficients to this scale by means of renormalization group equations. To be able to perform the calculations, also the matrix elements $\langle O_i \rangle$ have to be evaluated at this low energy scale. In the next section we will give a description of the matrix elements $\langle O_i \rangle$ and explain how they can be calculated at the hadronic scale.

3.4.2 Branching ratio of $\bar{B}_s^0 \to \mu^+ \mu^-$

Since the process $\bar{B}_s^0 \to \mu^+ \mu^-$ concerns a weak hadronic decay, we use an EFT to describe it[8]. Among the particles that are integrated out there can be particles that are not described by the SM. A diagrammatic example is provided in figure 7.
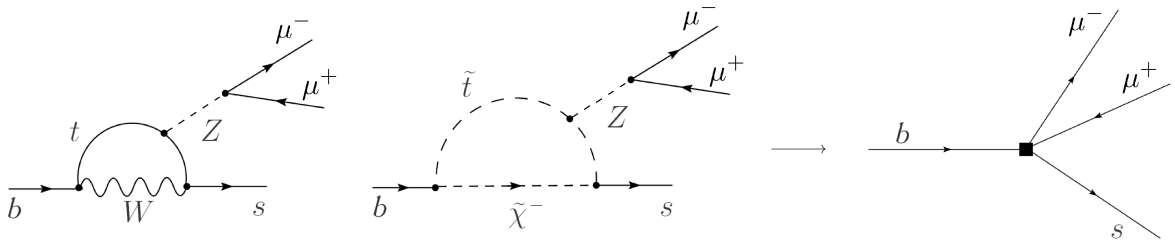
Figure 7: Example of an EFT for the process $b \to s\mu^+\mu^-$. The left side shows two diagrams of the full theory. The right shows the effective theory, where the heavy particles (W, Z, t, $\widetilde{\chi}^-$, $\widetilde{t}$) are integrated out, and a four-point interaction is left. This interaction is described by local operators O_i and Wilson coefficients C_i.

---

[7] For a step by step derivation, the reader is referred to ref.[4].

[8] Note that this derivation is done for the anti-B_s^0 meson. The derivation for B_s^0 is similar.

To derive an equation for the branching ratio of $\bar{B}_s^0 \to \mu^+\mu^-$, we start from the effective Hamiltonian that describes the more general decay to two leptons. The effective Hamiltonian for this process is given by

$$\mathcal{H}_{\text{eff}} = -\frac{4G_F}{\sqrt{2}}V_{tb}V_{ts}^*\big[C_{10}O_{10} + C_S O_S + C_P O_P + C_{10}'O_{10}' + C_S'O_S' + C_P'O_P'\big], \tag{59}$$

where V_{ti} are the CKM matrix elements, $C_i^{(')}$ are the relevant Wilson coefficients and $O_i^{(')}$ the corresponding local operators. The subscripts '10', 'S' and 'P' refer to the names of the operators and couplings, with 'S' for 'scalar' and 'P' for 'pseudo-scalar'. Within the SM all local operators, except for O_{10}, are negligible[11]. The S, P and primed operators are added to the effective Hamiltonian to be able to study effects of new physics. In writing this equation, the unitarity of the CKM matrix is used and terms proportional to $V_{ub}V_{us}^*/V_{tb}V_{ts}^* \sim \mathcal{O}(10^{-2})$ are omitted[10].

The four-fermion operators that govern the decay are given by[34][10]

$$\begin{aligned}
O_{10} &= \frac{e^2}{(4\pi)^2}(\bar{s}\gamma^\mu P_L b)(\bar{\ell}\gamma_\mu\gamma_5\ell), & O_{10}' &= \frac{e^2}{(4\pi)^2}(\bar{s}\gamma^\mu P_R b)(\bar{\ell}\gamma_\mu\gamma_5\ell), \\
O_S &= \frac{e^2}{(4\pi)^2}m_b(\bar{s}P_R b)(\bar{\ell}\ell), & O_S' &= \frac{e^2}{(4\pi)^2}m_s(\bar{s}P_L b)(\bar{\ell}\ell), \\
O_P &= \frac{e^2}{(4\pi)^2}m_b(\bar{s}P_R b)(\bar{\ell}\gamma_5\ell)\,, & O_P' &= \frac{e^2}{(4\pi)^2}m_s(\bar{s}P_L b)(\bar{\ell}\gamma_5\ell).
\end{aligned} \tag{60}$$

Here, $P_{L,R} = \frac{1}{2}(1 \mp \gamma_5)$ are the chiral projection operators and b, s, ℓ correspond to the external spinors of the initial state quarks and final state leptons. The operator O_{10} originates from the box and penguin diagrams in figure 3. The operators $O_{S,P}$ originate from the additional diagrams that appear when we consider the pMSSM instead of the SM (see figure 4). The primed operators $O_{S,P}'$ and O_{10}' are the chirality flipped partners of the unprimed operators. If we consider the objects that could be constructed using Dirac matrices, we could argue that contributions of the tensor operator ($\sigma^{\mu\nu}$) are missing. However, contributions of this operator vanish, since the only available four-vector is the momentum of the $\bar{B}_s^0$. It follows that it is not possible to construct an anti-symmetric tensor out of a single momentum, hence the tensor operator structure does not appear. The operators in equation 60 can be written in the form $O_i = \text{constants} \cdot O_Q^i \cdot O_\ell^i$, where $O_{Q,\ell}^i$ refer to the hadronic (Q) and leptonic (ℓ) parts.

The decay amplitude for $\bar{B}_s^0 \to \ell^+\ell^-$ can be calculated by

$$\langle \ell^+\ell^-|\,\mathcal{H}_{\text{eff}}\,|\bar{B}_s^0(p)\rangle = \frac{-4G_F}{\sqrt{2}}\frac{e^2}{(4\pi)^2}V_{tb}V_{ts}^* \sum_{i=10,10',S,S',P,P'} C_i\,\langle \ell^+\ell^-|\,O_\ell^i\,|0\rangle\,\langle 0|\,O_Q^i\,|\bar{B}_s^0(p)\rangle\,, \tag{61}$$

where on the right hand side the contributions are decomposed in a product of the amplitudes between the external states and the vacuum with respect to the effective hadronic (O_Q^i) and leptonic (O_ℓ^i) parts.

We can write the hadronic matrix elements in the form $\langle 0|\,\bar{s}\Gamma_a b\,|B_s^0(p)\rangle$. Due to the pseudo-scalar nature of the B_s^0 meson, these matrix elements vanish for $\Gamma_a = I$ and $\Gamma_a = \gamma^\mu$. The two hadronic matrix elements that are then relevant for this process are the ones with $\Gamma_a = \gamma_5$ and $\Gamma_a = \gamma_\mu\gamma_5$. They are given by[12]

$$\begin{aligned}
\langle 0|\,\bar{s}\gamma_\mu\gamma_5 b\,|\bar{B}_s^0(p)\rangle &= ip_\mu f_{B_s}, \\
\langle 0|\,\bar{s}\gamma_5 b\,|\bar{B}_s^0(p)\rangle &= -if_{B_s}\frac{M_{B_s}^2}{m_b + m_s}.
\end{aligned} \tag{62}$$

Here, f_{B_s} is the decay constant of the $\bar{B}_s^0$ meson, M_{B_s} its mass and p_μ its momentum. The bottom and strange quark masses are given by m_b and m_s respectively. The decay constant can be determined by non-perturbative methods such as the QCD sum rule approach[9][26]. It is necessary to use such a non-perturbative technique for low scale calculations, since QCD can only be treated in a perturbative way at high energies. By using the QCD sum rule method to calculate the decay constant, generally, only a 10-20% accuracy can be expected[6]. The calculation of this parameter at the hadronic scale, therefore causes large uncertainties with respect to the total low energy calculation.[4][32] By contracting

---

[9]For a detailed description of this method the reader is referred to ref. [29].

both sides of the first line with the momentum of the decaying $\bar{B}_s^0$ meson, and using the quark equations of motion, the second expression is found. Because of the Ward identity for on shell leptons, we have that $p_\mu(\bar{\ell}\gamma^\mu\ell) = 0$. This means that the operator $\langle 0|\, \bar{s}\gamma_\mu\gamma_5 b\, |\bar{B}_s^0(p)\rangle$ vanishes when contracted with the leptonic vector current ($\bar{\ell}\gamma^\mu\ell$). This is why the photon penguin contribution to the process vanishes.

By inserting the hadronic matrix elements in equation 61 we can write the matrix element as

$$
\begin{aligned}
\mathcal{M} &= \frac{-G_F\alpha}{\sqrt{2}\pi} V_{tb}V_{ts}^* \Bigg[\frac{i}{2} p^\mu f_{B_s}(C_{10} - C_{10}')\bar{\ell}\gamma_\mu\gamma_5\ell + \frac{i}{2} f_{B_s} \frac{M_{B_s}^2}{m_b + m_s}(C_S m_b - C_S' m_s)\bar{\ell}\ell \\
&\quad + \frac{i}{2} f_{B_s} \frac{M_{B_s}^2}{m_b + m_s}(C_P m_b - C_P' m_s)\bar{\ell}\gamma_5\ell \Bigg] \\
&= \frac{G_F\alpha}{\sqrt{2}\pi} V_{tb}V_{ts}^* \Bigg[F_A p^\mu \bar{\ell}\gamma_\mu\gamma_5\ell + F_S\bar{\ell}\ell + F_P\bar{\ell}\gamma_5\ell \Bigg].
\end{aligned}
\tag{63}
$$

Here, $\alpha = \frac{e^2}{4\pi}$ is the electromagnetic fine-structure constant and the F_i's represent the scalar (S), pseudo-scalar (P) and axial-vector (A) contributions to the matrix element. They are given by

$$
\begin{aligned}
F_A &= \frac{-i}{2} f_{B_s}(C_{10} - C_{10}'), \\
F_S &= \frac{-i}{2} f_{B_s} M_{B_s}^2 \left(\frac{C_S m_b - C_S' m_s}{m_b + m_s} \right), \\
F_P &= \frac{-i}{2} f_{B_s} M_{B_s}^2 \left(\frac{C_P m_b - C_P' m_s}{m_b + m_s} \right).
\end{aligned}
\tag{64}
$$

By squaring the matrix element and summing over the lepton spins we find the following expression[10]

$$
\begin{aligned}
|\mathcal{M}|^2 &= \frac{G_F^2\alpha^2}{\pi^2}|V_{tb}V_{ts}^*|^2 \Bigg[(M_{B_s}^2 - 4m_\ell^2)|F_S|^2 + M_{B_s}^2|F_P|^2 + 4m_\ell^2 M_{B_s}^2|F_A|^2 + 2m_\ell M_{B_s}^2(F_A F_P^* + F_P F_A^*) \Bigg] \\
&= \frac{G_F^2\alpha^2 M_{B_s}^2}{\pi^2}|V_{tb}V_{ts}^*|^2 \left[\left(1 - \frac{4m_\ell^2}{M_{B_s}^2}\right)|F_S|^2 + |F_P + 2m_\ell F_A|^2 \right].
\end{aligned}
\tag{65}
$$

Here, m_ℓ is the lepton mass and we have used $M_{B_s}^2 = (q_{\ell_+} + q_{\ell_-})^2 = p^2$, where $q_{\ell_\pm}$ are the momenta of the final state leptons. We will use the expression derived for $|\mathcal{M}|^2$ as a starting point for the BR calculation.

To calculate the BR we start off from the general formula for the differential decay width for a process ending in a two-body final state, which is given by[35]

$$
d\Gamma(A \to BC) = \frac{1}{2M_A}|\mathcal{M}|^2 dV(P_A; q_B, q_C)d\Omega,
\tag{66}
$$

where M_A is the mass of the decaying particle, P_A its momentum and q_B and q_C are the momenta of the final state particles. The two-body phase space integration element ($dV(P_A; q_B, q_C)$), which is evaluated in the rest frame of the decaying particle, is defined as

$$
dV(P_A; q_B, q_C) = \frac{1}{32\pi^2}\lambda(1, m_B^2/M_A^2, m_C^2/M_A^2)^{1/2}d\Omega,
\tag{67}
$$

where $\lambda(1, m_B^2/M_A^2, m_C^2/M_A^2)$ is the Källén function and M_A, m_B and m_C are the masses of the involved particles. If we apply this to the process $\bar{B}_s^0 \to \ell^+\ell^-$ we arrive at the following differential decay width

---

[10] For a detailed description of how this calculation is performed, the reader is referred to ref. [35]

$$dΓ(\bar{B}_s^0 → ℓ^+ℓ^-) = \frac{1}{2M_{B_s}}|\mathcal{M}|^2\frac{1}{32π^2}λ(1, \frac{m_ℓ^2}{M_{B_s}^2}, \frac{m_ℓ^2}{M_{B_s}^2})^{1/2}dΩ$$
$$= \frac{|\mathcal{M}|^2}{64π^2 M_{B_s}}\sqrt{1 - \frac{4m_ℓ^2}{M_{B_s}^2}}dΩ. \tag{68}$$

Integrating both sides and using $\int dΩ = 4π$ gives

$$Γ(\bar{B}_s^0 → ℓ^+ℓ^-) = \frac{|\mathcal{M}|^2}{16π M_{B_s}}\sqrt{1 - \frac{4m_ℓ^2}{M_{B_s}^2}}, \tag{69}$$

which is the partial decay width for $\bar{B}_s^0 → ℓ^+ℓ^-$. The BR of $\bar{B}_s^0 → ℓ^+ℓ^-$ is defined as the partial decay width divided by the total decay width of the $\bar{B}_s^0$ meson

$$\text{BR}(\bar{B}_s^0 → ℓ^+ℓ^-) = \frac{Γ(\bar{B}_s^0 → ℓ^+ℓ^-)}{Γ_{\text{total}}} = τ_{B_s}Γ(\bar{B}_s^0 → ℓ^+ℓ^-). \tag{70}$$

Here, we have used that $Γ_{\text{total}} = 1/τ_{B_s}$. Upon insertion of our result for the decay width from equation 69 we find

$$\text{BR}(\bar{B}_s^0 → ℓ^+ℓ^-) = \frac{|\mathcal{M}|^2 τ_{B_s}}{16π M_{B_s}}\sqrt{1 - \frac{4m_ℓ^2}{M_{B_s}^2}}. \tag{71}$$

And finally by substituting our expression for $|\mathcal{M}|^2$ from equation 65 we arrive at

$$\text{BR}(\bar{B}_s^0 → ℓ^+ℓ^-) = \frac{G_F^2 α^2 M_{B_s} τ_{B_s}}{16π^3}|V_{tb}V_{ts}^*|^2\sqrt{1 - \frac{4m_ℓ^2}{M_{B_s}^2}}\left[\left(1 - \frac{4m_ℓ^2}{M_{B_s}^2}\right)|F_S|^2 + |F_P + 2m_ℓ F_A|^2\right]. \tag{72}$$

Sometimes, instead of the above defined $C_S^{(')}$ and $C_P^{(')}$, the coefficients C_{Q_1} and C_{Q_2} are used. These relate to $C_{S,P}^{(')}$ in the following way

$$C_{S,P}m_b = C_{Q_1,Q_2} \qquad C_{S,P}'m_s = C_{Q_1,Q_2}' \tag{73}$$

By making use of these equations we can write the BR as

$$\text{BR}(\bar{B}_s^0 → ℓ^+ℓ^-) = \frac{G_F^2 α^2 τ_{B_s} M_{B_s}^3 f_{B_s}^2}{64π^3}|V_{tb}V_{ts}^*|^2\sqrt{1 - \frac{4m_ℓ^2}{M_{B_s}^2}}$$
$$× \left[\left(1 - \frac{4m_ℓ^2}{M_{B_s}^2}\right)\left|\left(\frac{M_{B_s}}{m_b + m_s}\right)(C_{Q_1} - C_{Q_1}')\right|^2 + \left|\frac{M_{B_s}}{m_b + m_s}(C_{Q_2} - C_{Q_2}') + \frac{2m_ℓ}{M_{B_s}}(C_{10} - C_{10}')\right|^2\right]. \tag{74}$$

If we want to make the step to a BR for the specific process to a muon-anti-muon final state we have to substitute the lepton mass $m_ℓ$ for the muon mass $m_μ$.

Wilson coefficients

So far, we have used Wilson coefficients in the BR equations without specifying their forms. As explained before, expressions for the Wilson coefficients are found by matching the full theory to the EFT. The result for the coefficients depends on the nature of the full theory. For instance, if the full theory is the SM, fewer particles are integrated out and incorporated in the Wilson coefficients than when SUSY is the full theory. Since we consider the process $\bar{B}_s^0 → ℓ^+ℓ^-$ in the pMSSM, the pMSSM defines our full theory. By starting at high energy, integrating out all heavy particles up to the W boson and performing the matching we can find the right Wilson coefficients. Since the full expressions for the Wilson coefficients are complex, we do not list them here but refer to ref.[15]. This provides an overview of the Wilson coefficients $C_{10}^{(')}$, $C_{Q1}^{(')}$ and $C_{Q2}^{(')}$ within the SM and pMSSM up to next-to-next-to-lowest order (NNLO).

Although the full expressions for the Wilson coefficients are complex, we can approximate their largest contributions in the limit of large $\tan\beta$. In the pMSSM, for large values of $\tan\beta$, we can assume that $C_{Q_1} \approx -C_{Q_2}$. In this limit, the largest contribution to C_{Q_2} is given by[39]

$$C_{Q_2} \approx \mu A_t \frac{\tan^3\beta}{(1+\epsilon\tan\beta)^2} \frac{m_t^2}{m_{\tilde{t}}^2} \frac{m_b m_\mu}{4\sin^2\theta_W M_W^2 m_A^2} f(x_{\tilde{t}\mu}). \tag{75}$$

Here $m_{\tilde{t}}^2 = m_{\tilde{t}_1} m_{\tilde{t}_2}$, and $x_{\tilde{t}\mu} = \frac{m_{\tilde{t}}^2}{\mu^2}$. The parameter ϵ parametrizes loop-induced non-holomorphic terms that receive their dominant contributions from higgsino and gluino exchange[2]. The function $f(x)$ is defined as

$$f(x) = -\frac{x}{1-x} - \frac{x}{(1-x)^2}\ln x, \tag{76}$$

Which is always positive, meaning that for large $\tan\beta$, the sign of C_{Q_2}, and therefore that of C_{Q_1}, depends on the sign of the combination μA_t.

From the expressions for the Wilson coefficients we can derive which pMSSM parameters will significantly influence the BR. We will do this in chapter 6, and use this, together with our analysis of the dominant Feynman diagrams, to analyze the behavior of the BR in the pMSSM.

SM contributions to the BR
The above derived BR equations hold for the process $\bar{B}_s^0 \to \ell^+\ell^-$ in general. Focusing on the muon–anti-muon final state, we can derive $\mathrm{BR}(\bar{B}_s^0 \to \mu^+\mu^-)$ in the SM by turning off all SUSY contributions. In the SM, only the C_{10} Wilson coefficient gives a non-zero contribution[34]. Therefore, we can obtain the SM result by setting all other Wilson coefficients to zero. If we do this for the BR in equation 74, we arrive at

$$\mathrm{BR}(\bar{B}_s^0 \to \mu^+\mu^-)_{\mathrm{SM}} = \frac{G_F^2 \alpha^2 M_{B_s} f_{B_s}^2 \tau_{B_s} m_\mu^2}{16\pi^3} |V_{tb}V_{ts}^*|^2 \sqrt{1 - \frac{4m_\mu^2}{M_{B_s}^2}} |C_{10}|^2, \tag{77}$$

which is the SM BR equation for the process $\bar{B}_s^0 \to \mu^+\mu^-$. The value of the Wilson coefficient C_{10} in the SM is given by $C_{10} = 4.134$[33].

BR predictions and measurements
The decay $B_s^0 \to \mu^+\mu^-$ was first observed in 2015 by the CMS and LHCb collaborations which performed a combined analysis of LHC data[1]. The latest measurement of the BR by the LHCb collaboration gave the following result[31]:

$$\bar{\mathcal{B}}(B_s \to \mu^+\mu^-)_{\mathrm{LHCb'17}} = (3.0 \pm 0.6^{+0.3}_{-0.2}) \times 10^{-9}. \tag{78}$$

Here the first presented uncertainty is statistical and the second one is systematic. This value concerns the untagged, time-integerated BR. A calculated SM prediction yields the following value for the untagged, time-integrated BR[34]:

$$\bar{\mathcal{B}}(B_s \to \mu^+\mu^-)_{\mathrm{SM}} = (3.57 \pm 0.16) \times 10^{-9}. \tag{79}$$

The SM prediction is consistent with the experimental results within the uncertainties. This consistency does not point at contributions of new physics to the BR and puts constraints on the pMSSM parameters. However, as stated before, new physics could also reside in other aspects of the process and does not necessarily have to alter the BR.

3.5 Summary

In this chapter we have provided an overview of the relevant aspects of the process $B_s^0 \to \mu^+\mu^-$. First we gave an introduction to the B_s^0 meson and the process $B_s^0 \to \mu^+\mu^-$, followed by a description of B_s^0-$\bar{B}_s^0$ mixing. Furthermore, we explained the differences between the different types of BRs that we encounter in literature. An important observation is that we measure the time-integrated and untagged BR in experiments. Next, we gave an overview of the dominant Feynman diagrams contributing to $B_s^0 \to \mu^+\mu^-$ within the SM and pMSSM. Based on these diagrams we determined which pMSSM parameters are expected to influence the BR in a significant way. Although this is only a first approximation, we will use this result as a starting point for our analysis of the BR behavior in chapter 6.1. In the final part

of the chapter we derived the BR for $\bar{B}_s^0 \to \mu^+\mu^-$ by means of an EFT approach. We introduced the concept of EFTs and provided a step by step derivation. Our main results (equations 72 and 74) will be used to analyze BR calculations performed by different computational programs. These programs will be introduced in chapter 4. In addition, we derived an equation for the SM BR (equation 77). This result will be used in chapter 5 to compare SM calculations performed by the computational programs.

4 Computational tools

This chapter gives a description of the computational programs that are used to generate particle spectra and to calculate the BR of the process $B_s \to \mu^+\mu^-$. It introduces each program and explains the way in which it calculates the BR. The two programs we will focus on are considered in more detail. Their differences are discussed and the relevant characteristics of both programs are summarized in a table.

The computational tools that are used to investigate the process $B_s \to \mu^+\mu^-$ are Spheno (SP)[43], MicrOMEGAs (MO)[18][19] and SuperIso (SI)[15]. SP can be used both as a spectrum generator and to calculate the BR, whereas MO and SI are only able to calculate the BR. To perform this calculation both programs require a spectrum as an input. For our analysis, we will use the spectra generated by SP as an input for MO and SI. In the following sections, each program is introduced and the procedures used for the BR calculation are discussed. Due to the complexity of the SP code, we will mainly focus on the BR calculation performed by MO and SI. The important features of MO and SI are summarized in table 9 and a discussion on the differences between the two programs is provided.

4.1 SPheno

SP is a program that calculates the particle spectrum of a supersymmetric BSM theory, such as the pMSSM. The obtained masses and mixing matrices can be used for the calculation of $\mathrm{BR}(B_s \to \mu^+\mu^-)$. SP uses an SLHA (SUSY Les Houches Accord) file[30] as input. In the case of the pMSSM, this input file should, next to a set of SM input and program settings, contain the 19 pMSSM parameters. An example of an input file used to perform the spectrum calculations is given in appendix B. SP produces an output file containing the particle spectrum. This SLHA file includes masses and mixing matrices and can directly be used as an input for MO and SI.

SP calculates the untagged, theoretical BR of $B_s \to \mu^+\mu^-$ (equation 74). The calculation is based on ref. [9]. In this paper, the Wilson coefficients are derived based on the contributions of the dominant LO diagrams, which were introduced in section 3.3. The calculation includes the one-loop QCD corrections to these diagrams and is performed using running couplings and running SUSY masses. Since the program uses these running couplings and masses, the BR calculation is more complex than the calculations performed by MO and SI.

4.2 MicrOMEGAs

MO is a computational tool that is designed to calculate various properties of dark matter. Besides this main purpose, it is also able to perform decay width and BR calculations, such as that of $B_s \to \mu^+\mu^-$. As an input, the program uses an SLHA file containing an externally calculated particle spectrum.

MO calculates the untagged, theoretical BR of $B_s \to \mu^+\mu^-$. The calculation uses equation 72 as a starting point and is based on ref. [10]. MO only takes the main NLO $\tan\beta$ contributions into account. This means that next to the LO diagrams, only the one-loop correction diagrams with the highest orders in $\tan\beta$ play a role. Concerning the Wilson coefficients, MO only considers the SM contributions to C_{10}, and all primed Wilson coefficients are neglected. For C'_{10} this is because its contribution is very small and for $C'_{S,P}$ because they are suppressed by a factor m_s/m_b compared to $C_{S,P}$. The full expressions for the Wilson coefficients used by MO are given in ref. [10]. To perform the calculation, the relation $C_S = -C_P$ is used. This is a valid assumption for large $\tan\beta$ [2]. Unfortunately, it is unclear at which scale the Wilson coefficients are evaluated.

The code relevant for the calculation of the BR can be found in the MSSM folder in the file `bsmu.c`. Instead of using the expression in equation 72, the code combines some of the variables in one number and puts this in front of the equation. The value of this one number, which we will call the 'pre-factor' is $7.827 \cdot 10^{-10}$. Unfortunately, the program does not provide an expression for the calculation of this pre-factor. The BR equation used in the code is given by

$$\text{BR}(B_s \to \mu^+\mu^-) = 7.827 \cdot 10^{-10} \sqrt{1 - \frac{4m_\mu^2}{M_{B_s}^2}} \left[\frac{\left(1 - \frac{4m_\mu^2}{M_{B_s}^2}\right) C_{S_{SUSY}}^2 M_{B_s}^4}{16 M_W^4} + \left(\frac{M_{B_s}^2 C_{P_{SUSY}}}{4 M_W^2} - 2Y(x_t) \right)^2 \right].$$

(80)

Here $C_{S_{SUSY}}$ and $C_{P_{SUSY}}$ contain the $C_{S,P}$ Wilson coefficient contributions, and $Y(x_t)$ contains the C_{10} contributions. The C_{10} Wilson coefficient is calculated by the following numerical approximation, which gives the SM contributions up to NLO

$$C_{10} = -\frac{Y(x_t)}{\sin^2 \theta_W},$$

$$Y(x_t) = 0.997 \cdot \frac{m_t(m_t)}{166 \text{ GeV}}^{1.56}.$$

(81)

Here θ_W is the weak mixing angle, $m_t(m_t)$ is the top mass evaluated in the $\overline{\text{MS}}$ scheme at $\mu = m_t$[14], and $x_t = m_t^2(m_t)/M_W^2$. The $C_{S,P}$ Wilson coefficients are calculated by adding separate contributions from box diagrams, Higgs penguin diagrams, EW penguin diagrams and charged Higgs diagrams.

As can be seen, equation 80 differs from equation 72, which is the formula provided by the paper the code is based on (ref. [10]). By comparing the two equations, we tried to reconstruct an expression for the pre-factor. Based on this comparison we derived that the pre-factor should be proportional to

$$\propto \frac{G_F^2 \alpha^2 M_{B_s} \tau_{B_s} f_{B_s}^2 |V_{tb} V_{ts}^*|^2 m_\mu^2}{64 \pi^3 \sin^2 \theta_W}.$$

(82)

After inserting typical values (see appendix C, table 12) for the variables in equation 82, we arrived at a pre-factor of the same order as the value provided by the program. Unfortunately, we were not able to retrieve the exact value. It therefore remains unclear which input values were used to arrive at this number[11]. This makes it more complicated to compare the calculation to calculations performed by other programs.

Table 7 gives an overview of the variables relevant for the BR calculation performed by MO and SI (based on equations 72 and 74). For each variable it is indicated if it is read out from the input SLHA file, hard-coded or incorporated in the pre-factor. For the hard-coded variables, the table presents the corresponding values. For the variables that are read out from the input file, a typical value is provided.

4.3 SuperIso

SI is a program that can be used for the calculation of flavour physics observables in the MSSM, such as the BR of the decay $B_s \to \mu^+\mu^-$. The program is also able to perform calculations within the SM. For the SM calculation, the program requires no input, but uses hard-coded values. A list of these hard-coded values, which are similar to the typical values presented in table 7, is provided in table 8. Apart from the built-in models, it is also possible to perform calculations based on an external SLHA input file containing a particle spectrum. In this case, SI uses the input file values instead of the hard-coded values to perform calculations.

SI calculates the untagged theoretical BR of $B_s \to \mu^+\mu^-$. This calculation proceeds via the use of equation 74, and it is partly based on the same paper as SP[9]. The program also calculates the untagged time-integrated BR by means of the conversion formula given in equation 55. To calculate the Wilson coefficients, SI includes two-loop EW (NNLO contributions) and three-loop QCD corrections (next-to NNLO, i.e. NNNLO contributions). The three-loop QCD contributions are only used for the calculation of C_{10}. The coefficients $C_{Q1,Q2}$ are calculated including two-loop QCD corrections. The program evaluates the Wilson coefficients at a matching scale μ_W and then evolves them to a scale μ_b. As explained in section 3.4.1, as a rule of thumb, these scales are usually chosen between $0.5 M_W - 2 M_W$ and $0.5 m_b - 2 m_b$.

---

[11]After several attempts to arrive at the specified number we reached out to the creators of the MicrOMEGAs code for clarification. However, this did not result in a clearer picture of how the pre-factor is calculated.

	SuperIso		MicrOMEGAs	
Variable	**Origin**	**Value**	**Origin**	**Value**
G_F	input file	$1.16637 \cdot 10^{-5}$ GeV^{-2}	pre-factor	-
$\alpha^{-1}(M_Z)$	input file	1.279	pre-factor	-
M_{B_s}	hard-coded	5.36677 GeV	hard-coded	5.369 GeV
f_{B_s}	hard-coded	0.2277 GeV	pre-factor	-
τ_{B_s}	hard-coded	$1.51 \cdot 10^{-12}$ s	pre-factor	-
$m_{\mu_{\mathrm{pole}}}$	input file	0.106 GeV	hard-coded	0.1059 GeV
V_{tb}	hard-coded	0.999	pre-factor	-
V_{ts}	hard-coded	0.0403	pre-factor	-
M_W	input file	80.3 GeV	hard-coded	80.2 GeV
$M_{Z_{\mathrm{pole}}}$	input file	91.2 GeV	input file	91.2 GeV
$m_{t_{\mathrm{pole}}}$	input file	173.1 GeV	input file	173.1 GeV
$m_b(m_b)$	input file	4.18 GeV	input file	4.18 GeV
$\alpha_s(M_Z)$	input file	0.1187	input file	0.1187
$\sin^2\theta_W$	calculated	$\sin^2\theta_W = \sin^2(\arctan(g_1/g_2))$	calculated	$\sin^2\theta_W = 1 - (M_W/M_Z)^2$
g_1	hard-coded	0.357458	not present	-
g_2	hard-coded	0.651908	not present	-

Table 7: Overview of the variables relevant for the BR calculation performed by SI and MO. The table specifies the origin of each variable (input file, hard-coded or pre-factor). In case of a hard-coded variable, its value is presented and for the input file variables, a typical value is provided. If a variable is not present in one of the codes, this is also indicated. The bottom mass $m_b(m_b)$ and couplings $\alpha^{-1}(M_Z)$ and $\alpha_s(M_Z)$ are evaluated in the $\overline{\mathrm{MS}}$ scheme[12].

Variable	**Value**	**Variable**	**Value**
G_F	$1.16647 \cdot 10^{-5}$ GeV^{-2}	$M_{Z_{\mathrm{pole}}}$	91.1876 GeV
$\alpha^{-1}(M_Z)$	$1.27917 \cdot 10^{-2}$	$m_{t_{\mathrm{pole}}}$	173.34 GeV
$m_{\mu_{\mathrm{pole}}}$	0.105658 GeV	$m_b(m_b)$	4.18 GeV
M_W	80.385 GeV	$\alpha_s(M_Z)$	0.1181

Table 8: Overview of the hard-coded values that are used by SI to perform SM calculations. These values are an addition to the hard-coded values presented in table 7.

The contributions to the Wilson coefficients at different orders are calculated separately and added by means of the following perturbative expansion

$$C_i(\mu) = C_i^{(0)}(\mu) + \frac{\alpha_s(\mu)}{4\pi}C_{i,s}^{(1)}(\mu) + \left(\frac{\alpha_s(\mu)}{4\pi}\right)^2 C_{i,s}^{(2)}(\mu) + \frac{\alpha(\mu)}{4\pi}C_{i,e}^{(1)}(\mu) + \frac{\alpha(\mu)}{4\pi}\frac{\alpha_s(\mu)}{4\pi}C_{i,es}^{(2)}(\mu) + \cdots , \quad (83)$$

where $C_{i,j}^{(k)}$ is the Wilson coefficient at order k in the perturbative expansion in $\alpha(\mu)$ ($j = e$) or $\alpha_s(\mu)$ ($j = s$). The expressions for the Wilson coefficients can be found in the SI manual[15]. In contrast to MO, SI also includes SUSY contributions for the calculation of C_{10}. For the calculation of $C_{Q1,Q2}$, the relation $C_{Q1} = -C_{Q2}$ is used, which is, similar to the relation for $C_{S,P}$ a valid assumption for large $\tan\beta$.

The code used for the calculation of the BR can be found in `bsmumu.c`, and the code used to evaluate the Wilson coefficients in `wilson.c`. An overview of which values are retrieved from the input file and which are hardcoded is given in table 7. Similar to MO, the Wilson coefficients are constructed from separate

---

[12]For a description of the $\overline{\mathrm{MS}}$ scheme see ref. [16].

contributions, belonging to different types of diagrams. SI makes a distinction between SM contributions, chargino contributions and Higgs contributions. The scales $\mu_{W,b}$ can be adjusted in the code. For the external SLHA option, they are by default set at $\mu_W = M_W$ and $\mu_b = m_{b_{\text{pole}}}$. However, for the SM option they are set at $\mu_W = 2M_W$ and $\mu_b = 0.5m_{b_{\text{pole}}}$. Since the scales are used to evaluate the Wilson coefficients, different values of these scales lead to different BR values for the same input. Though both sets of values are reasonable, it is important to note that different default settings are used for different models. This means that calculations performed for different models cannot be compared to each other without changing the scale settings. Unfortunately, the program documentation gives no explanation for using different default sets of scales.

4.4   Comparison between MicrOMEGAs and SuperIso

An overview of the important characteristics of MO and SI concerning the calculation of BR($B_s \to \mu^+\mu^-$) is given in table 9. There are a few notable differences between the programs. First, both programs use different values for the input variables used for the BR calculation. These variables and their values are listed in table 7. Next to this, the two programs compute contributions to the Wilson coefficients at different orders. MO only takes the main $\tan\beta$ NLO contributions into account, whereas SI includes two-loop EW and three-loop QCD corrections (the three-loop QCD corrections are only used for the calculation of C_{10}). Moreover, MO neglects the primed Wilson coefficients and only includes SM contributions to C_{10}. SI however, takes also the primed Wilson coefficients into account and includes SUSY contributions to C_{10}. Therefore, SI provides a more accurate calculation. Furthermore, there is some ambiguity considering the pre-factor used by MO. The last important thing to note is that the documentation of both programs is unclear about the scales at which the Wilson coefficients are evaluated. For SI, the scales can be found in the code, however for MO we were not able to retrieve the choice of scales from the code.

	MicrOMEGAs	SuperIso
BR equation	equation 72	equation 74
Type(s) of BR	untagged theoretical (equation 54)	untagged theoretical (equation 54) untagged time-integrated (equation 52)
Order of calculation	main $\tan\beta$ NLO contributions	two-loop EW corrections (NNLO) three-loop QCD corrections (NNNLO)
Notes	– Uses an unspecified pre-factor to perform BR calculation. – Primed Wilson coefficients are neglected. – C_{10} is calculated by means of a numerical approximation and only includes SM contributions. – Evaluation scales of Wilson coefficients are unspecified.	– Contains an option to perform SM calculations. – Default evaluation scales of Wilson coefficients differ per model, but can be adjusted. – The three-loop QCD corrections are only used for the calculation of C_{10}.

Table 9: Overview of the important features of MO and SI concerning the calculation of BR($B_s \to \mu^+\mu^-$).

The differences between the two programs result in deviations between the calculated BR values. In the next chapters, we will investigate these deviations by means of a numerical analysis. We start by comparing SM calculations and subsequently extend this comparison to the pMSSM. Furthermore, we will examine the influence of the individual pMSSM parameters on the BR. This will add to our knowledge about which parameters are of importance for the BR calculation and provides us with insight into the behavior of the BR in specific parts of the parameter space. Lastly, we will combine the results of our analyses and argue which program could be used best to perform the calculation of BR($B_s \to \mu^+\mu^-$).

5 Comparing Standard Model branching ratio calculations

This chapter describes the comparison of the BR calculation by MO and SI within the SM. Firstly, we explain how the SM value is obtained, followed by an analysis of the SM calculations performed by both programs. For SI, the SM calculation is executed for multiple combinations of scales.

We start by comparing the theoretical SM BRs calculated by MO and SI, to find out whether the basis of the two codes is the same. Both programs are designed to perform calculations in a supersymmetric BSM setting, such as the pMSSM. To compare SM calculations we have two options. Firstly, we can adjust our input[13] in such a way that the calculation is performed in the decoupling limit. This is done by choosing $m_A \gg M_Z$ (as explained in section 2.2.1), and results in a decoupling of the SUSY heavy Higgs contributions. If we combine this with small values for the parameters that are related to the dominant pMSSM diagrams (see section 3.3), such as $\tan\beta$, A_t and μ, we minimize the SUSY contributions and the calculation will approach the SM BR. However, since we take a limit, this does not result in the exact SM value for the BR. To achieve this, we can use a second option: turning off all SUSY contributions in the code. If we keep the SM input parameters constant, this will provide us with the same SM result for every input set, regardless of the chosen pMSSM input parameters. The SM input values used for the calculations performed in this chapter can be found in appendix C in table 13.

For MO, it is possible to turn off all SUSY contributions by setting all Wilson coefficients to zero except for C_{10}. Unfortunately, for SI we are not able to switch off all SUSY contributions. This is because in the SI code, C_{10} also receives SUSY contributions. Setting these contributions to zero turns out to be complicated, due to the complexity of the code. Therefore, for SI, we choose to use the decoupling limit approach in combination with a small value for $\tan\beta$ to perform the SM calculation. We choose to only require a small value for $\tan\beta$, because (as will be discussed in section 6.1) this is the only parameter that has a significant influence on the BR in the decoupling limit. Since the calculation does not result in an exact SM value, we average over the results of 1000 decoupling limit calculations of the theoretical BR. For every input set, we choose $m_A = 15$ TeV and $\tan\beta$ between 2 and 5. The other parameters are chosen randomly for each set, but within the ranges listed in table 14.

As explained in chapter 4, we do not know which scales are used by MO to perform the calculation. For SI, the scales at which the calculations are performed (μ_W and μ_b) can be adjusted in the code. As mentioned in section 3.4.1, they are usually chosen to be between $0.5M_W$ - $2M_W$ and $0.5m_b$ - $2m_b$. In order to provide a good comparison between the two programs, we perform the SI calculation for $\mu_W \in \{0.5M_W, M_W, 2M_W\}$ and $\mu_b \in \{0.5m_b, m_b, 2m_b\}$, where m_b is the pole mass of the bottom quark. We then have 9 different combinations for the scale values of μ_W and μ_b. For each of these scale combinations we use the same 1000 input sets to calculate the average decoupling limit BR.

The result of the SM theoretical BR calculation by MO is $3.06 \cdot 10^{-9}$. The average SI theoretical BR varies, depending on the chosen scale combination, between $3.05 \cdot 10^{-9}$ and $3.24 \cdot 10^{-9}$. The SM-only BR calculated by MO thus lies within the bandwidth of the decoupling limit BR calculation performed by SI. Next to this, in case of equal scales and SM input, the SI decoupling limit calculation is in agreement with the built-in SM-only calculation. As a final remark we want to note that the scale choice has by far the biggest impact on the calculated theoretical SM value for $\mathrm{BR}(B_s^0 \to \mu^+\mu^-)$. Changing the hard-coded input parameters of both calculations turned out to be less important.

---

[13]Keep in mind that, as explained in chapter 4, this input is first provided to SP. This program calculates a mass spectrum that is used as an input for SI and MO. If we mention 'input' we refer to the input provided to SP.

6 Comparing branching ratio calculations in the pMSSM

This chapter describes the comparison of BR calculations performed by MO and SI within the pMSSM. Firstly, a single parameter variation is performed, followed by BR calculations for a random scan in the pMSSM parameter space. Lastly, the influence of choice of scale in SI is studied.

After having studied the BR calculations executed by MO and SI in the SM in chapter 5, we will now focus on calculations performed in the pMSSM. We will study the behavior of the BR as a result of different pMSSM input parameters and aim to find out what the differences are between SI and MO. Firstly, we will examine the influence of individual parameters on the BR by means of a single parameter variation. Secondly, we will study the BRs which are a result of a random pMSSM scan. Our analysis of the BR behavior within the SM already showed that the choice of scales in SI influences the calculation. We will therefore extend this analysis to the pMSSM. The calculations will be performed using the same SM input values as in the chapter 5 (table 13).

6.1 Variation of single parameters

To get a first impression of the effects of the 19 pMSSM parameters on the BR, we perform an analysis in which we vary each parameter separately. While doing this, we keep the other parameters at a constant value. This gives us a first impression of the behavior of the BR and the influence of the pMSSM input parameters, which we can compare to our theoretical prediction in section 3.3.1. However, it should be pointed out that, since we make use of specific input set in which we only vary 1 out of 19 parameters, this analysis will not give us a full picture of the BR behavior within the pMSSM.

Based on our analysis of the dominant Feynman diagrams in section 3.3, we argued that the parameters $\tan\beta$, m_A, A_t, μ, M_2 and the squark masses ($m_{\tilde{Q}_1}$, $m_{\tilde{Q}_3}$, $m_{\tilde{u}_R}$, $m_{\tilde{t}_R}$) might influence the BR. If we have a look at the equations for the Wilson coefficients provided in ref. [15], we see that $\tan^2\beta$ and m_A^{-2} appear as a pre-factor. Therefore, we expect the influence of $\tan\beta$ and m_A to be large. The other parameters (A_t, μ, M_2, $m_{\tilde{Q}_1}$, $m_{\tilde{Q}_3}$, $m_{\tilde{u}_R}$ and $m_{\tilde{t}_R}$) are less apparent in the equations, and mainly enter via mixing matrices. Basd on these equations, it is therefore hard to predict their precise influence on the BR. If we consider the large $\tan\beta$ limit, the contributions to the unprimed Wilson coefficients can be approximated by equation 75. This equation contains the factors μA_t, $\tan^3\beta$ and $m_{\tilde{t}_1}m_{\tilde{t}_2}$. Therefore, in case of a large $\tan\beta$, we also expect the influence of A_t, μ, $m_{\tilde{Q}_3}$ and $m_{\tilde{t}_R}$ to be large. Besides the parameters we derived from the Feynman diagrams, the equations for the Wilson coefficients contain the gluino mass parameter (M_3). Consequently, we expect this parameter to influence the BR as well.

Three sets of pMSSM input parameters are selected to perform the single parameter variation. All three are chosen such that they result in a Higgs mass between 122 and 128 GeV and a neutralino as the LSP. The sets of input parameters (including the by SP calculated value for M_{SUSY}) are listed in table 10 and the corresponding BRs in table 11. The mass spectra can be found in table 15 in appendix C. The important characteristics of set 1 are that $\tan\beta$ is around 10 and that the other parameters are chosen to be around 1 TeV. For set 2, $\tan\beta$ is larger ($\sim$35) and the other parameters (except for m_A, which is 990 GeV) are chosen to be several TeVs. For set 3, m_A is around 5 TeV, therefore calculations performed with this set are in the decoupling limit.

For all sets, we vary each parameter over the range specified in table 14 in appendix C. For every value, the mass spectrum is calculated by SP, followed by the calculation of the theoretical BR by SI and MO. The SM input parameters are also kept constant and can be found in table 13 in appendix B. During the variation, the requirements concerning the Higgs mass and LSP are not checked for again. We perform the variation for 2000 different values in the indicated range and do this for all 19 pMSSM parameters. The scale combination used by SI is $\mu_W = M_W$, $\mu_b = m_b$, which is the default setting for the external SLHA option.

The next subsections give an overview of the results of the single parameter variation for set 1,2 and 3. For all sets, only the figures of the parameters that affect the BR are displayed. The parameters that show small or no influence are left out. Although for all three sets the parameters are varied over the same range, sometimes only part of this range is shown. This is because for parameter values outside this range, no viable spectra could be calculated.

Parameter	Value	Parameter	Value	Parameter	Value
M_1	1369 GeV	M_1	6954 GeV	M_1	4419 GeV
M_2	1751 GeV	M_2	-1003 GeV	M_2	2706 GeV
M_3	1878 GeV	M_3	5367 GeV	M_3	4415 GeV
μ	-49.65 GeV	μ	2723 GeV	μ	-1268 GeV
$\tan\beta$	9.871	$\tan\beta$	35.48	$\tan\beta$	25.50
m_A	308.2 GeV	m_A	990 GeV	m_A	5394 GeV
A_t	2169 GeV	A_t	-6528 GeV	A_t	3882 GeV
A_b	3262 GeV	A_b	7413 GeV	A_b	-3644 GeV
A_τ	324.1 GeV	A_τ	2391 GeV	A_τ	-5451 GeV
$m_{\tilde{Q}_1}$	1694 GeV	$m_{\tilde{Q}_1}$	2562 GeV	$m_{\tilde{Q}_1}$	5216 GeV
$m_{\tilde{u}_R}$	554.6 GeV	$m_{\tilde{u}_R}$	4455 GeV	$m_{\tilde{u}_R}$	2211 GeV
$m_{\tilde{d}_R}$	577.2 GeV	$m_{\tilde{d}_R}$	1800 GeV	$m_{\tilde{d}_R}$	5332 GeV
$m_{\tilde{Q}_3}$	1260 GeV	$m_{\tilde{Q}_3}$	5051 GeV	$m_{\tilde{Q}_3}$	3797 GeV
$m_{\tilde{t}_R}$	854.4 GeV	$m_{\tilde{t}_R}$	6672 GeV	$m_{\tilde{t}_R}$	3529 GeV
$m_{\tilde{b}_R}$	1098 GeV	$m_{\tilde{b}_R}$	6105 GeV	$m_{\tilde{b}_R}$	1876 GeV
$m_{\tilde{L}_1}$	1750 GeV	$m_{\tilde{L}_1}$	3559 GeV	$m_{\tilde{L}_1}$	2420 GeV
$m_{\tilde{e}_R}$	1653 GeV	$m_{\tilde{e}_R}$	2497 GeV	$m_{\tilde{e}_R}$	3319 GeV
$m_{\tilde{L}_3}$	1351 GeV	$m_{\tilde{L}_3}$	2743 GeV	$m_{\tilde{L}_3}$	1402 GeV
$m_{\tilde{\tau}_R}$	919.6 GeV	$m_{\tilde{\tau}_R}$	2000 GeV	$m_{\tilde{\tau}_R}$	3758 GeV
M_{SUSY}	1052 GeV	M_{SUSY}	5808 GeV	M_{SUSY}	3664 GeV
(a) Set 1		(b) Set 2		(c) Set 3	

Table 10: Input sets for the single parameter variation. The value of M_{SUSY}, calculated by SP, is also included.

	Theoretical BR		
Program	Set 1	Set 2	Set 3
SuperIso	$3.14 \cdot 10^{-9}$	$4.32 \cdot 10^{-9}$	$3.11 \cdot 10^{-9}$
MicrOMEGAs	$2.99 \cdot 10^{-9}$	$4.42 \cdot 10^{-9}$	$3.06 \cdot 10^{-9}$

Table 11: Theoretical BRs calculated by SI and MO for the input parameters of set 1,2 and 3.

6.1.1 Set 1

For input set 1, the parameters that affect the BR are $\tan\beta$, m_A, μ, A_t and M_2. The dependence of the BR on these parameters and the ratio between the BRs calculated by SI and MO are displayed in figure 8. In general, we notice that the BRs calculated by MO and SI are shifted by a constant with respect to each other. This results in a ratio, which for most of the variations, is close to 1. For each parameter we provide a description and explanation of the observed behavior.

$\boxed{\tan\beta:}$ For both MO and SI, the BR increases with increasing values of $\tan\beta$. The influence of this parameter is relatively large compared to the other parameters. Analytically, this can be explained by the fact that $\tan^2\beta$ is present as a pre-factor in the equations of the Wilson coefficients. In the high $\tan\beta$ limit, the unprimed Wilson coefficients are even proportional to a factor $\tan^3\beta$. Considering the dominant Feynman diagrams contributing to $B_s^0 \to \mu^+\mu^-$, we can explain the influence by observing that many Higgs particles participate in the process. These Higgs couplings account for $\tan\beta$ contributions, explaining the large influence on the BR. The BR calculated by SI shows an increase for small $\tan\beta$, whereas the BR calculated by MO stays at an SM-like value. Next to this, for large values of $\tan\beta$ we also observe a deviation between the two BRs. These differences could be a result of the fact that MO performs the calculation based on the main NLO $\tan\beta$ contributions only, whereas SI takes all contributions into account and performs the calculation up to higher orders (for an overview see table 9). This is reflected by the ratio $R = \text{BR}(\text{B}_s \to \mu^+\mu^-)_{\text{SI}}/\text{BR}(\text{B}_s \to \mu^+\mu^-)_{\text{MO}}$, which becomes larger at both
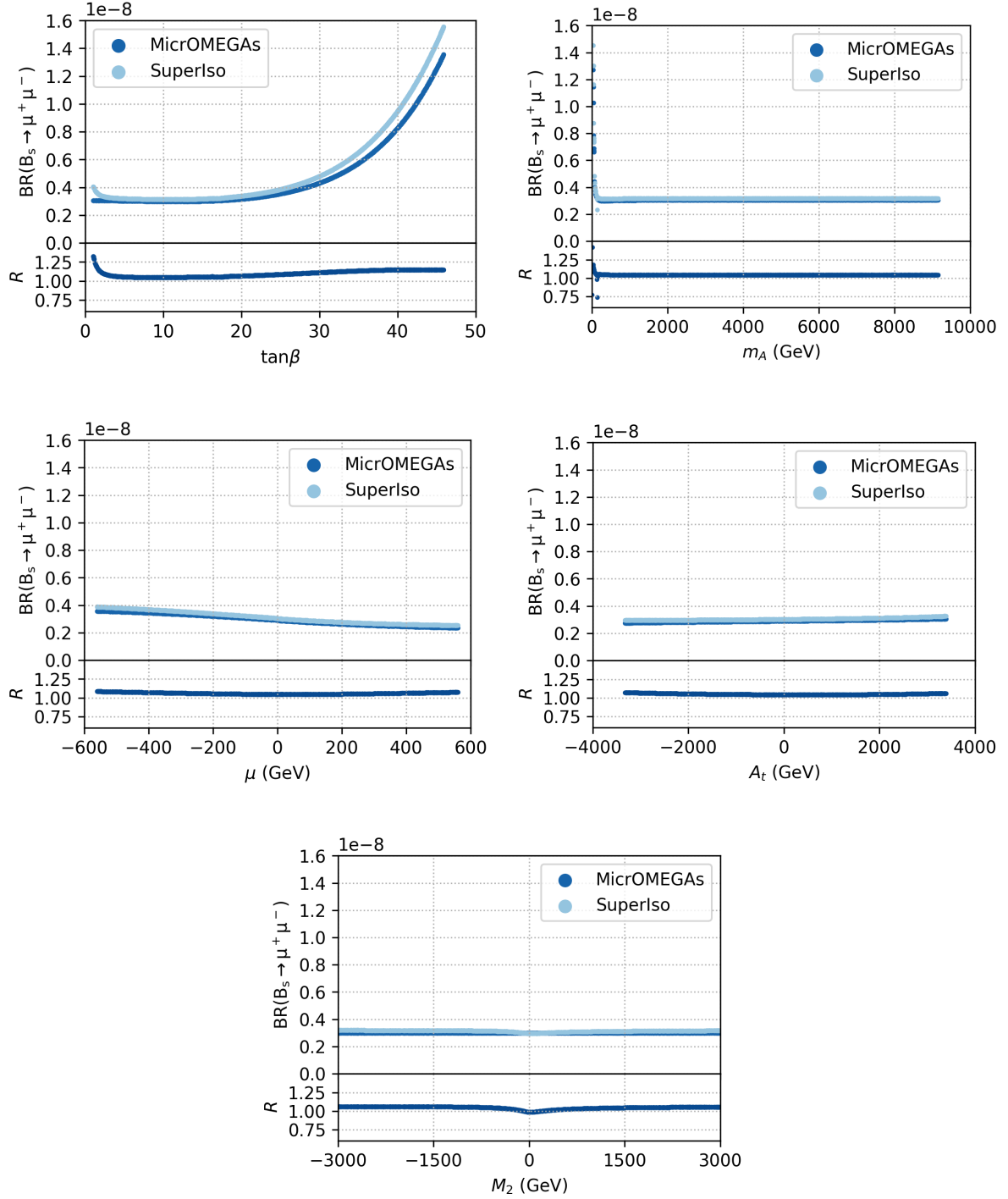
ends of the $\tan\beta$ range.

Figure 8: Overview of the BR behavior as a result of the variation of $\tan\beta$, m_A, μ, A_t and M_2 for input set 1. For each figure, the top panel displays the BRs calculated by MO and SI, and the bottom panel displays the ratio $R = \mathrm{BR}(\mathrm{B_s} \to \mu^+\mu^-)_{\mathrm{SI}}/\mathrm{BR}(\mathrm{B_s} \to \mu^+\mu^-)_{\mathrm{MO}}$.

$\boxed{m_A:}$ For almost all values of m_A there is no influence on the BRs calculated by MO and SI. However, for very small values of m_A (below $\sim$500 GeV), figure 8 shows an enormous increase in the BR for both programs. Unfortunately there are only few datapoints for small m_A values. Nevertheless, we can extrapolate between the points to see the behavior of the BR for small m_A. Analytically, we can explain

the behavior by noting that m_A^{-2} is present as a pre-factor in the equations of the Wilson coefficients. This can cause the BR to grow to large values for small m_A. Though for both programs the BRs become larger in the small m_A region, the (few) calculations show relatively large deviations between SI and MO, resulting in a larger ratio R. From a physics point of view, the constant and small BR value for large values of m_A is explained by the decoupling limit. For $m_Z \ll m_A$, the BR calculation may well be approximated by this limit.

$\boxed{\mu, A_t:}$ We combine the analysis of the influence of μ and A_t on the BR. As can be seen in figure 8, the influence of both parameters on the BR is little. The calculations performed by the two programs deviate only slightly, resulting in a ratio close to 1. Since this set has a large value for $\tan \beta$, we can (as explained in section 3.4.1) assume $C_{Q_1} \approx -C_{Q_2}$, and use equation 75 as an approximation for C_{Q_2}. The signs of $C_{Q_{1,2}}$ depend on the sign of the combination μA_t. To investigate the influence on the BR, we approximate equation 74 by

$$\text{BR}(B_s^0 \to \mu^+ \mu^-) \sim \text{pre-factor} \times \left[\left(1 - \frac{4m_\mu^2}{M_{B_s}^2} \right) \left(\frac{M_{B_s}}{m_b + m_s} \right)^2 |C_{Q_1}|^2 + \left| \left(\frac{M_{B_s}}{m_b + m_s} \right) - C_{Q_1} + 2C_{10} \frac{m_\mu}{M_{B_s}} \right|^2 \right],$$
(84)

where we have set the primed coefficients $C'_{Q_{1,2}}$ to zero, since we assume their contributions to be small with respect to the unprimed coefficients. This is because the primed coefficients are proportional to m_s, whereas the unprimed coefficients are proportional to m_b and $m_b \gg m_s$ (for a discussion on this see ref. [?]). The 'pre-factor' is defined as

$$\text{pre-factor} = \frac{G_F^2 \alpha^2 \tau_{B_s} M_{B_s}^3 f_{B_s}^2}{64\pi^3} |V_{tb} V_{ts}^*|^2 \sqrt{1 - \frac{4m_\mu^2}{M_{B_s}^2}}.$$
(85)

We plot equation 84, divided by the pre-factor, for varying C_{Q_1}. For m_μ, m_b and M_{B_s} we use the values listed in table 7, for m_s we use the value hard-coded in SI, which is $m_s = 0.096$ GeV and for C_{10} we use the value provided in ref. [33], which is $C_{10} = -4.134$. The results for $C_{Q_1} = [-0.5, 0.5]$ are displayed in figure 9. The light blue line represents the SM contribution, given by $\left| 2C_{10} \frac{m_\mu}{M_{B_s}} \right|^2$. The dark blue line indicates the BR including the SUSY contributions. We may observe that the total approximate BR becomes larger for large positive values of C_{Q_1}. However, for small negative values of C_{Q_1}, it becomes smaller than the SM contribution. This means that small negative values of C_{Q_1} (and small positive C_{Q_2} values) can lead to a suppression of the BR below the SM value. As C_{Q_1} becomes more negative, the total approximate BR again increases. As mentioned before, the sign of the combination μA_t determines the sign of C_{Q_1}. For a negative combination of μA_t, C_{Q_1} is positive, whereas for a positive combination of μA_t, C_{Q_1} is negative. From this we can deduce that negative combinations of μA_t can enhance the BR, whereas positive combinations μA_t can, depending on the size of μA_t, either reduce or enhance the BR.

We can use the above to explain the influence of μ and A_t on the BR. Figure 8 shows that for negative values of μ the BR is larger than for positive values of μ. Since A_t is positive for this set, we can explain this by considering the sign of the combination μA_t. For negative values of μ this sign is negative, leading to a larger BR. For positive values of μ the sign of the combination is positive, leading to a smaller BR. Based on the behavior of the BR displayed in figure 9, we expect the BR to become larger again for larger values of μ. However, no datapoints were found for this regime. For the variation of A_t we observe only very little change of the calculated BRs. The BR becomes slightly larger for positive values of A_t than it is for negative values of A_t. To explain this behavior, we can apply the same analysis as used for μ, thereby noting that the value of μ for this set is negative. The reason that we only observe a little change of the BR could be that μ is very small for this set ($\mu = -49.65$ GeV). Therefore, the variation of the value of A_t has less influence on the size of the combination μA_t than the variation of the value of μ, resulting in a smaller effect on the BR.
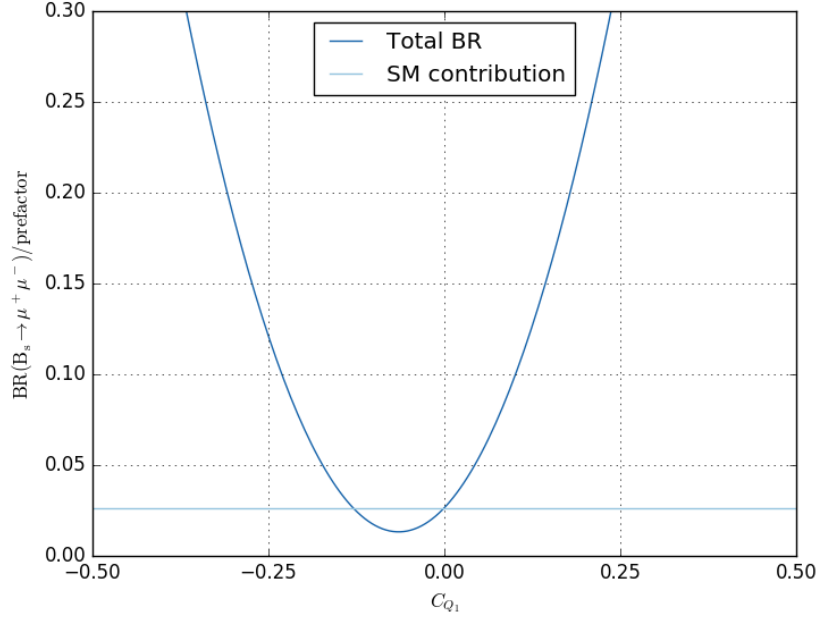
Figure 9: Approximate BR equation (equation 84) divided by the prefactor (equation 85), as a function of C_{Q_1}. Both the SM contribution and the total BR, including SUSY contributions, are shown. Since an approximate equation is used, the values on the y-axis are not related to real BR values.

$\boxed{M_2:}$ The result of the variation of M_2 shows that the BR calculated by MO remains unaffected, whereas the SI BR shows a small dip around zero. This behavior is interesting, however it is not very significant. It is however interesting that there is a difference between the two programs. We can explain the behavior of SI by looking at the chargino composition. As explained in section 2.2.1, the dominant component of a chargino is, amongst others, determined by the relative magnitude of M_2 and $|\mu|$ (for an overview see table 6). As $|\mu|$ is very small for this set ($|\mu| = 49.65$ GeV), only for very small values of M_2 there will be a shift in the composition of the lightest chargino. This may result in the observed behavior of the BR. Unfortunately, we were not able to explain why this composition shift does not affect the MO calculation.

6.1.2 Set 2

For input set 2, the parameters that affect the BR are $\tan\beta$, m_A, μ, A_t, M_2, $m_{\tilde{Q}_1}$, $m_{\tilde{Q}_3}$ and $m_{\tilde{t}_R}$. The dependence of the BR on these parameters and the ratio between the BRs calculated by SI and MO are displayed in figure 10 and 11. Again we notice that the BRs calculated by MO and SI, in many cases, seem to be shifted by a constant. Similar to set 1 for this set, the variations are performed in the large $\tan\beta$ limit (for set 2 $\tan\beta = 35.48$) For each parameter we provide a description and explanation of the observed behavior.

$\boxed{\tan\beta:}$ For both MO and SI, the BR increases enormously with increasing values of $\tan\beta$. We can explain this influence in the same way as we did for set 1. Similar to set 1, we observe a difference between SI and MO in the high $\tan\beta$ regime. However, for this set, the BR calculated by MO becomes larger than the BR calculated by SI, resulting in a ratio much smaller than 1. Unfortunately, we are not able to explain this difference.

$\boxed{m_A:}$ Similar to set 1, we observe for both MO and SI a constant SM-like BR for large values of m_A. For these values, we are in the decoupling limit. For small values of $\tan\beta$ the ratio between the two BRs drops, whereas for set 1, it became larger. We do not know why this difference occurs between the two sets. Note that for this set, for small values of m_A (< 500 GeV), no data points were found.
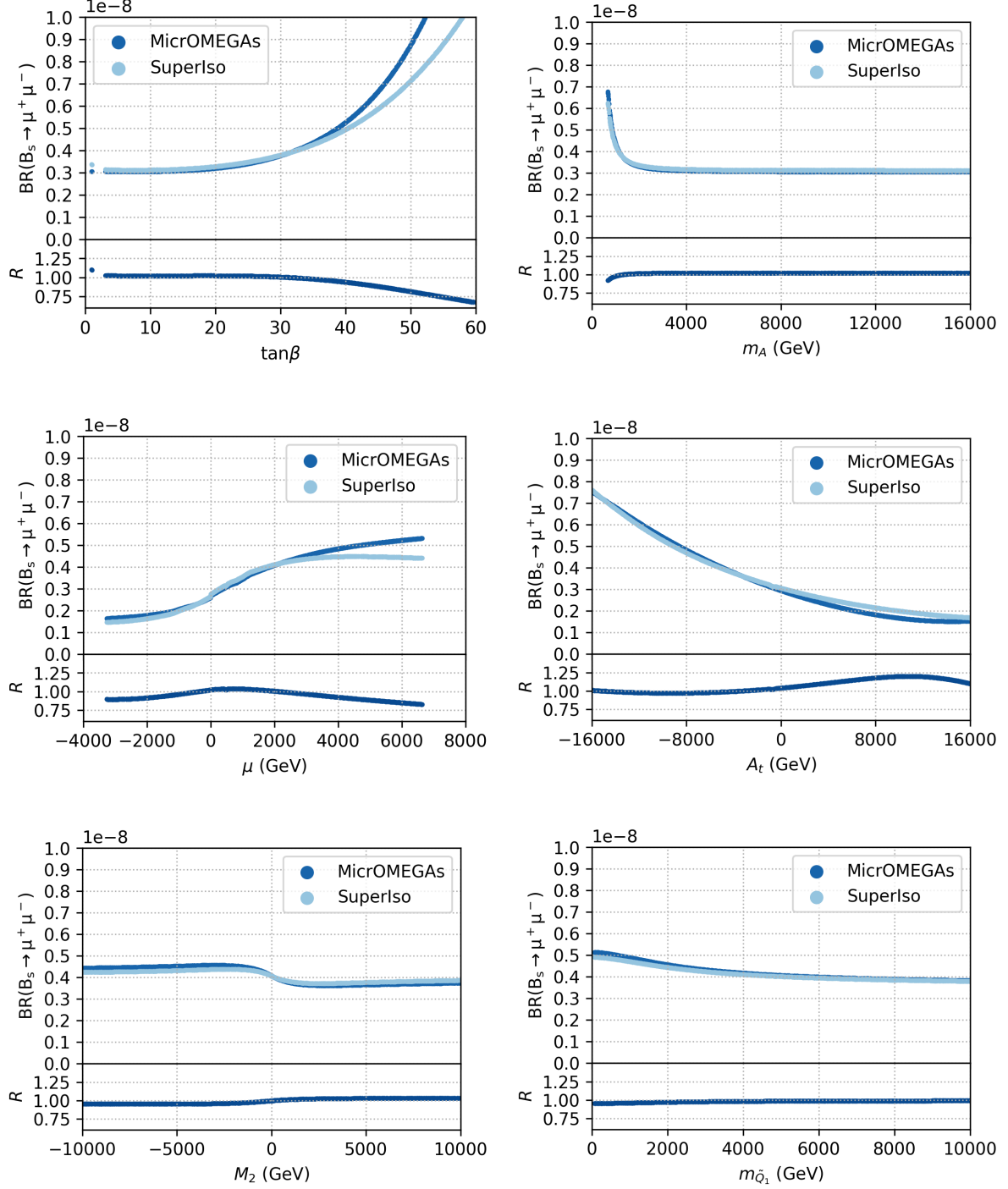
Figure 10: Overview of the BR behavior as a result of the variation of $\tan\beta$, m_A, μ, A_t, M_2 and $m_{\tilde{Q}_1}$ for input set 2. For each figure, the top panel displays the BRs calculated by MO and SI, and the bottom panel displays the ratio $R = \mathrm{BR}(\mathrm{B_s} \to \mu^+\mu^-)_{\mathrm{SI}}/\mathrm{BR}(\mathrm{B_s} \to \mu^+\mu^-)_{\mathrm{MO}}$.

$\boxed{\mu,\ A_t:}$ In contrast with set 1, we observe that for negative values of μ, the BR calculated by MO and SI is smaller, whereas for positive values it becomes larger. This reversed behavior occurs, because for this set, A_t is negative, whereas for set 1 it is positive. Based on figure 9, for very small values of μ, we expect the BR to become larger. However, no datapoints were found for this region, and therefore we are unable to check if we observe the expected behavior. Furthermore, we observe that the BRs calculated by MO and SI start to deviate for large values of μ, leading to a smaller ratio. Next to this, for small values of μ this ratio suddenly increases. Unfortunately, we are not able to explain these ratio changes. For A_t we

40

also observe a reversed behavior with respect to set 1. For negative values of A_t the BR becomes larger, whereas for positive values of A_t it becomes smaller. Similar to μ, this can be explained by noting that for this set, μ is positive, whereas for set 1 it was negative. For large positive values of A_t we expect, similar as for μ, the BR to become larger again. However, the figure for A_t does not show the expected behavior. What does stand out, is that for large values of A_t, the ratio between MO and SI becomes larger. Unfortunately, we do not have an explanation for this. Lastly, we note that the observed change in the BR due to the variation of both parameters is larger. This could be caused by the fact that the values for $\tan\beta$, μ and A_t for this set are much larger than for set 1. This leads to larger contributions to $C_{Q_{1,2}}$ and therefore to a larger variation of the BR.

$\boxed{M_2:}$ Both for MO and SI the change in the BR for varying values of M2 is quite small. We do however observe that for negative values of M_2, the BR is slightly larger than for positive values. Similar to set 1, we can relate the behavior of M_2 to the chargino composition. For this set, the value of $|\mu|$ is $|\mu| = 2723$ GeV. The change in composition due to $|M_2|$ being smaller or larger than $|\mu|$ results in the observed variation of the BR.

$\boxed{m_{\tilde{Q}_1}:}$ Though the influence is very small, we do observe a change in the BR for both MO and SI if $m_{\tilde{Q}_1}$ becomes smaller. Since for this set $|M_2| < |\mu|$, in the chargino diagrams presented in section 3.3, the lightest chargino will be wino-like and couple to left-handed squarks. Furthermore, for this set it holds that $m_{\tilde{Q}_1} < m_{\tilde{u}_R}$, meaning that the lightest squark is also left-handed. Small values of $m_{\tilde{Q}_1}$, being in that case the lightest squark, will therefore result in the observed higher BR. We did not see a significant influence of $m_{\tilde{Q}_1}$ on the BR in set 1. This is because for set 1, $|M_2| < |\mu|$ does not hold and $m_{\tilde{u}_R}$ is very small ($m_{\tilde{u}_R} = 554.6$ GeV).
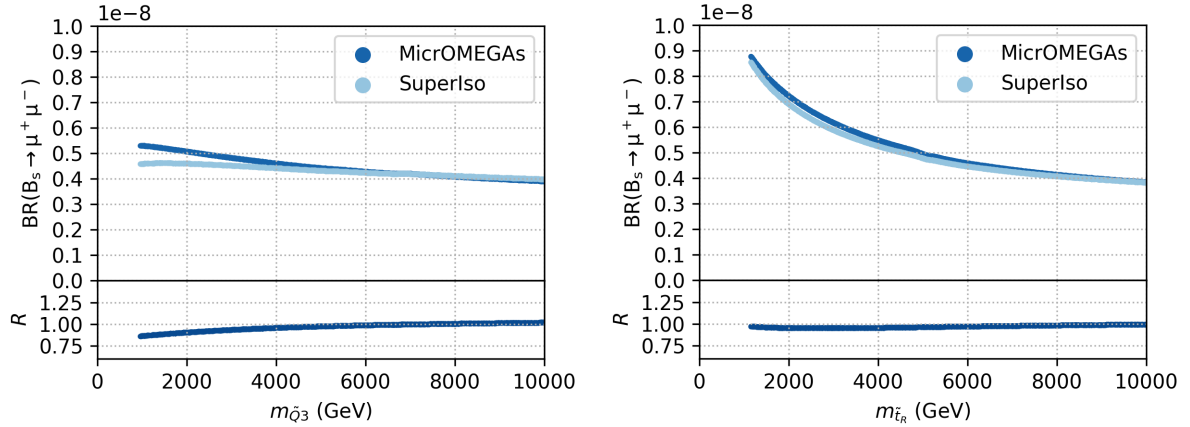

Figure 11: Overview of the BR behavior as a result of the variation of $m_{\tilde{Q}_3}$ and $m_{\tilde{t}_R}$ for input set 2. For each figure, the top panel displays the BRs calculated by MO and SI, and the bottom panel displays the ratio $R = \mathrm{BR}(\mathrm{B_s} \to \mu^+\mu^-)_{\mathrm{SI}}/\mathrm{BR}(\mathrm{B_s} \to \mu^+\mu^-)_{\mathrm{MO}}$.

$\boxed{m_{\tilde{Q}_3},\, m_{\tilde{t}_R}:}$ We combine the analysis of $m_{\tilde{Q}_3}$ and $m_{\tilde{t}_R}$ Similar to $m_{\tilde{Q}_1}$, the variation of $m_{\tilde{Q}_3}$ shows little change in the BR. For the variation of $m_{\tilde{t}_R}$ we observe a much larger influence on the BR. We can explain the influence of $m_{\tilde{Q}_3}$ and $m_{\tilde{t}_R}$ by looking at the largest contributions to the Wilson coefficients $C_{Q_{1,2}}$ in the large $\tan\beta$ limit in equation 75. This equation is proportional to $f(x)(x\mu^2)^{-1}$, where $x = m_{\tilde{t}}^2/\mu^2$ and $m_{\tilde{t}} = \sqrt{m_{\tilde{t}_1}m_{\tilde{t}_2}} = M_{\mathrm{SUSY}}$. The function $f(x)$ is given by equation 76. Figure 12 shows a plot of $f(x)(x\mu^2)^{-1}$ for $x = [0, 100]$ and $\mu^2 = 100$ GeV^2. As can be seen from the figure, for small values of x, meaning $m_{\tilde{t}}^2 = M_{\mathrm{SUSY}}^2 < \mu^2$, the function increases. An increasing value of the factor $f(x)(x\mu^2)^{-1}$ enhances the value of $C_{Q_{1,2}}$ and therefore increases the BR. Though M_{SUSY} is defined as $M_{\mathrm{SUSY}} \equiv \sqrt{m_{\tilde{t}_1}m_{\tilde{t}_2}}$, in order to generate the spectrum, SP calculates it using the values for $m_{\tilde{Q}_3}$ and $m_{\tilde{t}_R}$. It seems like the program uses the equation $M_{\mathrm{SUSY}} = \sqrt{m_{\tilde{Q}_3}m_{\tilde{t}_R}}$, however, the value for M_{SUSY} used by the program differs a few GeV from the value calculated using this formula. We do not know the exact way in which SP determines M_{SUSY}, but assume that it is related to $m_{\tilde{Q}_3}m_{\tilde{t}_R}$. For small combinations of $m_{\tilde{Q}_3}m_{\tilde{t}_R}$, M_{SUSY} becomes smaller, and therefore the BR becomes larger. This is exactly

the behavior that we observe in the figures for $m_{\tilde{Q}_3}$ and $m_{\tilde{t}_R}$. For both parameters, the BR increases for small parameter values. However, the influence of $m_{\tilde{t}_R}$ on the BR is much larger than that of $m_{\tilde{Q}_3}$. This can be explained by looking at the values for both parameters for this set ($m_{\tilde{Q}_3} = 5051$ GeV, $m_{\tilde{t}_R} = 6672$ GeV). If $m_{\tilde{Q}_3}$ is kept constant and $m_{\tilde{t}_R}$ is varied, M_{SUSY} can become smaller than for the situation where $m_{\tilde{t}_R}$ is kept constant and $m_{\tilde{Q}_3}$ varied. This results in a larger increase of the BR for small values of $m_{\tilde{t}_R}$. Note that for set 1 we did not observe any influence of $m_{\tilde{Q}_3}$ and $m_{\tilde{Q}_3}$ on the BR. This is because for set 1, μ is much smaller than for set 2, resulting in larger values of M_{SUSY}^2/μ^2 and therefore a smaller contribution to $C_{Q_{1,2}}$. Next to this, the value of A_t for set 1 is smaller than that for set 2. As can be seen from equation 75, together with small μ, this results in a smaller contribution to $C_{Q_{1,2}}$. Lastly, since for this set M_{SUSY} is also smaller than for set 2, decreasing values of $m_{\tilde{Q}_3}$ and $m_{\tilde{t}_R}$ result in smaller effects on the BR. The lack of data points for small values of $m_{\tilde{Q}_3}$ and $m_{\tilde{t}_R}$ (i.e. < 1000 GeV) can be explained by the large parameter values of set 2. For this region, no viable spectra could be calculated.
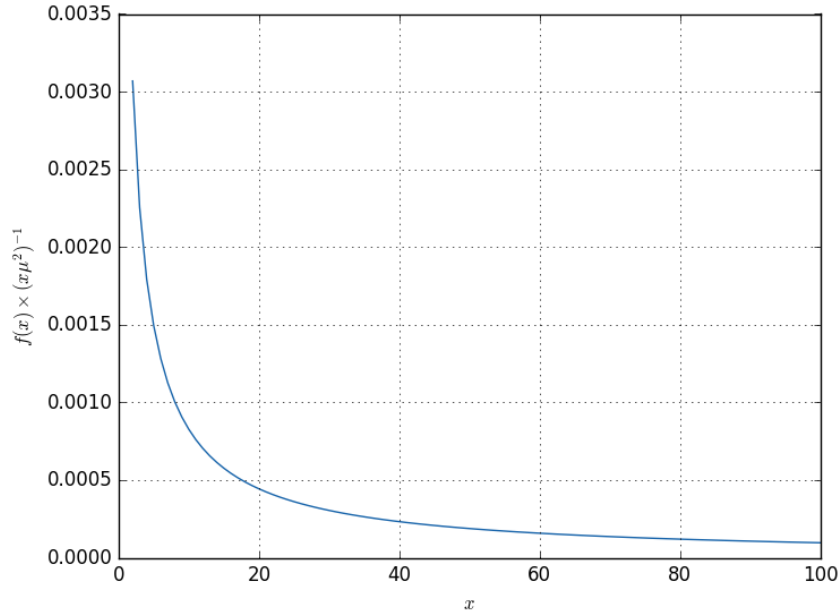

Figure 12: Plot of the factor $f(x)(x\mu^2)^{-1}$ for $x = m_{\tilde{t}}^2/\mu^2$ and $\mu^2 = 100$ GeV^2.

6.1.3 Set 3

For input set 3, the parameters that affect the BR are $\tan\beta$ and m_A. The influence of these parameters on the BR and the ratio between the BRs calculated by SI and MO are displayed in figure 13. As explained before, due to the large value of m_A, for this set we are in the decoupling limit. It is therefore that for all input parameters, we observe less influence on the BR. Because of the small variation, we look at a smaller range for the BR. This makes the shift by a constant between MO and SI more prominent in all figures. For each parameter we provide a description and explanation of the observed behavior.

$\boxed{\tan\beta\text{:}}$ Similar to sets 1 and 2 we observe an increase of the BR for increasing values of $\tan\beta$. The observed influence can be explained in the same way as for the previous sets. However, it should be noted that, because m_A is large, the increase of the BR for this set is relatively small. Note that for set 3, the BR calculated by SI is always larger than the BR calculated by MO. This is similar to set 1, whereas for set 2 the MO BR is larger than the SI BR.

$\boxed{m_A\text{:}}$ The variation of m_A results in similar behavior of the BR as for sets 1 and 2. For large values of m_A we are in the decoupling limit. For small values (< 1000 GeV), the BR increases due to the $1/m_A$ factor in the equations for the Wilson coefficients.
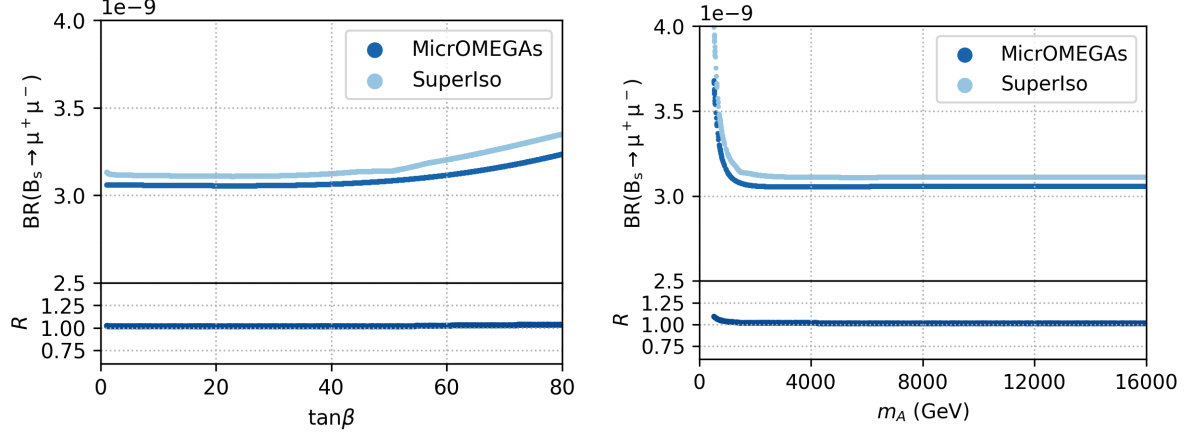
Figure 13: Overview of the BR behavior as a result of the variation of $\tan\beta$ and m_A for input set 3. For each figure, the top panel displays the BRs calculated by MO and SI, and the bottom panel displays the ratio $R = \mathrm{BR}(\mathrm{B_s} \to \mu^+\mu^-)_{\mathrm{SI}}/\mathrm{BR}(\mathrm{B_s} \to \mu^+\mu^-)_{\mathrm{MO}}$.

6.1.4 Summary

As explained in the introduction of this section, we expected the parameters $\tan\beta$, m_A, A_t, μ, M_2, M_3 and the squark masses $(m_{\tilde{Q}_1}, m_{\tilde{Q}_3}, m_{\tilde{u}_R}, m_{\tilde{t}_R})$ to influence the BR. After the analysis of the three different sets used for the single parameter variation, we observe that only the parameters $\tan\beta$, m_A, A_t, μ, M_2, $m_{\tilde{Q}_1}$, $m_{\tilde{Q}_3}$ and $m_{\tilde{t}_R}$ significantly influence the BR. Furthermore, we observe that an increasing value of $\tan\beta$ leads to an enormous increase of the BR. Next to this, the choice of m_A strongly controls whether we find an SM-like BR (which happens in the decoupling limit) or an increased BR (for small m_A). The influence of the parameters A_t and μ differs per set. For set 1 the values of both parameters are small. Therefore, the combination μA_t remains relatively small, leading to only a small influence on the BR. For set 2, the values of both parameters are large, leading to a larger influence on the BR. Since set 3 is in the decoupling limit, the influence of A_t and μ is suppressed, therefore we do not observe a significant influence of both parameters on the BR. Similar to A_t and μ the influence of M_2 also differs per set. The behavior of the BR for the variation of M_2 is related to the chargino composition, which is determined by the relative values of, amongst others, $|M_2|$ and $|\mu|$. For set 1, the value of $|\mu|$ is very small, therefore we only see a small influence on the BR as a result of the shifting chargino composition. However, for set 2, $|\mu|$ is much larger, leading to a larger change of the BR for varying M_2. Again, since set 3 is in the decoupling limit, we do not observe any influence of M_2 on the BR for this set. The effect of the parameters $m_{\tilde{Q}_1}$, $m_{\tilde{Q}_3}$ and $m_{\tilde{t}_R}$ on the BR was only visible for set 2. Considering $m_{\tilde{Q}_1}$, this is because for set 2, $m_{\tilde{Q}_1} < m_{\tilde{u}_R}$ and $|M_2| < |\mu|$, whereas for set 1 this does not hold. Considering $m_{\tilde{Q}_3}$ and $m_{\tilde{t}_R}$, we do not observe a significant influence on the BR, because for set 1, M_{SUSY} is lower than set 2. Next to this, set 1 has lower values for μ and A_t resulting in smaller contributions to $C_{Q_{1,2}}$ than for set 2. Again, we observe no influence of $m_{\tilde{Q}_1}$, $m_{\tilde{Q}_3}$ and $m_{\tilde{t}_R}$ for set 3 because of the decoupling limit. A general thing that stands out in the analysis of all three sets, is that in many cases the BRs of MO and SI seem to be shifted by a constant. This could be related to the choice of scales (μ_W, μ_b) for SI, which we also encountered in our SM analysis in chapter 5. We will further investigate the difference between MO and SI and the relation to the choice of scales in section 6.3.

6.2 Random pMSSM scan

After having studied the influence of the variation of a single parameter for a specific pMSSM input set, we will now perform a random scan of the 19D pMSSM parameter space. This numerical approach should provide us with more insight in the relations between the BR and the pMSSM input parameters.

To perform the random scan, we use the same parameter ranges as for the single parameter variation. These ranges are listed in table 14. We have selected 725000 random sets of input parameters within these ranges. All sets have a Higgs mass between 122 and 128 GeV and the lightest neutralino is the LSP. For SI, the used scales are the default scales for the SLHA option ($\mu_W = M_W$ and $\mu_b = m_b$).

The results are shown in figures 14 and 15. These figures show the relation between the BR calculated by SI and MO and the parameters m_A and $\tan\beta$, as we have seen in the previous section that these are the dominant parameters. The results of the random scan show that the BR becomes, in the case of small m_A, larger for larger values of $\tan\beta$. When m_A becomes larger, the decoupling limit is approached, resulting in less influence of $\tan\beta$ and an SM-like BR. Both figures show some points with small m_A values and a BR below the SM value. The $\tan\beta$ values of these points vary between small and large. What happens for these points, is that the contribution of C_{Q_2} destructively interferes with the contribution of C_{10}, while C_{Q_1} is small. Looking back at figure 9, we recognize this behavior in the limit of large $\tan\beta$. The figure shows that when $C_{Q_1} \approx -C_{Q_2}$ becomes negative and small, the BR is suppressed below the SM value. However, for the points with small $\tan\beta$, we are not able to explain why the destructive interference of the contributions, and therefore the BR suppression, occurs. This is left for future research.

None of the other pMSSM parameters or combinations of these parameters showed such clear relations with respect to the BR as m_A and $\tan\beta$. We already encountered the major influence of these two parameters when we performed the single parameter variation in the previous section. Since also the random scan shows their large influence on the BR (compared to the other parameters), we can conclude that m_A and $\tan\beta$ are the parameters that mainly determine the BR of $B_s^0 \to \mu^+\mu^-$ in the pMSSM.

Figure 14: Logarithmic plot of the relation between m_A, $\tan\beta$ and the theoretical BR calculated by SI. The value of $\tan\beta$ is indicated by the color of the dots. The values range from light-blue ($\tan\beta = 1$) up to dark-blue ($\tan\beta = 80$). Each dot represents an individual set of 19 pMSSM parameters, they are plotted in random order.
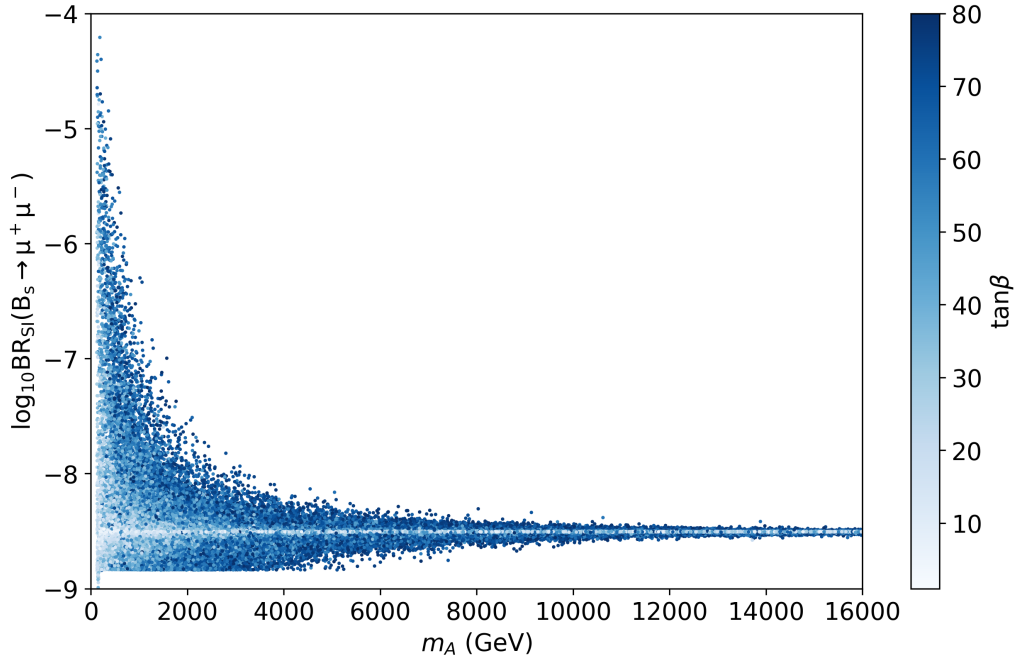
Figure 15: Logarithmic plot of the relation between m_A, $\tan\beta$ and the theoretical BR calculated by MO. The value of $\tan\beta$ is indicated by the color of the dots. The values range from light-blue ($\tan\beta = 1$) up to dark-blue ($\tan\beta = 80$). Each dot represents an individual set of 19 pMSSM parameters, they are plotted in random order.
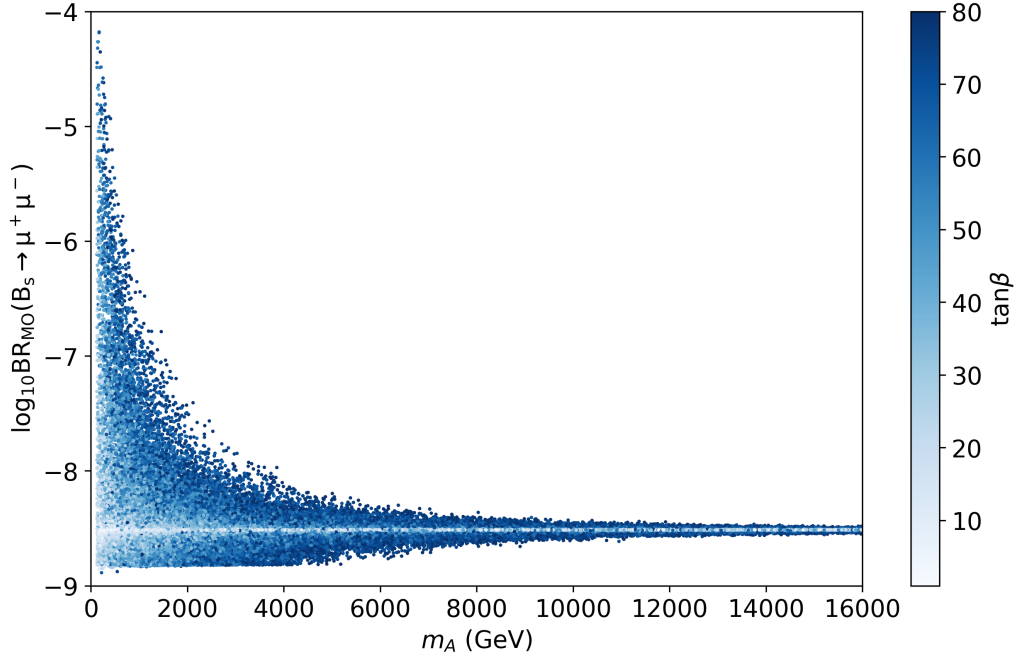
6.3 Scale variations

In the results of the single parameter variation, performed in section 6.1, we observed a difference between the BRs calculated by MO and SI. In some cases there seemed to be a shift by a constant value between the two programs, whereas in other cases the two programs show different behavior. The differences between MO and SI can partly be explained by the fact that MO takes less contributions into account than SI. However, the approximation used by MO should work in the large $\tan\beta$ limit. Since we still observe a difference between MO and SI in this limit, there must be another reason for these differences. The comparison of the SM BR calculations already showed the large influence of the choice of scales for SI. As mentioned before, the choice of scales for MO is not apparent in the code or manual, whereas for SI these scales can be set to specific values within the code. To investigate whether the choice of scales explains the observed differences, we compare the BR calculated by MO with the BR calculated by SI for different combinations of scales. By doing this we hope to find out if MO agrees with SI within these scale variations. The used combinations are the same as for the SM comparison: $\mu_W \in \{0.5M_W, M_W, 2M_W\}$ and $\mu_b \in \{0.5m_b, m_b, 2m_b\}$, where m_b is the pole mass of the bottom quark. We apply this scale variation to both the single parameter variation and to the random pMSSM scan. The results are provided in the next sections.

6.3.1 Single parameter variation

To investigate the influence of the choice of scales on the single parameter variation, we have taken input set 2 (table 10) as a starting point. Again we vary each parameter separately, while keeping the rest at a constant value. However, in this case, we calculate the SI BR for all 9 combinations of scales.

The results of the additional calculations for the parameters $\tan\beta$ and $m_{\tilde{t}_R}$ are displayed in figures 16 and 17. Because all parameters show similar results, we have chosen to show these two parameters as an example. For SI, the figures show a bandwidth. This bandwidth represents the BR variation due to the use of different scale combinations. It is created by taking the maximum and minimum of all calculated SI BR values for each input set. These maxima and minima do not always belong to the same scale combination. Next to the SI bandwidth, the BR calculated by MO for each input set is shown.

Figure 16: BR behavior as a result of the variation of $\tan\beta$ for input set 2 (table 10). For SI a bandwidth is shown, which represents the variation of the BR value due to the different combinations of scales.
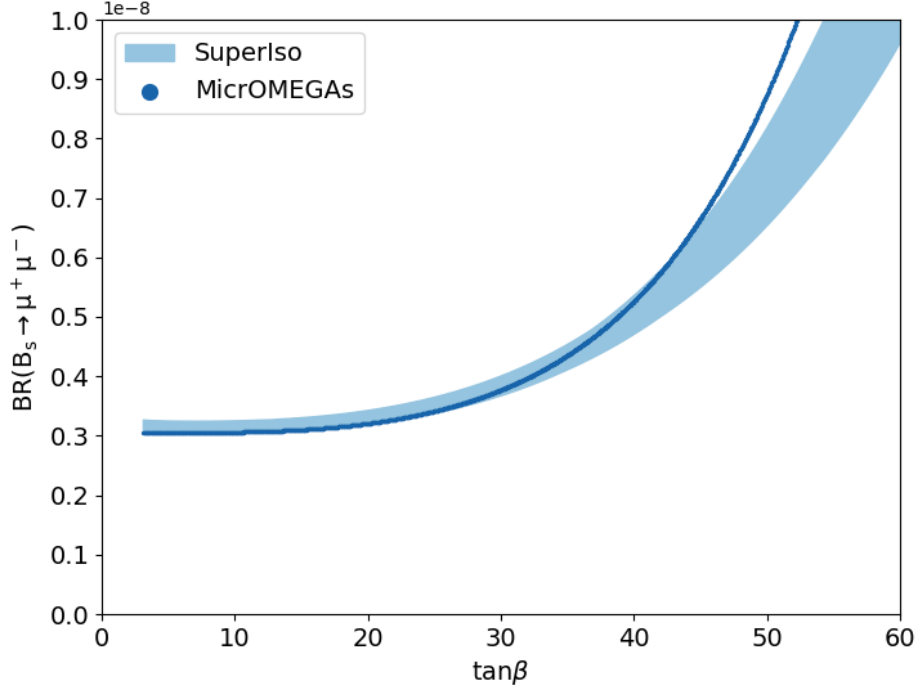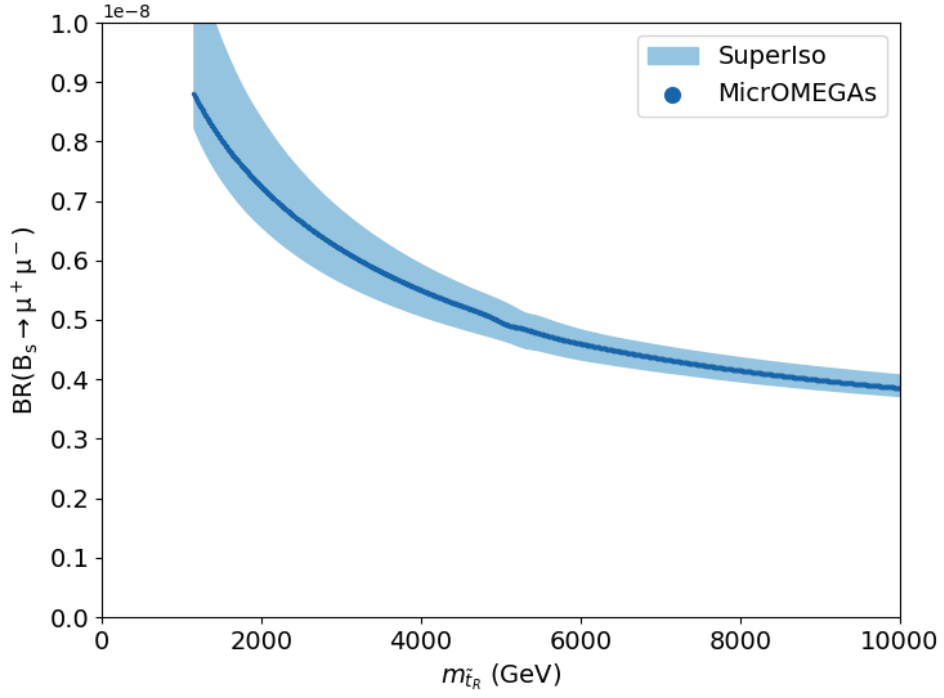

Figure 17: BR behavior as a result of the variation of $m_{\tilde{t}_R}$ for input set 2 (table 10). For SI a bandwidth is shown, which represents the variation of the BR value due to the different combinations of scales.

For the variation of $\tan\beta$ we observe that, up to $\tan\beta = 40$, the MO BR lies within the SI bandwidth. For larger values of $\tan\beta$, the MO BR and the SI band start to deviate. This deviation could be a result of the different contributions that are taken into account by both programs. However, note that this is a speculation, since we do not fully understand what happens in this region. If we look at the variation of $m_{\tilde{t}_R}$, we observe that the MO BR lies completely within the SI bandwidth. It should also be noted that for both parameters, the width of the SI band changes over the parameter range. This means that for certain regions the deviation in the SI BR, due to the scale choice, is larger than for other regions. As mentioned before, we showed these two parameters as an example. For the other parameters, the MO BR lies (mostly) within the SI bandwidth.

Since for all parameters, the BR calculated by MO agrees (to a large extent) with the bandwidth for SI, we can conclude that the observed shift between the two programs is mainly a result of the choice of scales. Although we do not know which scales are used by MO, the scales used by SI can always be chosen in such a way (within reasonable ranges) that the BRs calculated by both programs are similar.

6.3.2 Random pMSSM scan

To investigate the influence of the choice of scales on the random scan, we take each random input set and perform the SI BR calculation for all 9 scale combinations. Because of the large calculation time, we did this for 300000 of the 725000 random input sets.

The results of these calculations are displayed in figure 18. The dark blue line represents the BR calculated by MO for each of the 300000 input sets. The light-blue band corresponds to the variation of the BR calculation by SI for different scale choices. As can be seen from the figure, for every input set, the MO BR resides within the SI band. This differs from what we saw for the scale variations performed for the single parameter variation. This can be caused by the fact that for both analyses different input sets are used. What also stands out in figure 18, is that the width of the SI band differs per MO value. This is something that we also observed for the single parameter variation. Unfortunately we do not know why this happens. Based on figure 18, we can conclude that, similar to the single parameter variation, the differences between the programs arise from the choice of scales.

As an addition, we perform an analysis in which we determine the percentage difference of the highest and lowest BR with respect to the default SI BR (calculated using the default scale set, $\mu_W = M_W$ and $\mu_b = m_b$) for each input set. Next, we calculate a weighted average ($\bar{x}_{\text{weighted}}$) of this percentage difference by using the following equation

$$\bar{x}_{\text{weighted}} = \frac{\sum_{i=1}^{N} x_i G_i}{\sum_{i=1}^{N} G_i}. \tag{86}$$

Here x_i is the percentage difference for each individual input set and G_i are the weights, which are defined as

$$G_i = \frac{1}{(x_i - \mu)}, \tag{87}$$

where μ is the average of all percentage differences x_i. By using the weighted average, we correct for the presence of extreme BR variations. As a result, we find a weighted average deviation of $+7.76\%$ and -2.48% with respect to the default value.
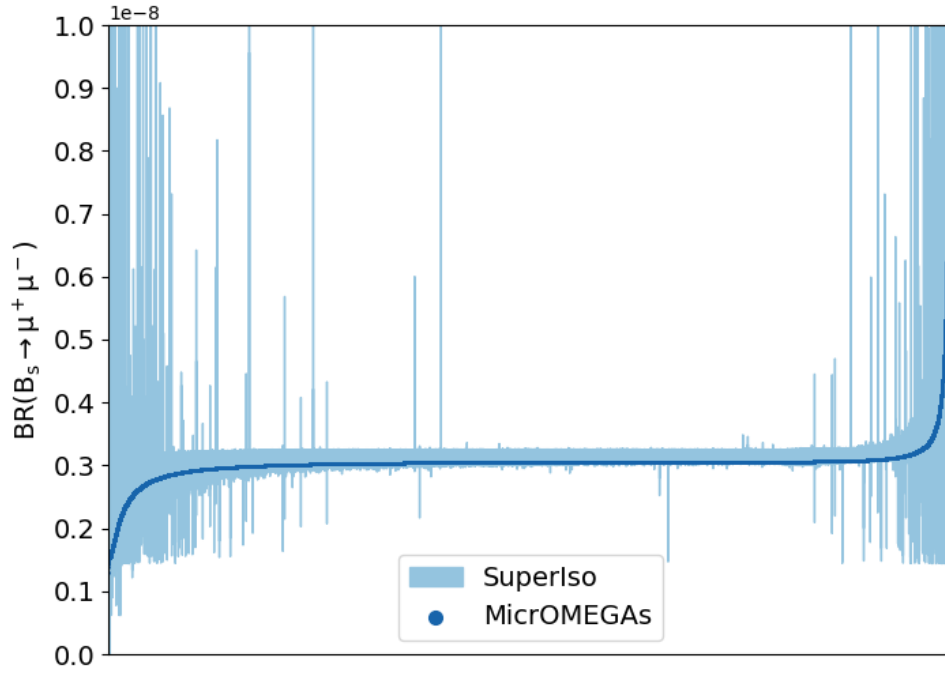
Figure 18: BR values for 300.000 random pMSSM input sets. The dark blue line represents the BR calculated by MO for each set. The light blue band represents the BR values calculated by SI for the 9 different scale sets. For each input set, a line is drawn between the highest and lowest SI BR, resulting in the displayed band.

7 Conclusion and Outlook

In this research, we compare the calculations of $\mathrm{BR}(B_s^0 \to \mu^+\mu^-)$ performed by the programs SuperIso (SI) and MicrOMEGAs (MO) within the pMSSM. A study of the manuals, reference papers, and code reveals multiple differences between the two computational tools. Firstly, there is a difference between the types of calculations that can be performed by the two programs. SI is able to calculate both the theoretical and the time-integrated BR, whereas MO can only calculate the theoretical BR. Next, the tools use different hard-coded values for the parameters involved in the calculation. Furthermore, the programs take different contributions into account to perform the calculation: MO includes the main $\tan\beta$ NLO contributions, whereas SI includes two-loop EW (NNLO) and three-loop QCD (NNNLO) contributions. Moreover, the primed Wilson coefficients, and the SUSY contributions to the C_{10} Wilson coefficient are neglected in MO. A final, important difference concerns the choice of scales used to calculate the Wilson coefficients (μ_W) and to perform the calculations (μ_b). MO does not provide any clarity on the chosen scales, whereas for SI, the scales can be manually adjusted in the code.

To analyze the differences between the two programs in the pMSSM, two numerical approaches are used. Firstly, the influence of the individual pMSSM parameters on the BR is investigated. Secondly, a random pMSSM scan is executed and used for BR calculations. Both analyses show that the BR calculated by MO does not agree with that calculated by SI. A subsequent analysis is performed for both approaches, in which the scales used by SI are varied. This analysis identifies the choice of scales as the main cause of the observed differences between the two programs. The effects of the other differences are very small compared to the effect of the scale choice. When the scales in SI are chosen within a reasonable range ($\mu_W = 0.5M_W$-$2M_W$ and $\mu_b = 0.5m_b$-$2m_b$), the calculations performed by the two programs agree. Both the analysis of the influence of individual parameters and the random scan show that the parameters that influence the BR most are $\tan\beta$ and m_A.

With respect to MO, the calculation performed by SI is more complete, because SI is able to perform calculations up to higher orders, takes all relevant contributions into account and is able to calculate the time-integrated BR. Therefore, SI is the best choice to perform the BR calculation in the pMSSM. However, we would like to stress that an uncertainty band on the calculated BR value, based on the scale variation, needs to be provided by the program as a default.

In this thesis, we did not consider the BR calculation performed by SP. An analysis of the calculation performed by this program could be a follow up to this project. Since this program uses running couplings and masses, it will be interesting to compare its performance to the programs we analyse in this thesis.

References

[1] Observation of the rare $B_s^0 \to \mu^+\mu^-$ decay from the combined analysis of CMS and LHCb data. *Nature*, 522(7554):68–72, May 2015. http://dx.doi.org/10.1038/nature14474.

[2] A. Arbey, M. Battaglia, F. Mahmoudi, D. Martínez Santos. Supersymmetry confronts $B_s \to \mu^+\mu^-$: Present and future status. *Phys. Rev.*, D87(3):035026, 2013. https://arxiv.org/abs/1212.4887.

[3] P. Tanedo A. Dedes, J. Rosiek. Complete one-loop MSSM predictions for $B^0 \to \ell^+\ell'^-$ at the Tevatron and LHC. *Phys. Rev.*, D79:055006, Mar 2009. https://link.aps.org/doi/10.1103/PhysRevD.79.055006.

[4] A.J. Buras. Weak Hamiltonian, CP violation and rare decays. In *Probing the standard model of particle interactions. Proceedings, Summer School in Theoretical Physics, NATO Advanced Study Institute, 68th session, Les Houches, France, July 28-September 5, 1997. Pt. 1, 2*, pages 281–539, 1998. https://arxiv.org/abs/hep-ph/9806471.

[5] A.J. Buras, R. Fleischer, J. Girrbach, Jennifer, R. Knegjens. Probing New Physics with the B_s to $\mu^+\mu^-$ Time-Dependent Rate. *JHEP*, 07:77, 2013. https://arxiv.org/abs/1303.3820.

[6] A.V. Radyushkin. Introduction into QCD sum rule approach. In *Strong interactions at low and intermediate energies. Proceedings, 13th Annual Hampton University Graduate Studies, HUGS'98, Newport News, USA, May 26-June 12*, 1998. http://www1.jlab.org/Ul/publications/view_pub.cfm?pub_id=1220.

[7] W. Beenakker. *Reader for the course Quantum Field Theory*, pages 28–32. https://www.hef.ru.nl/~wimb/dictaat_QFT_old.pdf.

[8] W. Beenakker. The Standard Model and Beyond, 2018. https://www.hef.ru.nl/~wimb/.

[9] C. Bobeth, A.J. Buras, F. Kruger, J. Urban. QCD corrections to $\bar{B} \to X_{d,s}\nu\bar{\nu}$, $\bar{B}_{d,s} \to \ell^+\ell^-$, $K \to \pi\nu\bar{\nu}$ and $K_L \to \mu^+\mu^-$ in the MSSM. *Nucl. Phys.*, B630:87–131, 2002. https://arxiv.org/abs/hep-ph/0112305.

[10] C. Bobeth, T. Ewerth, F. Kruger, J. Urban. Analysis of neutral Higgs-boson contributions to the decays $B_{s,d} \to \ell^+\ell^-$ and $B_{s,d} \to K\ell^+\ell^-$. *Phys. Rev.*, D64(2001) 074014. https://arxiv.org/abs/hep-ph/0104284.

[11] D. Becirevic, N. Kosnik, F. Mescia, E. Schneider. Complementarity of $B_s \to \mu^+\mu-$ and $B \to K\ell^+\ell^-$ in New Physics searches. 2012. https://arxiv.org/abs/1209.0969.

[12] E. Nardi D. Guetta. Searching for new physics in rare $\overrightarrow{B}\tau$ decays. *Phys. Rev.*, D58:012001, May 1998. https://link.aps.org/doi/10.1103/PhysRevD.58.012001.

[13] A. Djouadi. The anatomy of electroweak symmetry breaking Tome II: The Higgs bosons in the Minimal Supersymmetric Model. *Physics Reports*, 459(1-6):1–241, Apr 2008. http://dx.doi.org/10.1016/j.physrep.2007.10.005.

[14] E.H. Logan, U. Nierste. $B_{s,d} \to \ell^+\ell^-$ in a Two-Higgs-Doublet Model. *Nucl. Phys.*, B586:39-55,2000. https://arxiv.org/abs/hep-ph/0004139.

[15] F. Mahmoudi. SuperIso v3.4: A program for calculating flavour physics observables in 2HDM and supersymmetry. 2014. http://superiso.in2p3.fr/superiso3.4.pdf.

[16] R. Scalise F. Olness. Regularization, renormalization, and dimensional analysis: Dimensional regularization meets freshman EM. *American Journal of Physics*, 79(3):306–312, Mar 2011. http://dx.doi.org/10.1119/1.3535586.

[17] G. Buchalla, A.J. Buras, M.E. Lautenbacher. Weak decays beyond leading logarithms. *Rev. Mod. Phys.*, 68:1125–1144, 1996. https://arxiv.org/abs/hep-ph/9512380.

[18] G. Bélanger, F. Boudjema, A. Pukhov, A. Semenov. microOMEGAs: A program for calculating the relic density in the MSSM. *Computer Physics Communications*, 149(2):103–120, Dec 2002. http://dx.doi.org/10.1016/S0010-4655(02)00596-9.

[19] G. Bélanger, F. Boudjema, A. Pukhov, A. Semenov. microMEGAs: Version 1.3. *Computer Physics Communications*, 174(7):577–604, Apr 2006. http://dx.doi.org/10.1016/j.cpc.2005.12.005.

[20] H. Georgi. Effective field theory. *Ann. Rev. Nucl. Part. Sci.*, 43:209–252, 1993. https://doi.org/10.1146/annurev.ns.43.120193.001233.

[21] T. Thomas H. Greaves. On the CPT theorem. *Studies in History and Philosophy of Science Part B: Studies in History and Philosophy of Modern Physics*, 45:46–65, Feb 2014. http://dx.doi.org/10.1016/j.shpsb.2013.10.001.

[22] U. Nierste I. Dunietz, R. Fleischer. In pursuit of New Physics with B_s decays. *Physical Review*, 63(D11), May 2001. http://dx.doi.org/10.1103/PhysRevD.63.114015.

[23] K. De Bruyn, R. Fleischer, R. Knegjens, P. Koppenburg, M. Merk, N. Tuning. Branching Ratio Measurements of B_s Decays. *Phys. Rev.*, D86:014027, 2012. https://arxiv.org/abs/1204.1735.

[24] M. Cahill-Rowley, J. Hewett, A. Ismail, T. Rizzo. Constraints on Higgs Properties and SUSY Partners in the pMSSM, 2013. https://arxiv.org/abs/1308.0297.

[25] M. Drees, R. Godbole, P. Roy. *Theory and phenomenology of Sparticles: an account of four-dimensional N=1 supersymmetry in high-energy physics*. World Scientific, Singapore, 2004. https://cds.cern.ch/record/873465.

[26] M. Tanabashi et al. (Particle Data Group). *Phyis. Rev.*, D98, 030001 (2018) and 2019 update.

[27] M. van Beekveld, W. Beenakker, S. Caron, R. Castelijn, M. Lanfermann, A. Struebig. Higgs, di-Higgs and tri-Higgs production via SUSY processes at the LHC with 14 TeV. *JHEP*, 05:044, 2015. https://arxiv.org/abs/1501.02145.

[28] M.E. Peskin, D.V. Schroeder. *An Introduction to quantum field theory*. Addison-Wesley, Reading, USA, 1995. http://www.slac.stanford.edu/~mpeskin/QFT.html.

[29] P. Colangelo, A. Khodjamirian. QCD sum rules, a modern perspective. pages 1495–1576, 2000. https://arxiv.org/abs/hep-ph/0010175.

[30] P.Z. Skands and others. SUSY Les Houches accord: Interfacing SUSY spectrum calculators, decay packages, and event generators. *JHEP*, 07:036, 2004. https://arxiv.org/abs/hep-ph/0311123.

[31] M. Adinolfi Z. Ajaltouni S. Akar J. Albrecht F. Alessio M. Alexander S. Ali G. Alkhazov et al. R. Aaij, B. Adeva. Measurement of the $B_s^0 \to \mu^+\mu^-$ Branching Fraction and Effective Lifetime and Search for $B_s^0 \to \mu^+\mu^-$ Decays. *Physical Review Letters*, 118(19), May 2017. http://dx.doi.org/10.1103/PhysRevLett.118.191801.

[32] R. Fleischer. Flavour Physics and CP Violation: Expecting the LHC. In *High-energy physics. Proceedings, 4th Latin American CERN-CLAF School, Vina del Mar, Chile, February 18-March 3, 2007*, pages 105–157, 2008. https://arxiv.org/abs/0802.2882/.

[33] R. Fleischer, D. Galárraga Espinosa, R. Jaarsma, G. Tetlalmatzi-Xolocotzi. CP Violation in Leptonic Rare B_s^0 Decays as a Probe of New Physics. *Nikhef*, 2017-038. https://arxiv.org/abs/1709.04735.

[34] R. Fleischer, R. Jaarsma, G. Tetlalmatzi-Xolocotzi. In Pursuit of New Physics with $B_{s,d}^0 \to \ell^+\ell^-$. *JHEP*, 05:156, 2017. https://arxiv.org/abs/1703.10160.

[35] R. Kleiss. *Pictures, Paths, Particles, Processes*, pages 153–155, 164–178. version of August 31, 2018.

[36] G. Rajasekaran. Fermi and the theory of weak interactions. *Resonance*, 19(1):18–44, Jan 2014. http://dx.doi.org/10.1007/s12045-014-0005-2.

[37] S.P. Martin. A Supersymmetry primer. pages 1–98, 1997. https://arxiv.org/abs/hep-ph/9709356.

[38] T. Kajita, E. Kearns, M. Shiozawa. Establishing atmospheric neutrino oscillations with Super-Kamiokande. *Nuclear Physics B*, 908:14 – 29, 2016. http://www.sciencedirect.com/science/article/pii/S0550321316300554.

[39] U. Haisch, F. Mahmoudi. MSSM: cornered and correlated. *Journal of High Energy Physics*, 2013(1), Jan 2013. http://dx.doi.org/10.1007/JHEP01(2013)061.

[40] V. Khachatryan and others. Phenomenological MSSM interpretation of CMS searches in pp collisions at $\sqrt{s} = 7$ and 8 TeV. *JHEP*, 10:129, 2016. https://arxiv.org/abs/1606.03577.

[41] M. van Beekveld. Possible Indirect Detection of Dark Matter and its impact on LHC Supersymmetry searches. Master's thesis, Radboud University Nijmegen, 2016.

[42] T. van Daal. Renormalization group invariants in the minimal supersymmetric standard model. Master's thesis, Radboud University Nijmegen, 2014.

[43] W. Porod. SPheno, a program for calculating supersymmetric spectra, SUSY particle decays and SUSY particle production at e^+e^- colliders. *Comput. Phys. Commun.*, 153:275–315, 2003. http://de.arxiv.org/abs/hep-ph/0301101.

A   CKM and PMNS matrix

The CKM matrix is a 3×3 unitary quark mixing matrix. The elements are related to the different quark transitions that can take place. The matrix is assigned to the down-type quarks and connects the gauge eigenstates (d', s', b') to the mass eigenstates (d, s, b) in the following way

$$
\begin{pmatrix} d' \\ s' \\ b' \end{pmatrix} = \begin{pmatrix} V_{ud} & V_{us} & V_{ub} \\ V_{cd} & V_{cs} & V_{cb} \\ V_{td} & V_{ts} & V_{tb} \end{pmatrix} \begin{pmatrix} d \\ s \\ b \end{pmatrix}
\tag{88}
$$

The CKM matrix can be parametrized by three mixing angles and one phase. In the 'standard parametrization' used by the Particle Data Group (PDG)[26] it takes the following form

$$
V_{\mathrm{CKM}} = \begin{pmatrix} c_{12}c_{13} & s_{12}c_{13} & s_{13}e^{-i\delta} \\ -s_{12}c_{23} - c_{12}s_{23}s_{13}e^{i\delta} & c_{12}c_{23} - s_{12}s_{23}s_{13}e^{i\delta} & s_{23}c_{13} \\ s_{12}s_{23} - c_{12}c_{23}s_{13}e^{i\delta} & -c_{12}s_{23} - s_{12}c_{23}s_{13}e^{i\delta} & c_{23}c_{13} \end{pmatrix},
\tag{89}
$$

where θ_{ij} for $i, j = 1, 2, 3$ (referring to the three generations) are the mixing angles, $s_{ij} = \sin\theta_{ij}$, $c_{ij} = \cos\theta_{ij}$ and δ is the overall phase. This phase is responsible for all CP violating phenomena that occur in flavor changing processes in the SM. The magnitudes $|V_{ij}|$ of the CKM elements are determined by experiment. The following values are provided by the PDG[26]

$$
\begin{pmatrix} |V_{ud}| & |V_{us}| & |V_{ub}| \\ |V_{cd}| & |V_{cs}| & |V_{cb}| \\ |V_{td}| & |V_{ts}| & |V_{tb}| \end{pmatrix} = \begin{pmatrix} 0.97420 \pm 0.00021 & 0.2243 \pm 0.0005 & 0.00394 \pm 0.00036 \\ 0.218 \pm 0.004 & 0.997 \pm 0.017 & 0.0422 \pm 0.0008 \\ 0.0081 \pm 0.0005 & 0.0394 \pm 0.0023 & 1.019 \pm 0.025 \end{pmatrix}.
\tag{90}
$$

As can be seen, there is a hierarchy in the flavor changing quark processes. Elements on the diagonal, corresponding to transitions that take place within the same generation, are of $\mathcal{O}(1)$. The off-diagonal elements are smaller. This means that processes that involve quark transitions between different generations are suppressed with respect to processes that have transitions within the same generation.

Similar to the the quark sector, also in the lepton sector the gauge eigenstates do not need to coincide with the mass eigenstates. This gives rise to lepton mixing in the charged current interactions. The lepton mixing is described by the Pontecorvo–Maki–Nakagawa–Sakata (PMNS) matrix, which is assigned to the neutrinos. It connects the gauge eigenstates $(\nu_e, \nu_\mu, \nu_\tau)$ to the mass eigenstates (ν_1, ν_2, ν_3) in the following way

$$
\begin{pmatrix} \nu_e \\ \nu_\mu \\ \nu_\tau \end{pmatrix} = \begin{pmatrix} U_{e1} & U_{e2} & U_{e3} \\ U_{\mu 1} & U_{\mu 2} & U_{\mu 3} \\ U_{\tau 1} & U_{\tau 2} & U_{\tau 3} \end{pmatrix} \begin{pmatrix} \nu_1 \\ \nu_2 \\ \nu_3 \end{pmatrix}.
\tag{91}
$$

Similar to the CKM matrix, the PMNS matrix (U_{PMNS}) involves three mixing angles and one CP violating phase. It can be written in the 'standard parametrization' as in equation 89. According to equation 91, if the PMNS matrix is not a unit matrix, this implies that the neutrinos produced in weak interaction processes ($\nu_{e,\mu,\tau}$) are linear superpositions of the mass eigenstates ($\nu_{1,2,3}$). These mass eigenstates evolve differently with time and therefore the $\nu_{e,\mu,\tau}$ neutrinos can oscillate into each other while traveling a certain distance. Neutrino oscillations were first observed in 1998 at the Super-Kamiokande experiment[38]. The oscillations only take place because the mass eigenstates are not equal to the gauge eigenstates. From this we can infer that neutrinos have non-zero masses.

B   SLHA Input file

```
BLOCK MODSEL # Model selection
1 0 # nonUniversal
5 2 #CPV
#
BLOCK SMINPUTS # Standard Model inputs
1 1.27118000e+02 # alpha_em^-1(M_Z)^MSbar
2 1.16637000e-05 # G_F [GeV^-2]
3 1.18700000e-01 # alpha_S(M_Z)^MSbar
4 9.11876000E+01 # M_Z pole mass
5 4.18000000E+00 # mb(mb)^MSbar
6 1.73100000E+02 # mt pole mass
7 1.77686000e+00 # mtau pole mass
     8 0.00000000E+00  # m_nu_3
#
BLOCK MINPAR # Input parameters - minimal models
#
BLOCK EXTPAR # Input parameters - non-minimal models
# 0   5.292641E+02  # SUSY SCALE
     1     4.41926538E+03  # M_1
     2     2.70650076E+03  # M_2
     3     4.41459338E+03  # M_3
    11     3.88246223E+03  # A_t
    12    -3.64397462E+02  # A_b
    13    -5.45062502E+03  # A_tau
    23    -1.26771531E+03  # mu
    25     2.54977966E+01  # tan(beta)
    26     5.39388571E+03  # m_A, pole mass
    31     2.42003542E+03  # M_L1
    32     2.42003542E+03  # M_L1
    33     1.40201827E+03  # M_L3
    34     3.31942516E+03  # M_eR
    35     3.31942516E+03  # M_eR
    36     1.63490543E+03  # M_tauR
    41     5.21569221E+03  # M_Q1
    42     5.21569221E+03  # M_Q1
    43     3.79651766E+03  # M_Q3
    44     2.21101113E+03  # M_uR
    45     2.21101113E+03  # M_uR
    46     3.52896237E+03  # M_tR
    47     5.33239559E+03  # M_dR
    48     5.33239559E+03  # M_dR
    49     1.87570538E+03  # M_bR
#
#BLOCK IMEXTPAR # Input parameters - non-minimal models
# 0 5.29264150E+02  # Set
# 1 0.0 # M_1(MX)
# 2 00e+03 # M_2(MX)
# 3 0e+03 # M_3(MX)
# 11 0e+03 # At(MX)
# 12 0e+03 # Ab(MX)
# 13 0e+03 # Atau(MX)
# 23 0e+02 # mu(MX)
# #
Block SPhenoInput # SPheno specific input
1 -1 # error level
2 0 # SPA conventions
11 1 # calculate branching ratios
12 1.00000000E-04 # write only branching ratios larger than this value
21 0 # calculate cross section
```

C Background information

Pre-factor calculation

Parameter	Value
G_F	$1.16639 \cdot 10^{-5}$ GeV$^-$2
α^{-1}	137
M_{B_s}	5.369 GeV
$\tau_{B_s}/\hbar$	$1.51 \cdot 10^{-12}/6.59 \cdot 10^{-25} = 2.91 \cdot 10^{12}$ GeV^{-1}
f_{B_s}	0.2277 GeV
V_{tb}	0.999
V_{ts}	0.0403
$m_{\mu_{\mathrm{pole}}}$	0.105 GeV
$\sin\theta_W$	0.2223

Table 12: Values used for the calculation of the pre-factor.

SM input values

Parameter	Value
$\alpha^{-1}(M_Z)$	127.118
G_F	$1.16637 \cdot 10^{-5}$ GeV$^-$2
$\alpha_s(M_Z)$	0.1187
$M_{Z_{\mathrm{pole}}}$	91.876 GeV
$m_b(m_b)$	4.18 GeV
$m_{t_{\mathrm{pole}}}$	173.1 GeV
$m_{\tau_{\mathrm{pole}}}$	1.77686 GeV

Table 13: List of the SM parameters used as an input for SPheno. The parameters $\alpha^{-1}(M_Z)$, $\alpha_s(M_Z)$ and $m_b(m_b)$ are evaluated in the $\overline{\mathrm{MS}}$ scheme.

Scanning ranges

Parameter	Range
M_1	[1 GeV, 10 TeV]
M_2	[-10 TeV, 10 TeV]
M_3	[1 GeV, 10 TeV]
μ	[-8 TeV, 8 TeV]
$\tan\beta$	[1, 80]
m_A	[1 GeV, 16 TeV]
A_t	[-16 TeV, 16 TeV]
A_b	[-16 TeV, 16 TeV]
A_τ	[-16 TeV, 16 TeV]
$m_{\tilde{Q}1}$	[1 GeV, 10 TeV]
$m_{\tilde{u}R}$	[1 GeV, 10 TeV]
$m_{\tilde{d}R}$	[1 GeV, 10 TeV]
$m_{\tilde{Q}3}$	[1 GeV, 10 TeV]
$m_{\tilde{t}R}$	[1 GeV, 10 TeV]
$m_{\tilde{b}R}$	[1 GeV, 10 TeV]
$m_{\tilde{L}1}$	[1 GeV, 16 TeV]
$m_{\tilde{e}R}$	[1 GeV, 16 TeV]
$m_{\tilde{L}3}$	[1 GeV, 16 TeV]
$m_{\tilde{\tau}R}$	[1 GeV, 16 TeV]

Table 14: Scanning ranges for the pMSSM input parameters.

Mass spectra single parameter variation

Parameter	Value (GeV)	Parameter	Value (GeV)	Parameter	Value (GeV)
$m_{t_{\text{pole}}}$	173.1	$m_{t_{\text{pole}}}$	173.1	$m_{t_{\text{pole}}}$	173.1
$M_{Z_{\text{pole}}}$	91.19	$M_{Z_{\text{pole}}}$	91.19	$M_{Z_{\text{pole}}}$	91.19
M_W	80.32	M_W	80.32	M_W	80.32
$m_{\tau_{\text{pole}}}$	1.777	$m_{\tau_{\text{pole}}}$	1.777	$m_{\tau_{\text{pole}}}$	1.777
m_{h^0}	122.2	m_{h^0}	125.0	m_{h^0}	122.8
m_{H^0}	3090	m_{H^0}	989.9	m_{H^0}	5394
m_{A^0}	3082	m_{A^0}	989.9	m_{A^0}	5394
m_{H^+}	3183	m_{H^+}	993.1	m_{H^+}	5395
$m_{\tilde{d}_L}$	1738	$m_{\tilde{d}_L}$	2883	$m_{\tilde{d}_L}$	5339
$m_{\tilde{d}_R}$	588.2	$m_{\tilde{d}_R}$	2177	$m_{\tilde{d}_R}$	5436
$m_{\tilde{u}_L}$	1736	$m_{\tilde{u}_L}$	2882	$m_{\tilde{u}_L}$	5339
$m_{\tilde{u}_R}$	563.6	$m_{\tilde{u}_R}$	4693	$m_{\tilde{u}_R}$	2391
$m_{\tilde{s}_L}$	1738	$m_{\tilde{s}_L}$	2883	$m_{\tilde{s}_L}$	5339
$m_{\tilde{s}_R}$	588.2	$m_{\tilde{s}_R}$	2177	$m_{\tilde{s}_R}$	5436
$m_{\tilde{c}_L}$	1736	$m_{\tilde{c}_L}$	2882	$m_{\tilde{c}_L}$	5339
$m_{\tilde{c}_R}$	563.6	$m_{\tilde{c}_R}$	4693	$m_{\tilde{c}_R}$	2391
$m_{\tilde{b}_1}$	1127	$m_{\tilde{b}_1}$	5216	$m_{\tilde{b}_1}$	2050
$m_{\tilde{b}_2}$	1271	$m_{\tilde{b}_2}$	6239	$m_{\tilde{b}_2}$	3915
$m_{\tilde{t}_1}$	780.1	$m_{\tilde{t}_1}$	5213	$m_{\tilde{t}_1}$	3595
$m_{\tilde{t}_2}$	1319	$m_{\tilde{t}_2}$	6704	$m_{\tilde{t}_2}$	3931
$m_{\tilde{e}_L}$	1757	$m_{\tilde{e}_L}$	3570	$m_{\tilde{e}_L}$	2453
$m_{\tilde{e}_R}$	1656	$m_{\tilde{e}_R}$	2543	$m_{\tilde{e}_R}$	3335
$m_{\tilde{\nu}_{eL}}$	1755	$m_{\tilde{\nu}_{eL}}$	3568	$m_{\tilde{\nu}_{eL}}$	2452
$m_{\tilde{\mu}_L}$	1757	$m_{\tilde{\mu}_L}$	3570	$m_{\tilde{\mu}_L}$	2453
$m_{\tilde{\mu}_R}$	1656	$m_{\tilde{\mu}_R}$	2543	$m_{\tilde{\mu}_R}$	3335
$m_{\tilde{\nu}_{\mu L}}$	1755	$m_{\tilde{\nu}_{\mu L}}$	3568	$m_{\tilde{\nu}_{\mu L}}$	2452
$m_{\tilde{\tau}_1}$	924.7	$m_{\tilde{\tau}_1}$	2042	$m_{\tilde{\tau}_1}$	1448
$m_{\tilde{\tau}_2}$	1359	$m_{\tilde{\tau}_2}$	2747	$m_{\tilde{\tau}_2}$	3767
$m_{\tilde{\nu}_{\tau L}}$	1356	$m_{\tilde{\nu}_{\tau L}}$	2742	$m_{\tilde{\nu}_{\tau L}}$	1446
$m_{\tilde{g}}$	1858	$m_{\tilde{g}}$	5561	$m_{\tilde{g}}$	4627
$m_{\tilde{\chi}_1^0}$	53.71	$m_{\tilde{\chi}_1^0}$	-1049	$m_{\tilde{\chi}_1^0}$	1288
$m_{\tilde{\chi}_2^0}$	-57.39	$m_{\tilde{\chi}_2^0}$	2744	$m_{\tilde{\chi}_2^0}$	-1291
$m_{\tilde{\chi}_3^0}$	1355	$m_{\tilde{\chi}_3^0}$	-2745	$m_{\tilde{\chi}_3^0}$	2767
$m_{\tilde{\chi}_4^0}$	1753	$m_{\tilde{\chi}_4^0}$	6831	$m_{\tilde{\chi}_4^0}$	4355
$m_{\tilde{\chi}_1^+}$	55.91	$m_{\tilde{\chi}_1^+}$	1049	$m_{\tilde{\chi}_1^+}$	1289
$m_{\tilde{\chi}_2^+}$	1753	$m_{\tilde{\chi}_2^+}$	2746	$m_{\tilde{\chi}_2^+}$	2767

(a) Set 1. (b) Set 2. (c) Set 3.

Table 15: Mass spectra calculated by SPheno for input set 1,2 and 3.